# OPTIMAL DISPERSION OF GRAPHENE IN CEMENT-BASED COMPOSITES FOR IMPROVED MECHANICAL AND DURABILITY PERFORMANCE

A Dissertation

by

ZHANGFAN JIANG

Submitted to School of Engineering and Applied Science of

University of Virginia

In partial fulfillment of the requirements of the degree of

DOCTOR OF PHILOSOPHY

in

Civil Engineering

May 2022

# OPTIMAL DISPERSION OF GRAPHENE IN CEMENT-BASED COMPOSITES FOR IMPROVED MECHANICAL AND DURABILITY PERFORMANCE

A Dissertation

by

ZHANGFAN JIANG

Submitted to School of Engineering and Applied Science of
University of Virginia
In partial fulfillment of the requirements of the degree of

DOCTOR OF PHILOSOPHY

in

Civil Engineering

Approved by:

| | |
|---|---|
| Chair of Committee, | Devin K. Harris |
| Committee Members, | Osman E. Ozbulut (Advisor)<br>Jose Gomez<br>Ji Ma<br>Lisa Colosi Peterson |

May 2022

# DEDICATION

*To my lovely family*

*“家人闲坐， 灯火可亲”*

# ABSTRACT

## Optimal Dispersion of Graphene in Cement-Based Composites for Improved Mechanical and Durability Performance

Zhangfan Jiang
B.Sc. Harbin Institute of Technology
M.S. University of Virginia

Advisor: Dr. Osman E. Ozbulut
Associate Professor, Department of Engineering Systems and Environment
University of Virginia

Cementitious materials are the most widely used materials in our built environment even though the production of cement requires considerable energy and causes significant global carbon dioxide emissions, leading to various environmental and social impacts. As the performance of cement-based composites is strongly affected by their nano-scale properties, one potentially transformative approach to introduce superior performance in these composites is nanoengineering. Graphene, which offers outstanding mechanical properties at a low-cost, can serve as an exceptional nano-reinforcement in cement composites. However, certain challenges currently hinder the use of graphene in cement composites. In particular, graphene sheets often aggregate into flakes of weakly interacting monolayered sheets due to their strong hydrophobicity and van der Waals attraction. To leverage the excellent mechanical properties of graphene in cement-based composites, its dispersion problem needs to be addressed. In addition, though there have been various studies where the graphene-based nanomaterials have been used in either cement paste or mortar composites to improve their mechanical properties, only a few studies have explored the effects of graphene in cementitious composites with coarse aggregates that possess different physico-mechanical behavior.

This study investigates an effective dispersion method and an optimal morphology and concentration of graphene-based nanomaterials for the incorporation into cement composites. First, the use of commercially available graphene nanoplatelets (GNPs) in concrete mixtures is investigated. For the dispersion of GNPs, high shear mixing at different durations with and without additional ultrasonication is used. A polycarboxylate-based superplasticizer (PCE) is utilized to assist the dispersion. The compression and flexural strength are evaluated on concrete mixtures, while direct tensile tests are conducted on mortar specimens to evaluate tensile properties of GNP-reinforced cement composites. As the performance enhancement obtained from PCE-assisted dispersion of GNP into cement composites have remained modest, the use of several other surfactants, including two ionic surfactants, one non-ionic surfactant, and ultrasonication are explored for the fabrication of graphene-reinforced cement composites. Taguchi method of experimental design is employed to minimize the number of experiments needed to assess the effects of selected factors on the dispersion process. Two multi-criteria decision making methods, namely Technique for Order Preference by Similarity to an Ideal Solution (TOPSIS) and Principle Component Analysis (PCA) methods, are employed to determine the optimal values of experimental factors. The findings of the optimal dispersion study are used to fabricate GNP-reinforced mortar composites. The mechanical and durability properties of the graphene-reinforced cement composites is thoroughly investigated. Finally, a life-cycle assessment framework is used to evaluate environmental performance of the developed cement composites over stages from “cradle-to-gate”. Results show that the incorporation of GNPs at 0.1 wt.% of cement can increase the compression strength by 36%, tensile strength by 48%, and significantly reduce permeability and sorptivity of mortar composites.

# ACKNOWLEDGEMENTS

I am fortunate to have had so many great people during my study at University of Virginia, without whom this dissertation would not been possible.

I would like to express my deep gratitude to my advisor, Prof. Osman E. Ozbulut, who is an inspiring scholar and great mentor. He is always there whenever needed. Without his guidance, support and encouragement, this dissertation will never have a successful completion. He is always patient to guide me on the research. Whenever I feel confused about myself and my work, he is never stingy with his compliments. He generously guides me to conduct researches, think scientifically, write professionally. He has always tried his best to help us. I feel very lucky and honored to be among his students and work under his supervision during my graduate study.

I would also like to sincerely thank Prof. Devin Harris, Prof. Ji Ma, Prof. Jose Gomez and Prof. Lisa Colosi Peterson for being my dissertation committee members. Thanks for their continues support and feedback to make this dissertation better.

I would like to acknowledge the teams at University of Virginia and Virginia Transportation Research Council for their guidance and assistance in this research. I would send my sincere thanks to Mr. William Bill Ordel, Mr. Kenneth Herrick, Mr. Michael Burton, Mr. Keegan Gumbs, Mr. Derek Henderson, Mr. Richard White, Mr. Joseph Thompson, Prof. Gary Koenig, Chen Cai, Prof. Geoffrey M. Geise, and Patrick McCormack.

I have been blessed to be surround by smart and enthusiastic friends. Special thanks go to Abdou Karim and Ugur Kilic, who always offer help on everything without hesitate and encouragement during tough time. Thanks to Muhammad Sherif for his support on my research and life. If were to mention the good memories with all my best friends, this acknowledgement will be too long. I want to send my thanks to Xueying Zhao, Fangwei Cheng, Bingrong Sun, Qiang Chen, Zheng Chen, Wenjian Jia, Lian Cui, who are always be there with me, for there generous support and encouragement.

I want to extend my deepest gratitude to my family, my parents, Guoping Jiang and Huijun Zhang, my grandparents, Deqing Zhang and Aizhen Chen. With their unconditional love and infinite support, I have the courage to study overseas and have the faith to do what I want to do. I thank my husband, Li Ding, my better half, for always being there with me, for making me laughing and laughing with me, for supporting and encouraging me without hesitate, for always being proud of me.

At the end, I also want to thank myself for never giving up. Someone said, PhD study is tough. But when I look back on these days, I am very lucky to have all my professors, my friends and my families to stand by me. They turned all the tough time to good memories. I think that’s why I have the faith to complete my PhD.

# NOMENCLATURE

| | |
|---|---|
| A | Amplitude |
| AE | Acoustic Emissions |
| AF | Average Frequency |
| ANOVA | Analysis of Variance |
| BG | Bilayer Graphene |
| BIC | Bayesian Information Criterion |
| CF | Carbon Fiber |
| CH | Calcium Hydroxide |
| CNF | Carbon Nanofiber |
| CNTs | Carbon Nanotubes |
| CPS | Cement Pore Solution |
| C-S-H | Calcium Silicate Hydrate |
| D | Duration |
| DF | Degree of Freedom |
| DLVO | Derjaguin-Landau-Verwey-Overbeek |
| DTG | Derivative of Thermogravimetric |
| F127 | Pluronic F127 |
| FLG | Few Layer Graphene |
| FWHM | Full Width at Half Maximum |
| G | Graphene |
| GEV | Generalized Extreme Value |
| GNPs | Graphene Nanoplatelets |
| GO | Graphene Oxide |
| GWP | Global Warming Potential |
| ITZ | Interfacial Transition Zone |
| LCA | Life Cycle Assessment |

| | |
|---|---|
| LCCA | Life Cycle Cost Analysis |
| LCI | life Cycle Inventory |
| LCIA | Life Cycle Impact Assessment |
| MS | adjusted Mean of Squares |
| MS | Melamine-based Superplasticizer |
| MWCNT | Multi Wall Carbon Nanotube |
| NS | Naphthalene-based Superplasticizer |
| PAA | Polyacrylic Acid |
| PCA | Principle Component Analysis |
| PCE | Polycarboxylate-based Superplasticizer |
| PDF | Probability Density Function |
| PEO | Polyethylene Oxide |
| PVA | Polyvinyl Alcohol |
| RA | Rise Time over Amplitude |
| rGO | reduced Graphene Oxide |
| RT | Rise Time |
| S/N | Signal-to-Noise |
| SC | Sodium Cholate |
| SDBS | Sodium Doecylbenzene Sulfonate |
| SEM | Scanning Electron Microscopy |
| SP | Superplasticizer |
| SS | adjusted Sum of Squares |
| SWCNT | Single Wall Carbon Nanotube |
| TBP | Tributyl Phosphate |
| TG | Thermogravimetric |
| TGA | Thermogravimetric Analysis |
| TOPSIS | Technique for Order Preference by Similarity to an Ideal Solution |
| UV-vis | Ultraviolet-visible |

|  |  |
|---|---|
| UE | Ultrasonication Energy |
| DLS | Dynamic Light Scattering |
| UHPC | Ultra-high Performance Concrete |

# TABLE OF CONTENTS

# LIST OF TABLES

# LIST OF FIGURES

# 1. INTRODUCTION

## 1. 1. Problem Statement

Cementitious composites are the most widely used materials for the design of civil structures. They are produced from raw materials that are low-cost and readily available. They exhibit high compressive strengths, good fire resistance, and can be considered as more durable compared to other construction materials. However, cementitious materials also face a number of challenges [1]. Present and future durability challenges for reinforced concrete structures. The production of cement requires considerable energy and causes significant global carbon dioxide emissions, leading to various environmental and social impacts [2]. In addition, conventional cementitious composites are inherently brittle and susceptible to cracking, which render them vulnerable especially under harsh operating conditions. Cementitious materials with improved mechanical performance and durability can provide substantial improvement in damage resistance and service life of future concrete infrastructure. This will lower the energy and emissions for concrete materials and structures, leading to more sustainable built environment.

## 1. 2. Research Motivation

As performance of cementitious composites is strongly affected by their nano-scale properties, one potentially transformative approach to introduce superior performance in cement composite materials is nanoengineering. Since early 1990s, numerous research studies have been conducted to explore behavior of cementitious composites with different functional fillers such as carbon fiber (CF), carbon nanofiber (CNF), carbon nanotubes (CNTs), colloidal nano silica, iron oxide nanoparticles, and nickel powder [3–10]. Among these different fillers, CNTs have been the most widely used filler in cement matrix to develop advanced cementitious composites [11]. CNTs are molecular-scale tubes of graphene, which is a single-layer $sp^2$-bonded carbon sheet. CNTs have a tensile strength of 11 to 63 GPa and a Young's modulus of 0.3 to 0.9 TPa [12]. CNTs can exist as single-walled (SWCNT) or multi-walled carbon nanotubes (MWCNT). Depending on their quality and type, the cost of SWNTs ranges from $37,500 to $160,000 per kg and the cost of MWCNTs ranges from $600 to $15,000 per kg [13]. Although MWCNTs have considerably higher costs compared to other nanostructured carbons such as carbon black and

CNF, they have been extensively studied as reinforcing nanomaterial in cementitious composites due to their advantageous mechanical and electrical properties [14–19]. Numerous studies have been conducted to develop advanced cementitious composites by incorporating CNTs in cement matrix and considerable improvements in various mechanical properties have been reported [20]. However, most of these nano-reinforced composites could not be utilized at commercial scale, mainly due to their cost and/or the difficulties in their processing. In addition, previous research has mainly focused on the use of carbon nanomaterials in cement paste and mortar composites, while only very limited studies have explored the role of these nanomaterials in concrete composites that possess different physico-mechanical behavior [20].

Graphene, as the strongest material ever measured with a tensile strength of 130 GPa and Young’s modulus of about 1 TPa, is expected to serve as an exceptional nano reinforcement in composite materials [21]. Compared to quasi-one-dimensional (1D) CNTs, graphene sheets are two-dimensional (2D), and both sides of the atomic lattice contact the matrix of a composite system, thereby generating more sites for potential chemical and physical bonding with the host material. Most importantly, graphene sheets and their derivatives can be synthesized in large quantities from inexpensive graphite powder [22] and can be produced at large-scale for industrial demand at low-cost.

Graphene-based nanomaterials can enhance nucleation effect and promote cement hydration reaction, refine the microstructure and improve the compactness of cement composite, and constrain the propagation of microcracks. These enhancements can help to reduce cement content and develop more sustainable concrete materials. However, the agglomeration effect due to the strong van der Waals force between graphene sheets makes the uniform dispersion difficult and limit the efficacy of graphene [21]. Graphene sheets tend to recombine due to attractive van der Waals forces after the energy supplied by mechanical agitation through ultrasonication or high shear mixing. The re-clustering of graphene sheets is to be avoided either by decreasing the van der Waals forces between the nanoparticles or by introducing a carrier medium with induced repulsive forces (steric, or electrostatic forces) between nanoparticles.

Pristine graphene sheets are not dispersible in water due to a large mismatch between the low surface energy of graphene, high surface tension of water, and limited mobility. An effective approach to increase the dispersion of graphene in any medium can be through the surface modification of pristine graphene to reduce the nanoparticle after oxidation and exfoliation; however, this method will introduce *structural defects* into graphene and help pick up residual oxygen-containing groups, which leads to loss of desired physical and mechanical properties. An alternative and relatively simple approach could be the stabilization of graphene through *non-covalent modifications using surfactants*. However, *strong alkaline environment of cement hydration affects the adsorption behavior of surfactants* and the stable suspensions of graphene re-agglomerate after being introduced to cement pore solution due to the adverse effects of high pH environment to surfactant-graphene interface. Therefore, to leverage the excellent mechanical properties of graphene in cement-based composites, there is still a need to address its dispersion problem.

## 1. 3. Research Objectives

This research aims to formulate graphene-reinforced cementitious materials that are intrinsically resilient and durable, and as a result, can extend the service life of concrete structures. The graphene, which possesses a large surface area and a high aspect ratio, offers outstanding mechanical, electrical and thermal properties at relatively low cost. It is therefore considered as ideal nanomaterial for the development of advanced composite materials. However, its use in concrete industry at large scales requires low fabrication costs while preserving its exceptional structural properties. In addition, only when graphene sheets are homogeneously dispersed within the cementitious matrix, significant enhancement on mechanical properties and durability can be obtained. In this research, the use graphene nanoplatelets (GNPs) in cement-based composites is explored. An efficient dispersion of graphene sheets without damaging their unique structural integrity into the cement matrix is aimed to be developed. A multi-scale characterization is carried out to reveal the effects and reinforcing mechanism of graphene to cementitious matrix with and without coarse aggregates. The durability of the developed composites is analyzed through assessing porosity and capillary water absorption. Then, an environmental life cycle analysis is performed to assess the energy and emissions related to production of the developed graphene-reinforced cement composites.

## 1. 4. Organization of This Dissertation

This dissertation is organized into the following sections:

*Chapter 1* describes the motivation for the research and the scope of the research. It also gives a brief description of this dissertation.

*Chapter 2* presents a concise summary of the application of nanomaterials in cement composite and its advantages. It then provides some background information of graphene-based nanomaterials and the dispersion of graphene-based nanomaterials. Furthermore, the literature review of graphene-based cement composites is presented.

*Chapter 3* investigates the effects of GNPs on the mechanical properties of concrete. The wet dispersion technique which employs high shear mixing and polycarboxylate-based superplasticizer is utilized to disperse GNPs. The effects of sonication time and dispersion equipment on the dispersion of GNPs are studied. The dispersion quality is assessed through optical microscopy, Raman spectroscopy and SEM. Mechanical properties are evaluated through compressive and flexural strength tests. The microstructure of GNP-reinforced concrete is investigated through SEM.

*Chapter 4* characterizes the tensile behavior of GNP-reinforced mortar using acoustic emission. The specimens are tested under direct tensile test. AE parameters such as AF and RA are used to analyze the cracking mode. Average RA is analyzed to explore the effect of GNPs reinforcement. A correlation between average acoustic energy and the tensile strength is established.

*Chapter 5* optimizes the parameters of the surfactant-assisted dispersion process of GNPs using TOPSIS-based and PCA-based Taguchi method. The effects of sonication parameters (time and amplitude), sample volume, surfactant type, surfactant/GNPs ratio, GNPs concentration on the dispersion and stability of GNPs are investigated. Average particle size, the absolute value of zeta potential, UV-vis absorbency in aqueous and alkaline environments, the absolute value of zeta potential in alkaline environment, the residual absorbance after 24 h in aqueous and alkaline environments serves as criteria to characterize the dispersion quality of GNPs. ANOVA is performed to assess the relative importance of each parameter.

*Chapter 6* explores the influence of two types of GNPs on mechanical properties and durability of cement composites. The optimal dispersion procedure found in Chapter 5 is applied to disperse GNPs. The mechanical properties are assessed by compressive strength. The sorptivity and permeable porosity tests are performed to evaluate durability. Thermogravimetric analysis (TGA) and scanning electron microscopy (SEM) analysis are performed to study the hydration process and microstructure of GNP-reinforced cement composites.

*Chapter 7* studies the environment impact of GNP-reinforced mortar by means of Life Cycle Impact Assessment (LCIA) and Life Cycle Cost Analysis (LCCA).

*Chapter 8* summarizes the dissertation work and presents its major findings. It also provides some recommendations for future research.

# 2. LITERATURE REVIEW AND BACKGROUND

## 2. 1. Graphene and Graphene-based Nanomaterials

Graphene, a two-dimensional material comprised of a monolayer of carbon atoms, is the basis of all graphitic materials. Graphene can be wrapped up in a ball to form fullerenes, rolled into CNTs or stacked to form graphite [23]. In each layer, the carbon atoms are connected by staggered single and double covalent bonds to form a planar hexagonal, or honeycomb, lattice structure (Figure 2-1). Each carbon atom contains four valence electrons, which includes three electrons in $sp^2$ hybrid orbitals [24]. Graphene possesses unique properties making it a promising candidate for a multitude of applications [25]. Graphene is the thinnest material currently known with a thickness of only .335 nm [25,26]. Other unique physical properties include a large specific surface area, measured to be as high as 2360 $m^2g^{-1}$ [27] and aspect ratios from 6,000 – 600,000 [12,28]. Furthermore, the mechanical properties of graphene are also unique, as graphene is considered to be the strongest material ever measured [25]. Graphene has a tensile strength of 130 GPa and a modulus of elasticity of 1000 GPa [28,29]. The excellent mechanical properties have sparked research into graphene's use as a method of self-reinforcement in cements, with several studies showing increased flexural, tensile and compressive strength with the inclusion of graphene and its derivatives [30–34]. In addition, the structure of graphene gives it unusual thermal properties. Several researchers have measured the thermal conductivity of graphene and found values in the range from 3000 to 5300 $Wm^{-1}K^{-1}$ [35–39]. The electrical properties of graphene, includes an intrinsic electron mobility of 200,000 $cm^2V^{-1}s^{-1}$ [40] and an electronic conductivity of between $10^7$ and $10^8$ $Sm^{-1}$ [41]. These properties have made graphene a popular choice for use in self-sensing cements, as their high electrical conductivity allows for the formation of conductive pathways.

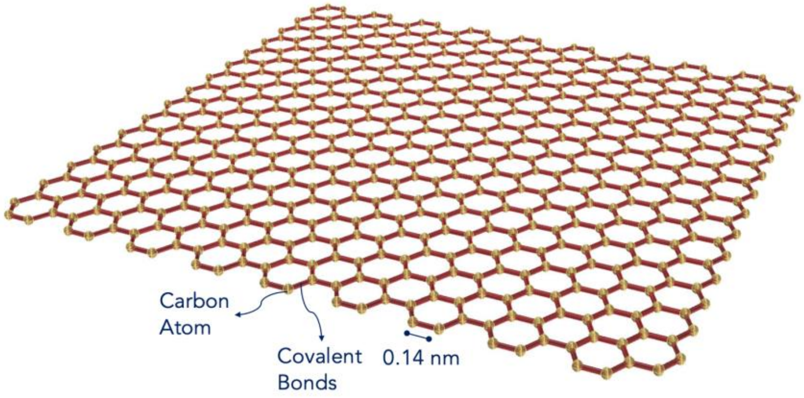

**Figure 2-1.** Structure of graphene.

While the basic unit of graphene is a single monolayer, it can be very difficult to obtain large amounts of single layer graphene. A 2018 study found that out of 60 companies, none of them were producing pure monolayer graphene [42]. As such, other types of graphene containing multiple layers are often studied and considered for future applications. As the properties of graphene are influenced by its thickness, the material is characterized by the number of layers in the flakes. ISO standard ISO/TS 80004-13:2017 defines the different types of graphene, as a function of their layer number [43]. The most relevant categories are graphene, bilayer graphene, few layer graphene and graphene nanoplatelets, which are defined as:

- Graphene (G) refers to a single layer of carbon atoms and represents a building block of all other graphitic materials.
- Bilayer graphene (BG) is simply a graphene flake with two well defined layers.
- Few layer graphene (FLG) is defined as having in-between 3 and 10 well defined stacked graphene layers.
- Graphene nanoplatelets (GNPs) are graphene stacks with thicknesses typically ranging 1 to 3 nm, with a lateral size between 100 nm and 100 µm.

In addition to pure graphene with different number of layers, there are multiple other graphitic materials that contain elements other than carbon and present different characteristics, such as graphene oxide and reduced graphene oxide. Graphene oxide (GO) is a material comprised of graphene layers with attached oxygen-containing functional groups, such as hydroxyl, epoxide, carboxyl and carbonyl groups [44]. GO is typically synthesized by exposing graphite to an oxidant and then exfoliating the oxidized graphite to form few layer oxidized graphene [24]. During the oxidation process a large number of defects can be introduced to the GO layers and, thus, GO is an amorphous material [42]. This loss of crystallinity causes it to be electrically insulating and have reduced mechanical properties [45]. However, while pure graphene is hydrophobic, the oxygen containing functional groups cause GO to be hydrophilic resulting in a high dispersibility in water, as compared to graphene [42,46].

In order to recover some of the lost electrical and mechanical properties of graphene oxide, the material can undergo several processes to form a material with fewer oxide functional groups, known as reduced graphene oxide (rGO). The structure of rGO is similar to that of GO. The material still contains the structural defects that are present in graphene oxide after reduction and, thus, has an amorphous structure [42]. The properties rGO displays are typically in between that of graphene and graphene oxide. It is partially dispersible in water, with the exact ease of dispersion dependent on the amount of remaining oxide functional groups after reduction [46]. The mechanical and electrical conductivities are increased compared to that GO, but lower than that of graphene [42,46].

## 2. 2. Dispersion of Graphene-based Nanomaterials into Cement Composites

One of the largest barriers to the widespread incorporation of graphene in cement-based composites is its poor dispersion in aqueous solutions. This difficulty in obtaining a homogenous suspension is caused by its high surface energy and strong van der Waal forces, combined with its hydrophobic nature [28]. As a result, graphene tends to agglomerate and form aggregates in water, which results in an uneven distribution of properties. This can be especially detrimental to the electrical properties of graphene reinforced cements, as a continuous pathway is needed for electrical conductivity. It has been observed that at higher GNPs concentrations that display aggregates, also show a reduction in piezoresistive effects [47]. GO has an easier time dispersing in water, due to its hydrophilic nature and oxide functional groups. However, the alkaline and ionic nature of cement and its pore solutions can cause GO to form irregular agglomerates, due to crosslinking with $Ca^{2+}$ and reduction of GO to a less-dispersible rGO [48,49]. To address this problem and realize the full potential of graphene-based materials, several methods exist to increase the dispersion in water and cements. Physical methods, such as ultrasonication, high shear mixing, and ball milling, have been employed, as well as chemical methods, such as covalent and noncovalent functionalization.

### *2.2.1. Physical dispersion methods*

The most widely employed method for increasing the dispersion of graphene-based materials is sonication. Sonication is a method during which an acoustic field is used to agitate the suspension. When the frequencies applied are greater than 20 kHz, it is referred to as ultrasonication, which serves to separate the graphene layers by creating cavitation bubbles that quickly collapse and generate shockwaves [50,51]. A majority of studies use sonication in conjunction with other chemical dispersive methods, such as surfactants [52–56].

High shear mixing and ball milling are other types of physical dispersion methods. High shear mixing can be used to combine surfactants with graphene-based materials or it can be used when mixing the suspension with cement to prevent re-agglomeration [46,48]. Similarly, ball milling can be used in various ways to improve dispersion [30]. Furthermore, another study, has utilized ball milling to assist in the production of edge-oxidized graphene oxide [57].

### *2.2.2. Chemical functionalization methods*

Covalent functionalization of a graphene-based material refers to the process of adding a new functional group to the graphene layer by covalently bonding it to the graphene. This functionalization can add a range of properties and characteristics, such as increased ease of dispersion and changes in the conductivity. It is easier to attach new functional groups to GO, as a result of its increased reactivity due the attached oxygen functional groups [24]. This method has several advantages as it creates strong covalent between the functional groups and the graphene sheet. However, covalent functionalization introduces defects to the material, which results in a partial loss of electrical conductivity [58]. This method has been shown to be beneficial for increasing dispersion and improving properties in graphene and graphene oxide reinforced cementitious composites [59,60].

Non-covalent functionalization of a graphene-based material refers to the modification of the material by hydrogen bonds, ionic bonds and electrostatic forces between graphene and functional molecules [24]. This method has distinct advantages over covalent functionalization, as it does not change the bulk structure of the graphene [58]. However, the bonds connecting the functional groups and the graphene are weaker than that of covalently functionalized graphene. One of the most common ways to achieve improved dispersion with noncovalent functionalization is through the use of surfactants. Superplasticizers are commonly used as surfactants in the literature, especially polycarboxylate-based superplasticizer (PCE) [55,61,62]. The molecular structure of PCE consists of an adsorbing anionic backbone and non-ionic side chains and looks like a comb, as shown in Figure 2-2. It has been shown that anionic surfactants can effectively disperse graphene in water [63], while non-ionic surfactants can successfully stabilize and disperse graphene in aqueous solutions [64]. PCE has been shown to be an effective surfactant for GNP, GO and rGO, as it has both anionic and non-ionic components [65]. The backbone will absorb onto the graphene sheet, while the negatively charged side chains will serve to separate the layers [56]. Their ability to disperse graphene has been largely attributed to steric hinderance and electrostatic repulsion that suppresses the van der Waal forces between the graphene layers [54,61]. Other types of superplasticizers, such as naphthalene-based (NS) and melamine-based (MS) superplasticizers have also been studied.

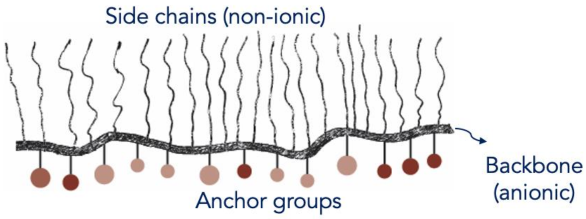

**Figure 2-2.** Schematic representation of typical molecular structure of PCE.

### *2.2.3. Dispersion Using Sonication*

To fabricate a cogent aqueous dispersion of GNPs, the ultrasonication with the aid of surfactants is widely utilized [66]. During the dispersion process, there are many factors needed to be decided. For example, ultrasonication setup, surfactants, solution volume, GNPs dosage, etc.

Zou et. al. [67] explored the effects of  ultrasonication energy (UE) on the dispersion of CNT and engineering properties of CNT cement paste. The CNT was dispersed in water by ultrasonication with different UE varying from 25 to 400 J/mL. The amount of dispersed CNT in water was effectively improved by more intense UE. The optimum UE to obtain a uniform dispersion is found to be dependent on the CNT dosage.

Table 2-1 summarized the dispersion process of GNPs in aqueous. It can be seen that the ultrasonication duration varies from 5 to 60 min. The ultrasonication type and output power are not reported in some papers. Thus, the UE is not able to be calculated. Researcher commonly dispersed the amount of GNPs into the mixing water. Due to the different mix design, the resulted GNPs dosage in water are also different. Thereby, it is difficult to select an optimal dispersion process for GNPs to achieve uniform dispersion.

**Table 2-1.** Dispersion process of GNPs in aqueous

| **Ultrasonication** | | | **Surfactant** | | **GNP (wt%)** | **Solution volume (mL)** | **Ref.** |
|---|---|---|---|---|---|---|---|
| **Type** | **Power (W)** | **Duration (min)** | **Type** | **S/GNP** | | | |
| Probe | 360 | 10 | SDBS | 1.33-4 | 0.03-0.09 | Mixing water | [31] |
| Probe | 300 | 60 | PCE | 7.5-30 | 1 | Mixing water | [56] |
| Bath | 100 | 60 | SP | 1.5-22 | 0.15-0.5 | 13.5 | [68] |
| Probe | 360 | 30 | PCE, NS, MS | 8-16 | 0.03-0.12 | Mixing water | [54] |
| -- | -- | 60 | Silane coupling agent | 10 | 0.1* | 100 | [69] |
| -- | 400 | 30 | -- | -- | 0.08-0.24 | Half of mixing water | [70] |
| Bath | -- | 30 | PCE | 0.05-0.12 | 20* | Mixing water | [71] |
| Tip | 100 | 15 | -- | -- | 2.22* | -- | [72] |
| Probe | -- | 60 | PCE | 0.27-1.6 | 0.5-3.0 | Mixing water | [73] |
| -- | -- | 5 | PCE | 3-6 | 0.25-0.5 | Mixing water | [74] |
| -- | -- | 60 | PCE | 0.13-14 | 0.07-2.59 | Mixing water | [75] |
| -- | 300 | 5 | SDBS | 0.06-0.18 | 0.4-1.2 | Mixing water | [76] |

* g/L

### *2.2.4. Characterization of Graphene Dispersion*

As discussed in the previous sections, one major challenge of utilizing graphene in cement composite is achieving adequate dispersion. Thus, several characterization methods that analyze the morphology of graphene and stability of graphene solutions have been used to examine the dispersion quality.

Raman spectroscopy is a non-destructive tool that can characterize structural quality of graphene-based nanomaterials [77]. The most common features in Raman spectra of graphitic materials are a low intensity D band (~1350 $cm^{-1}$), a strong intensity G band (1582 $cm^{-1}$) and a moderate intensity 2D band (2726 cm$^{-1}$). A typical Raman spectra for graphite is shown in Figure 2-3.

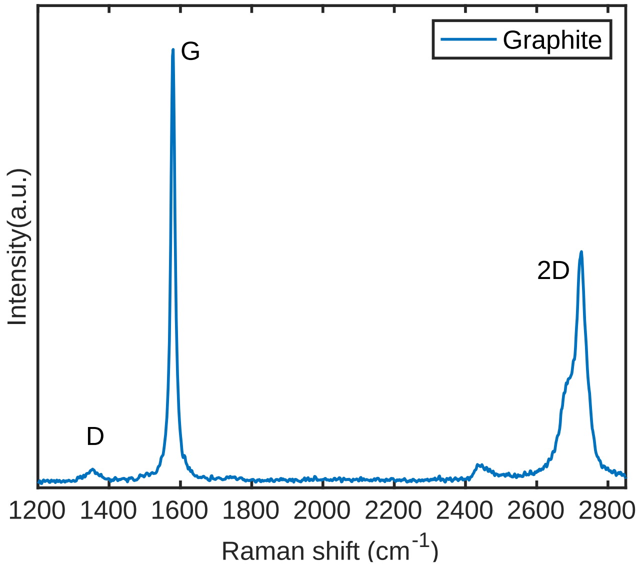

**Figure 2-3.** Raman spectra for graphite.

The G band is attributed to the sp$^2$ carbon network, while the D band is ascribed to defects and disorder [78]. However, the presence of the D band does not directly indicate structural defects (sp$^3$ or vacancy defects). The edge of graphene sheets, i.e., the number of C-atoms with dangling bonds, also acts as defects. Therefore, the intensity ratio of D band and G band ($I_D/I_G$) can provide information about particle size. A larger $I_D/I_G$ indicates a larger fraction of edge defects, i.e., smaller particle size [79].

Usually, the shape and intensity of the 2D band can inform about the number of graphene layers, i.e. thickness. For monolayer graphene, the 2D band exhibits a single Lorentzian feature with a full width at half maximum from 20 ~ 30 cm$^{-1}$, with an intensity ratio of 2D band to G band ($I_{2D}/I_G$) of approximately 2.0 [80–82]. As the number of graphene layers increases, the 2D band shifts to the right with a lower $I_{2D}/I_G$ [83,84]. In some cases, another band, called D' band, can also be observed at ~1620 cm$^{-1}$, relating to the defect-induced process [85]. The intensity ratio of D band to D' band ($I_D/I_{D'}$) can be computed to identify the type of defects. A value of $I_D/I_{D'}$ below 3.5 indicates that the nature of defects is edge or boundary related, whereas a $I_D/I_{D'}$ up to ~7 reflects vacancy basal plane point defects and a $I_D/I_{D'}$ up to ~13 represents sp$^3$ defects [86].

Ultraviolet-visible (UV-vis) spectroscopy can be used to evaluate the dispersion quality and stability of graphene in aqueous media [56,87,88]. The transmittance of solution is measured over a set of wavelengths, which can be converted to the absorbance [89]. The absorbance peak appears at the wavelength of ~260 nm for graphene nanoplatelets and ~230 nm for a monolayer GO [31,88,90,91]. According to the Beer-Lambert law, the absorbance at the peak is proportional to the concentration of graphene [92]. The higher absorbance indicates the better dispersion of graphene in aqueous media [93]. Thus, the reduction in absorbance will directly imply the degree of deterioration of the dispersion, indicating the stability of graphene in aqueous media [94].

Dynamic light scattering (DLS) is a non-invasive and in situ method to measure the size distribution of graphene in liquid solutions. By contrast with other methods, DLS has the significant advantages of larger statistics, quick measurement and no need for drying dispersion solution [95]. DLS probes the Brownian motion of the particles in a liquid solution and measures the translational and rotational diffusion, determining the dimensions of dispersed particles [96–98].

Zeta potential ($\zeta$) from electrophoretic mobility is a strength index that gives an indication of the stability of the colloidal system [99]. The stability of the colloidal system depends on the net summation of attractive van der Waals forces and repulsive pressure from repulsive double layer. The electric double layer consists of two layers, the Stern layer (the inner layer) and the diffuse layer (the outer layer). A repulsive force is generated between dispersed particles when these two layers overlap [87,100–102]. Zeta potential is defined as the potential at the plane of shear that is immediately outside the Stern layer [103–105]. Zeta potential is dependent on both dispersed particles and medium [106]. The greater absolute value of zeta potential ($|\zeta|$) implies the better stability of the dispersion system. The dispersed particles might tend to aggregate and coagulate when $|\zeta|$ is low. When $|\zeta|$ is greater than 30 mV, it is considered to gain sufficient repulsion force between adjacent particles for stable dispersion [107–109].

Optical microscopy with a high magnification can be used to visualize the dispersion of graphene sheets and measure the lateral size distribution of the graphene sheets. The images obtained from optical microcopy can be enhanced with suitable filters and converted to a binary image. Then, an image processing/analysis code can be used to compute the lateral size of each particle shown in the image.

## 2. 3. Graphene-based Cement Composites

There have been various studies where the few layer graphene or GNPs were used in either cement paste or mortar composites to improve their mechanical properties [31,32,93,110,111] or to provide self-sensing characteristics [71,112–116]. On the other hand, only a few studies have explored the effects of GNPs in cementitious composites with coarse aggregates that possess different physio-mechanical behavior [117–120]. Du et al. [117] prepared concrete mixtures with GNP concentrations varying from 0.5% to 2.5% by weight of cement. The GNPs were first added into water and a naphthalene sulfonate-based surfactant and ultrasonicated for two hours. Then, the aqueous suspension was added to dry materials and mixed for three minutes. Various tests were conducted to investigate mechanical and transport properties of the developed composites. They found that GNPs do not have any significant effect on the mechanical properties of the concrete, while the water permeability and chloride diffusion coefficient decrease by 80% with the addition of 1.5% GNPs.

Chen et al. [118] also fabricated GNP-reinforced concrete specimens with GNP ratios from 0.02% to 0.4% and evaluated the freeze-thaw resistance and compressive strength of the developed concrete mixtures. The GNPs were in ethanol aqueous solution and this solution was first added to water. Then, cement and aggregates were added into suspension and mechanically mixed to prepare the concrete mixtures. They found that adding GNPs at a ratio of 0.05% increases the compressive strength of concrete 22% but further increasing the GNP content results in a decrease.

Peyvandi et al. [119] investigated the effects of nano-scale (GNP and CNF) and micro-scale (polyvinyl alcohol or PVA) fibers in high-performance concrete. The mixture consisted of Portland cement, silica fume, coarse and fine aggregates, and a polycarboxylate-based superplasticizer. To improve the dispersion, polyacrylic acid (PAA) was used as surfactant. The GNPs were first mixed with the water and PAA and ultrasonicated for about an hour prior to their addition into dry materials. A modest increase of 12% and 14% in compressive and flexural strength, respectively was reported for a mixture with 0.045 vol.% GNPs and 0.6 vol.% PVA fibers. It was also found that the GNPs considerably improves the moisture sorption resistance.

Liu et al. [120] also developed concrete mixtures with 4.5% GNP content. The GNPs were combined with polycarboxylate-based superplasticizer and the aqueous suspension was ultrasonicated for 30 min prior to mixing with dry materials. This study focused on the damage sensing of the GNP-reinforced cementitious composites. The electrical measurements were carried out while the specimens were tested under compressive loading. The obtained results suggest that damage evolution process of the developed concrete can be monitored through resistivity measurements.

In contrast to above-mentioned studies where no significant effect of GNPs was observed on the mechanical properties of the concrete, Dimov et al. [121] reported an increase of 146% in the compressive strength and 80% in the flexural strength of the concrete for the graphene-reinforced concrete. In that study, both commercially available GNPs and graphene sheets obtained through liquid-phase exfoliation of graphite powder was used. The GNPs were dispersed in the water using two hours of high shear mixing at 5000 rpm and then incorporated into concrete mixture. In addition to very high increases in the mechanical properties, a significant improvement in water permeability was reported for the developed concrete composites with 0.7 g of GNPs in 1 liter of mixing water. This reported concentration of the GNPs corresponds to a GNP ratio of 0.04% by weight of cement.

Besides, no previous studies explored the effects of GNPs on mortar composites through direct tensile testing. There was one earlier study where the influence of multi-layer graphene on the tensile behavior of mortar composites was studied [122]. In that study, splitting tensile tests were conducted to indirectly assess the tensile strength of the mortar composites. The samples with 0.033% multilayer graphene achieved the optimal tensile strength, for which the corresponding increment was 131.6% at 28days, comparing with the plain samples.

GNPs used in earlier studies have different particle size, thickness and surface area. These characteristics of GNPs have shown to significantly affect the reinforcing capability of GNPs in other composites such as polymers [123–125]. However, there have been limited studies to systematically explore the effects of particle size and surface area on the mechanical and permeability properties of GNP reinforced cementitious composites.

Dong et. al. [126] explored the lateral size effect of graphene on the nano/micro-structures and mechanical properties of ultra-high performance concrete (UHPC). Graphene with lateral size of 3 µm, 10 µm, and 50 µm was incorporated. The graphene with lateral size of > 50 µm was found to improve the C-S-H structure due to the nucleation site effect and the formation of core-shell elements during hydration process. With the increasing graphene lateral size, the compressive strength, toughness and three-point bending modulus of UHPC is increased. It can be concluded that the lateral size of graphene visibly influences the nano/micro-structure of UHPC, resulting in obviously different reinforcement on properties of UHPC.

From above discussions, it can be concluded that there is limited information on the effects of few layer graphene or GNPs on the mechanical properties of cementitious composites with coarse aggregates, i.e. concrete. Furthermore, from available studies, there are conflicting conclusions: either a limited /no increase [117–119], or very high increase [121] in mechanical properties was reported.

## 2. 4. Life Cycle Assessment

The cement industry accounts for approximately 5% of anthropogenic carbon dioxide ($CO_2$) emission worldwide [127]. Approximately 900 kg of $CO_2$ are released into the atmosphere to produce 1 ton of cement [128]. Life cycle assessment (LCA) is an important tool to assess environment impact. It enables to estimate the cumulative potential environment impact under the categories of global warming, ozone depletion and so on, during a product life cycle [129].

Generally, the LCA framework contains four phases, according to ISO 14040:

- Goal and scope definition: statement of intent for study.
- Inventory analysis: collect and document data.
- Impact assessment: transit from simple inventory results to impacts.
- Interpretation: put results into perspective and recommend improvement.

The LCA can be performed at three system boundaries: (1) cradle-to-gate, i.e., consider the raw material extraction and material production; (2) cradle-to-grave, which includes the raw material extraction, material production, the exit of the final product from the factory, and the use, demolition, and waste phase; (3) cradle-to-cradle, which is cradle-to-grave phase add recycling and extensive reuse of the waste phase [130].

# 3. EFFECTS OF GNPs ON COMPRESSION AND FLEXURAL STRENGTH OF CONCRETE COMPOSITES

## 3. 1. Overview

In this chapter, an experimental investigation is carried out to study the effects of graphene nanoplatelets (GNPs) on the mechanical properties of cementitious composites with coarse aggregates. The concrete mixtures with GNPs concentrations ranging from 0.025% to 0.10% by weight of the cement are prepared, where a wet dispersion technique that employs high shear mixing and polycarboxylate-based superplasticizer to disperse GNPs in water. The effects of various dispersion parameters including different high shear mixing durations as well as the use of ultrasonication together with high shear mixing on the dispersion of GNPs are studied. The dispersion quality of GNPs is assessed through optical microscopy, Raman spectroscopy, and Scanning Electron Microscopy tests. Compressive strength and flexural strength tests are conducted to assess the effects of GNPs on mechanical properties of the fabricated GNP-reinforced concrete specimens. Results show that all the dispersion procedures considered in this study can disperse GNPs in water without causing any basal or vacancy defects in graphene sheets and reduce the size of graphene flakes. The use of ultrasonication together with high shear mixing leads to the smallest size graphene sheets. When the GNPs are added to the concrete mixture at a dosage of 0.025%, a maximum increase of 17% in compressive strength is observed, while no significant effect of GNPs on the flexural strength is noticed.

## 3. 2. Materials

Portland cement type I/II, natural sand, and coarse aggregates with a maximum size of 12.5 mm are used to prepare concrete samples. Table 3-1 shows the chemical composition of the cement used in this study. Grade M-25 GNP manufactured through mechanical exfoliation is used as nano reinforcement. Table 3-2 shows various properties of the M-25 GNPs. A polycarboxylate-based superplasticizer is utilized to help dispersion of the GNPs and achieve the desired workability.

**Table 3-1.** Chemical composition of cement

| **Chemical composition (%)** | **Cement** |
|---|---|
| $SiO_2$ | 21.0 |
| $Al_2O_3$ | 4.9 |
| $Fe_2O_3$ | 2.3 |
| CaO | 64.8 |
| MgO | 1.7 |
| $Na_2O$ | 0.3 |

**Table 3-2.** Properties of GNP M-25

| **Properties** | **Values** |
|---|---|
| Surface Area ($m^2/g$) | 120~150 |
| Diameter (μm) | 25 |
| Thickness (nm) | 6-8 |
| Density (g/cc) | 2.2 |
| Carbon Content (%) | >99.5 |
| Tensile Modulus (GPa) | 1000 |
| Tensile Strength (GPa) | 5 |

## 3. 3. Dispersion and Mixing Procedures

In this study, the wet dispersion of GNPs is considered for the fabrication of GNP-reinforced-cement composites. To improve stability and dispersion of GNPs in water, a polycarboxylate-based superplasticizer is used as surfactant. Polycarboxylate-based superplasticizer consists of a main carbon chain with carboxylate groups and polyethylene oxide (PEO) side chains. When superplasticizer is dissolved in water, the main carbon chains are absorbed at the interface between GNPs and water and the PEO side chains extend out from GNPs. These side chains can help GNPs to be apart from each other and allow water to surround particles, which is called steric hinderance. Besides of the physical separation generated from long side chains, the main chain imparts a slight negative charge that make GNPs particles repel each other [131]. Since polycarboxylate-based superplasticizer are already used in cementitious composites and have shown to be effective in dispersion of carbon-based materials in cement matrix [66,132], they are selected to serve as surfactant in this study.

For the treatment of the suspension that consists of water, superplasticizer, and GNPs, either only high shear mixing or combination of high shear mixing and ultrasonication is considered. Table 3-3 shows a total of six dispersion methods studied here. Since a dispersion procedure that involves only high shear mixing can be more practical for industrial applications, the first three dispersion techniques involve only high shear mixing with a rotating speed of 5000 rpm for different durations (30 min, 60 min or 90 min). The next three methods follow the same high mixing durations with earlier methods but combine them with 15 minutes of probe ultrasonication at 240 Watts at and amplitude of 40%, and using a probe frequency of 10 kHz. As discussed above, ultrasonication can further facilitate and improve the dispersion of GNPs.

**Table 3-3.** Different dispersion procedures

| Dispersion case | High-shear mixing | Probe ultrasonication |
|---|---|---|
| H1 | 30 min | 0 |
| H2 | 60 min | 0 |
| H3 | 90 min | 0 |
| HU1 | 30 min | 15 min |
| HU2 | 60 min | 15 min |
| HU3 | 90 min | 15 min |

Once the dispersion of GNPs into water is completed, all dry materials including cement, sand and coarse aggregates are added into concrete mixer and are mixed for 30 s. Then, the GNP suspension is added and all materials are mixed for three min and then cast into molds.

## 3. 4. Sample Preparation

Control concrete mixture is designed as per ACI 211 [133] and then modified to explore the effect of GNPs on the strength properties of concrete. Water : binder ratio of concrete remains constant at 0.5 in all batches and binder : fine aggregates : coarse aggregates ratio is taken as 1:2:2. First, four concrete mixtures with GNP concentrations ranging from 0.025% to 0.10% by weight of cement are prepared to study the influence GNP ratio. In all of these GNP-reinforced concrete mixtures, the amount of superplasticizer is set to be 0.3 mL per kilogram of cementitious materials and the GNPs are dispersed into water and superplasticizer suspension through high shear mixing for 30 min (dispersion case H1). To evaluate performance of various GNP dispersion techniques, GNP-reinforced concrete specimens with 0.05% GNP ratio are also prepared with five other dispersion methods listed in Table 3-3. A summary of the mixing proportions for different mixes described above is provided in Table 3-4.

For each batch, three 76.2×76.2×279.4 mm prismatic specimens and three Φ101.6×203.2 mm cylindrical specimens are cast for flexural strength tests and compressive strength tests, respectively. All specimens are removed from molds after 24h and stored under a curing condition with a temperature of 23.0 ± 2°C and a relative humidity greater than 95%.

**Table 3-4.** Mixing plan with different GNPs ratios

| Mix name | Dispersion case | Cement (kg/m$^3$) | Water (kg/m$^3$) | GNP (g) | Coarse Aggregates (kg/m$^3$) | Fine aggregates (kg/m$^3$) |
|---|---|---|---|---|---|---|
| Control | - | 433.1 | 216.5 | 0 | 870.4 | 811.3 |
| GC1-0.025 | H1 | 433.1 | 216.5 | 108.3 | 870.4 | 811.3 |
| GC1-0.05 | H1 | 433.1 | 216.5 | 216.5 | 870.4 | 811.3 |
| GC1-0.075 | H1 | 433.1 | 216.5 | 324.8 | 870.4 | 811.3 |
| GC1-0.10 | H1 | 433.1 | 216.5 | 433.1 | 870.4 | 811.3 |
| GC2 | H2 | 433.1 | 216.5 | 216.5 | 870.4 | 811.3 |
| GC3 | H3 | 433.1 | 216.5 | 216.5 | 870.4 | 811.3 |
| GC4 | HU1 | 433.1 | 216.5 | 216.5 | 870.4 | 811.3 |
| GC5 | HU2 | 433.1 | 216.5 | 216.5 | 870.4 | 811.3 |

| | | | | | | |
|---|---|---|---|---|---|---|
| GC6 | HU3 | 433.1 | 216.5 | 216.5 | 870.4 | 811.3 |

## 3. 5. Test Methods

To evaluate the effectiveness of different GNP dispersion methods listed in Table 3, the droplets are extracted from the GNP suspension using a pipette and placed on silica dioxide substrates and glass substrates. A control case for the dispersion is also prepared by adding as-received GNPs into water and stirring them for 15 s. Scanning electron microscopy (SEM) images are obtained after natural drying of GNP samples on silica dioxide substrates with a 10 kV beam and magnification varying from 500× to 5000×. Raman spectroscopy of these samples are acquired by Renishaw Raman Spectroscopy with a 514 nm excitation laser and an 1800 g/mm grating, and spectra are recorded with a 50× lens. For each sample, typically six spectra are recorded and averaged.

In addition, GNPs flakes are visualized using optical microscopy with a high magnification to measure the lateral size distribution of the flakes. At least 1000 flakes are measured and the contrast of images is enhanced with suitable filters. A MATLAB code is used to first convert the original images to a binary base image as shown in Figure 3-1 and then compute the lateral size of each particle present in the image.

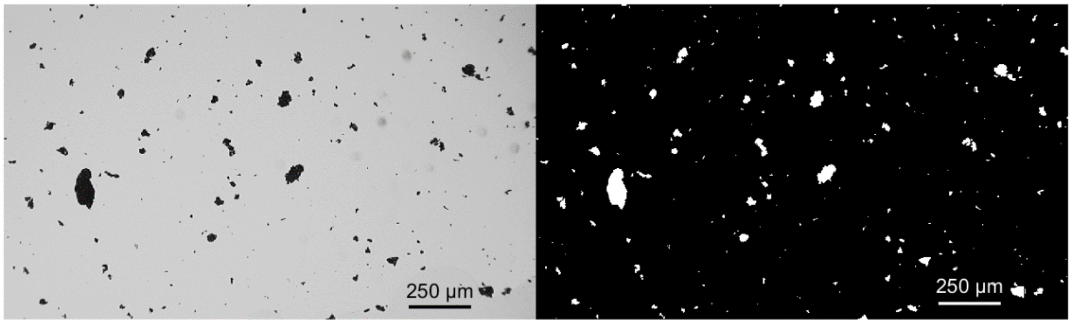

(a) (b)

**Figure 3-1.** (a) Original optical microscopy image of exfoliated graphene flakes; and (b) its binary base image obtained with MATLAB.

Compressive strength test and flexural strength test are performed at 28 days as per ASTM C 39 and ASTM C 78, respectively. For compressive tests, three prismatic specimens are tested at a loading rate of 0.25 MPa/s. A four-point bending set up is used for the flexural strength tests. The load is applied at a constant rate such that the tensile stress at the bottom face of the specimens increases at a rate of 1.2 MPa/min. The flexural strength of the specimen is calculated as:

$$R=\frac{PL}{bd^2} \tag{3-1}$$

where $R$ is the modulus of rupture (MPa), $P$ is maximum applied load (N), $L$ is span length (mm), $b$ is average width of specimen (mm), and $d$ is the average depth of specimen (mm).

## 3. 6. Structural Characterization of Dispersed of GNPs

According to manufacturer's datasheet, the GNPs used in this study have a mean diameter of 25 $\mu$m, with 10% of them have a diameter less than 6 $\mu$m, and an average thickness of 6-8 nm. Figure 3-2(a) shows the morphology of the GNPs provided by the manufacturer. The image shows the GNPs with a diameter ranging from 3 to 25 $\mu$m and with thin layers. Note that the GNPs are provided in dry powder form. However, when the GNPs are dispersed in water, they tend to flocculate due to hydrophobic nature of graphene sheets. The GNPs are formed face to face with large contact area and strong bonding force, leading to agglomerates with maximum dimensions about 100 $\mu$m and those larger than 150 $\mu$m as shown in Figures 3-2(b) and 3-2(c).

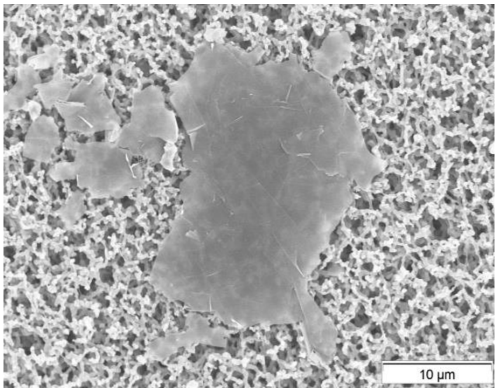

(a)

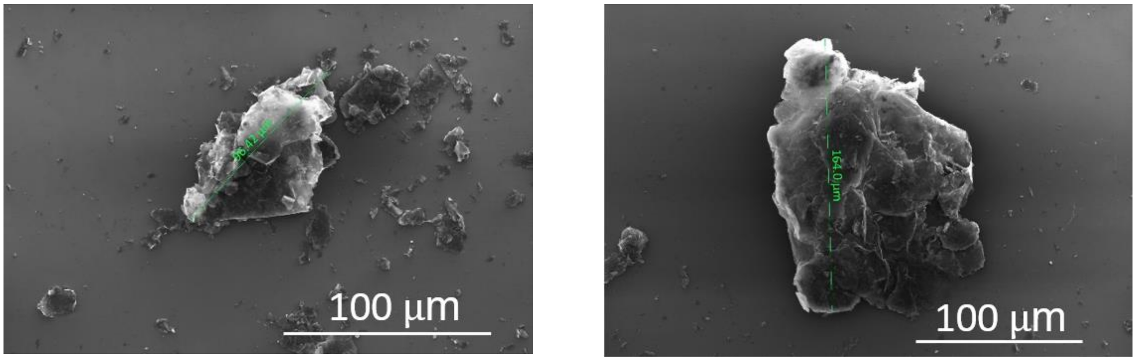

(b) (c)

**Figure 3-2.** (a) Morphology of GNPs obtained from manufacturer; (b) and (c) SEM images of GNPs dispersed in water.

To explore the effectiveness of different GNP dispersion procedures, lateral sizes of graphene flakes obtained from each dispersion case are computed by analyzing the optical microscopy images. In order to better analyze size distribution and effectively compare the results, the histograms of lateral sizes are plotted and then fitted with different statistic models [134–136]. In particular, the experimental data are fitted by 15 commonly used distribution models such as generalized extreme value (GEV), log-logistic, and log-normal distributions. Using Bayesian Information Criterion (BIC), the GEV distribution model is found to be the best-fit model for all dispersion cases and employed to fit the experimental data as shown in Figure 3-3. The GEV model is a probability density function (PDF) described by parameters $\mu$, $\sigma$ and $k$. Table 3-5 presents the GEV distribution parameters and the comparison of experimental data and the fitted data. For some dispersion cases, the models very closely predict both the average size of flakes and the median of flake size. However, in some other cases such as HU2, H3, and HU3 cases, the fitted data is more accurately described with the median flake size compared to the average flake size. Thus, the median value of obtained GEV distributions is more robust in describing the experimental data.

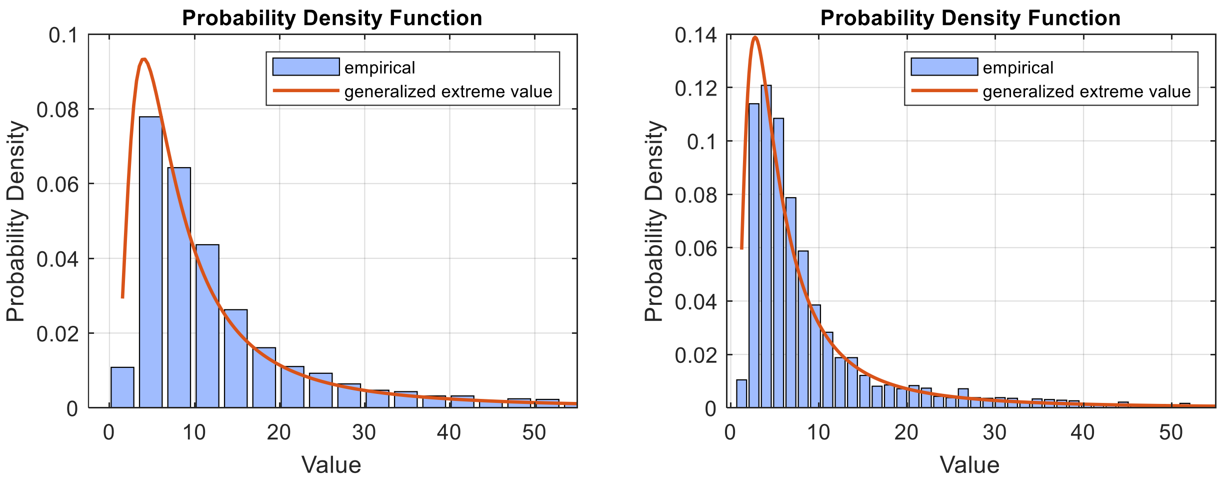

(a) (b)

**Figure 3-3.** A comparison of different distribution models and the experimental data for (a) as received GNP; and (b) GNPs suspension with high shear mixing of 90 min.

**Table 3-5.** GEV distribution parameters and comparison of experimental data with fitted data

| **Dispersion case** | **Distribution parameters** | | | **Average of flake size ($\mu$m)** | | **Median of flake size ($\mu$m)** | |
|---|---|---|---|---|---|---|---|
| | **$\mu$** | **$\sigma$** | **k** | **Exp. data** | **Fit data** | **Exp. data** | **Fit data** |
| Control | 6.017 | 5.685 | 0.645 | 14.4 | 14.3 | 7.8 | 8.0 |
| H1 | 5.478 | 3.879 | 0.492 | 11.2 | 11.4 | 7.2 | 7.0 |
| H2 | 4.964 | 3.524 | 0.556 | 11.4 | 11.3 | 6.4 | 6.4 |
| H3 | 4.102 | 3.154 | 0.646 | 9.6 | 11.5 | 5.5 | 5.4 |
| HU1 | 4.118 | 2.671 | 0.510 | 8.2 | 8.4 | 5.3 | 5.2 |
| HU2 | 2.024 | 1.490 | 0.665 | 4.7 | 5.8 | 2.7 | 2.6 |
| HU3 | 1.854 | 1.318 | 0.703 | 4.4 | 5.6 | 2.5 | 2.4 |

Figure 3-4(a) compares the size distribution curves for the control dispersion case, which consists of addition of GNPs into water and hand stirring, as well as different dispersion cases where GNPs are dispersed into water and superplasticizer suspension through different durations of high shear mixing and ultrasonication. It can be seen that increasing high shear mixing duration both decreases the median flake size and increases the amount of smaller size flakes.

Compared to median flake size of 7.8 $\mu$m for the control case, the high shear mixing with 30 min, 60 min or 90 min produce median graphene flake sizes of 7.2 $\mu$m, 6.4 $\mu$m, and 5.5 $\mu$m. Figure 3-4(b), 3-4(c) and 3-4(d) compare the lateral size distributions of graphene flakes obtained with different duration of high shear mixing and with or without additional 15 min probe ultrasonication. It can be seen that when the probe ultrasonication is applied, considerably more flakes with smaller size are produced, especially in dispersion cases with 60 min and 90 min high shear mixing. In these cases, the median flake size also decreases largely. In particular, when the 60 min high shear mixing is combined with 15 min probe ultrasonication, the median flake size reduces to 2.7 $\mu$m compared to flake size of 6.4 $\mu$m obtained from 60 min high shear mixing. Similarly, the median flake size decreases from 5.5 $\mu$m to 2.5 $\mu$m when 90 min high shear mixing is combined with 15 min probe ultrasonication.

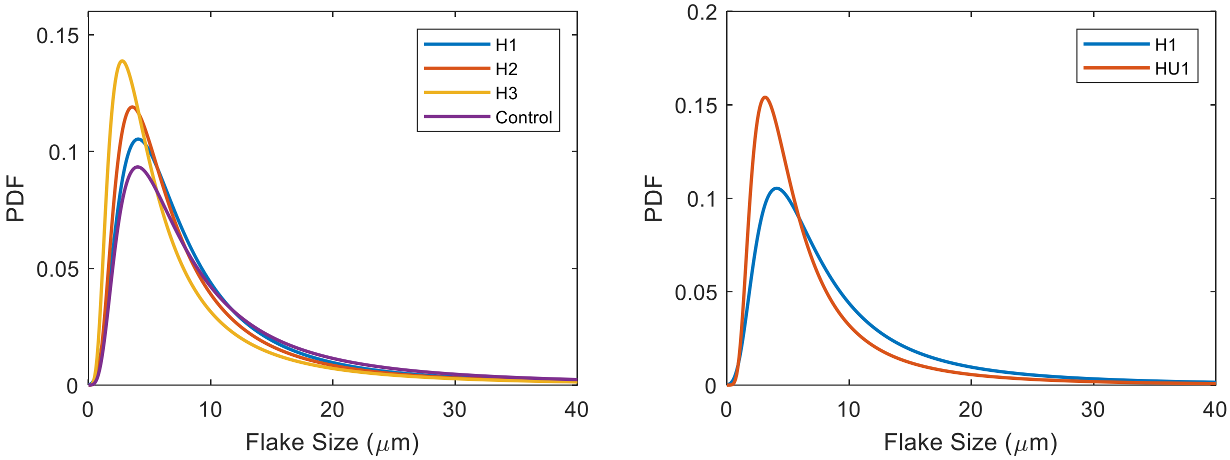

(a) (b)

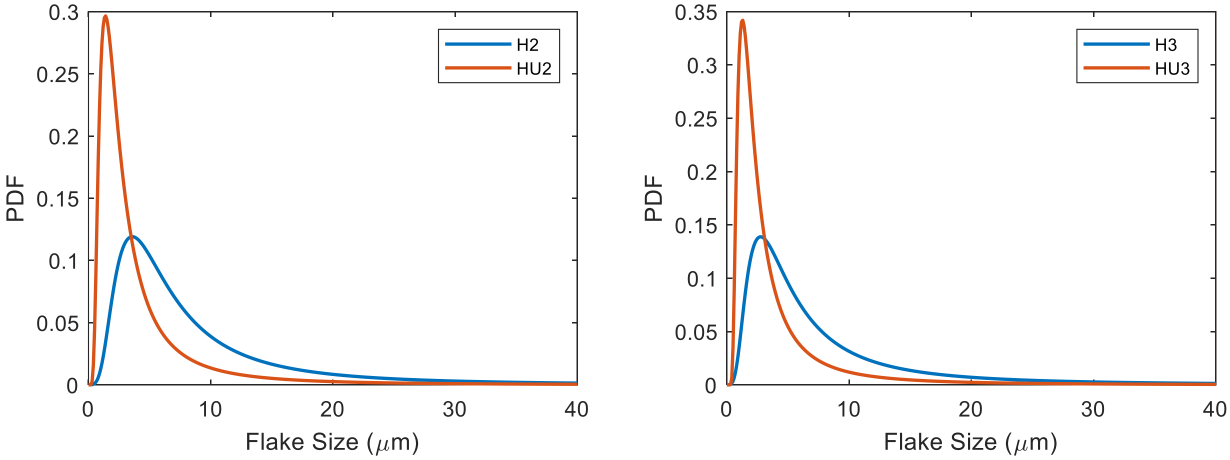

(c) (d)

**Figure 3-4.** Probability distribution of flake size for (a) GNPs dispersed with different high shear mixing durations and control case; GNPs dispersed with (b) 30 min (c) 60 min (d) 90 min high shear mixing and with and without 15 min probe ultrasonication.

Raman spectroscopy is a non-destructive tool that can provide a quick and facile structural and quality characterization of graphene-based materials [42]. The most common features in Raman spectra of graphitic materials are a low intensity D band (~1350 cm$^{-1}$), a strong intensity G band (1582 cm$^{-1}$) and a moderate intensity 2D band (2726 cm$^{-1}$). The size and layers of GNPs particles can be analyzed by evaluating the intensity, shape and position of these bands. Raman spectra of all samples are presented in Figure 3-5 with normalized intensity in y-axis.

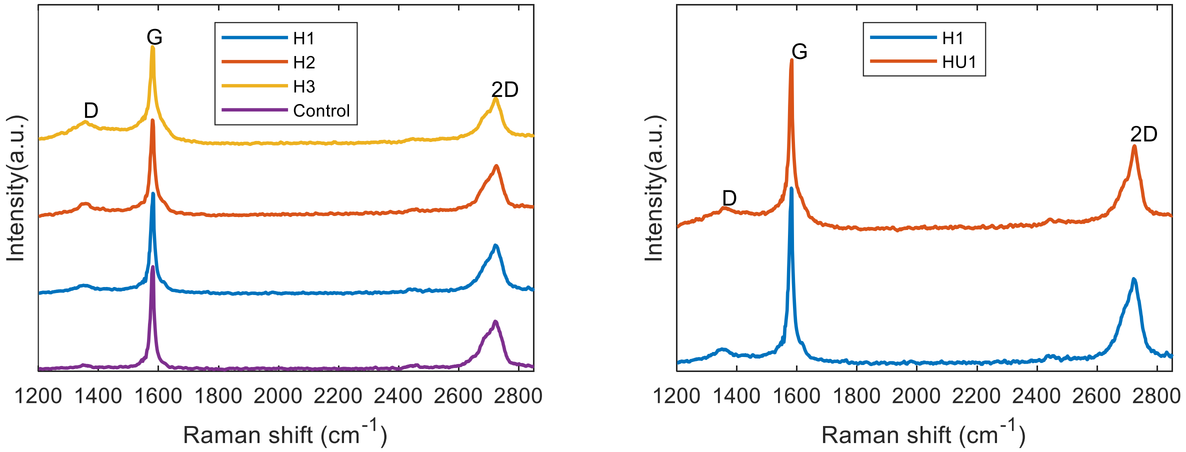

(a) (b)

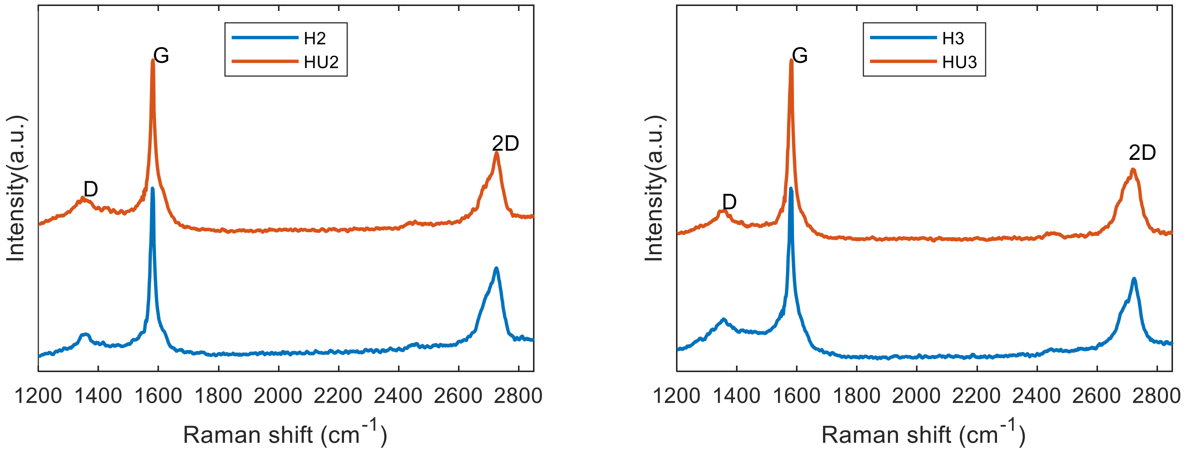

(c) (d)

**Figure 3-5.** Raman spectroscopy results comparing (a) GNPs dispersed with different high shear mixing durations and control case; GNPs dispersed with (b) 30 min (c) 60 min (d) 90 min high shear mixing and with and without 15 min probe ultrasonication.

The G band that indicates the sp$^2$ carbon network (C-C atoms) appears at 1582 cm$^{-1}$ in all samples. A higher intensity of G band implies a high crystallinity of graphene. In addition, the full width at half maximum (FWHM) of G band can inform about the disorder degree of carbon atom distribution [137]. The D bands in Raman spectra of graphitic materials are features associated with the presence of defects and disorders in C-C bonds (sp$^3$ defects) [78]. The presence of D band does not directly indicate structural defects (sp$^3$ or vacancy defects). The edge of graphene sheets, i.e., the number of C-atoms with dangling bonds also acts as defects. The ratio of D band and G band intensities ($I_D/I_G$) is commonly used to evaluate the presence of defects but it does not inform about the type of the defect. Compared to control dispersion of GNPs, $I_D/I_G$ ratio increases when the GNPs are treated with high shear mixing and ultrasonication, indicating edge defects are introduced. When only high shear mixing is used for the dispersion (cases H1 to H3), the $I_D/I_G$ ratio always increases for a larger duration of high shear mixing as can be seen from Figure 3-6(a). The addition of 15 min sonication to each high shear mixing dispersion cases increased the $I_D/I_G$ in HU1 and HU2 dispersion cases compared to H1 and H2 cases but resulted a slightly lower value for HU3 case compared to H3. However, $I_D/I_G$ remains considerably lower than one with values in the range of 0.11 – 0.24 for all dispersion cases, indicating the quality of graphene sheets is preserved.

To identify the type of defects observed in this study, the ratio of D band intensity to D' band intensity ($I_D/I_{D'}$) is computed. D' band occurs as a shoulder on the G band and is also related to defect. A value of $I_D/I_{D'}$ below 3.5 indicates that the nature of defects is edge or boundary related [86]. From Figure 3-6(a), it can be concluded that there are no shear-induced vacancy defects or basal defects in any of GNP suspensions since the $I_D/I_{D'}$ ratio is below 3.5 for all cases. This can be also confirmed with the examination of FWHM of G band for the studied dispersion cases. If the sp$^3$ defects are present, then the FWHM of G band considerably increases [138]. Here, in all dispersion cases, the FWHM of G band remained in the range of 16 – 19 cm$^{-1}$. A slight decrease in the FWHM of G in most of dispersion cases where high shear mixing with and without sonication compared to control case suggests an improvement in disorder degree of C-atom distribution [137]. Overall, increase in defects, i.e. in the $I_D/I_G$ ratio, is due to the fragmentation of GNPs, which increased the number of particles and edge defects [79]. This indicates smaller flake size are obtained with increasing duration of high shear mixing or ultrasonication, which confirms the findings obtained from optical microscopy analyses.

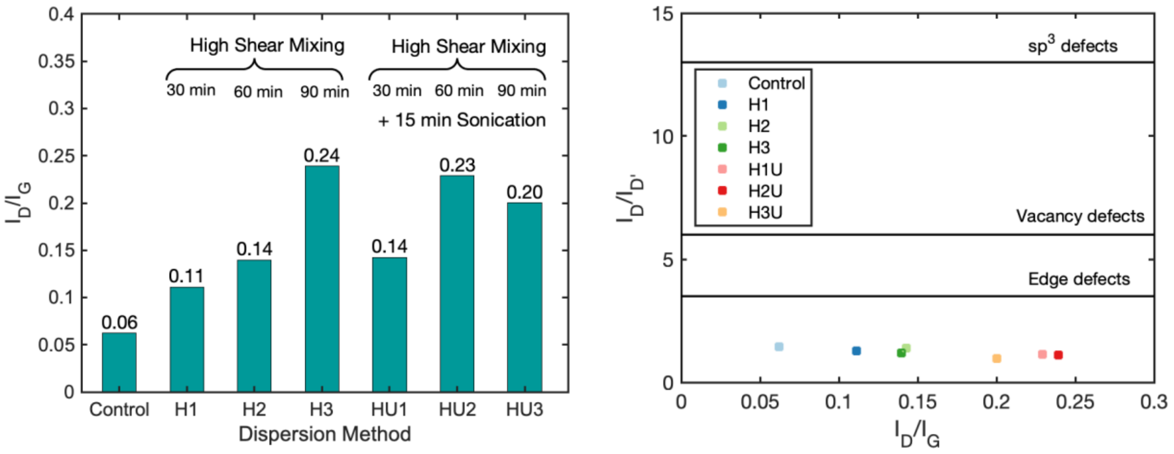

(a)

(b)

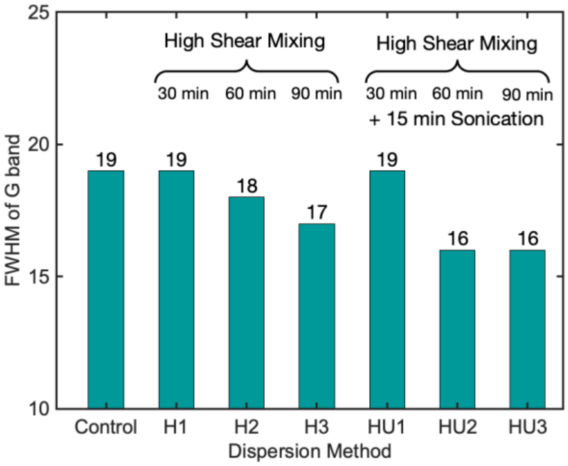

(c)

**Figure 3-6.** The variation of (a) $I_D/I_G$, (b) $I_D/I_{D'}$ and (c) FWHM of G band variation with GNP dispersion method.

Studying the shape, intensity, and position of 2D band provides information on the exfoliation degree and the number of layers in dispersed GNPs. For single layer graphene, the 2D band, which occurs at less than 2700 $cm^{-1}$, exhibits a single Lorentzian feature with a FWHM from 20 ~ 25 $cm^{-1}$ and an intensity ratio of 2D band to G band ($I_{2D}/I_G$) of approximately 2.0 [80–82]. As the number of graphene layers increases, the 2D band can be fitted by multiple Lorentzian features, resulting in a wider, shorter band with lower $I_{2D}/I_G$ [83,84].

Here, the position of 2D band in all dispersion cases is either 2726 or 2727 $cm^{-1}$ and the FWHM of 2D band ranges from 57 to 75 $cm^{-1}$. In addition, $I_{2D}/I_G$ for all GNP suspensions is in the range of 0.43-0.50, which is lower than 2.0 as shown in Figure 3-7. Therefore, the graphene flakes obtained after the treatment of GNPs in all dispersion cases consist of multi-layer graphene sheets [139,140]. The $I_{2D}/I_G$ ratio did not change considerably compared to control case in all the dispersion cases except dispersion case HU3, indicating no significant exfoliation of the GNPs occurred in most cases. A relatively lower value of $I_{2D}/I_G$ ratio observed for the HU3 dispersion case could be due to re-agglomeration and restacking of smaller size but larger quantity graphene sheets produced with this dispersion method [138].

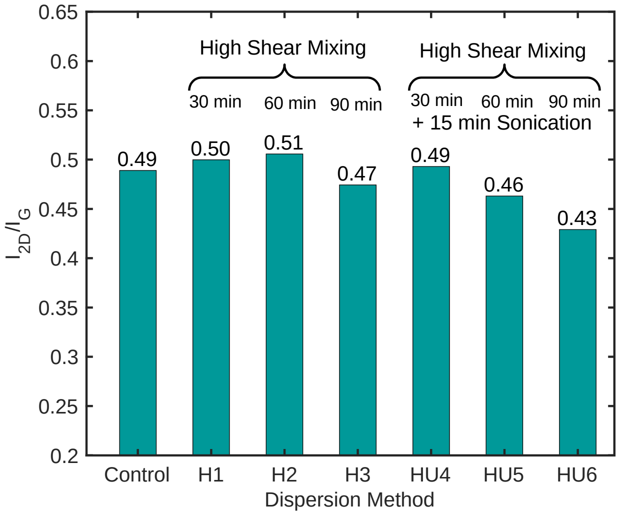

**Figure 3-7.** $I_{2D}/I_G$ for all GNP dispersion cases.

Figures 3-8 to 3-10 show the SEM images of the GNPs prepared with different dispersion methods. In these images, the GNP particles with lateral sizes varying from 6 $\mu$m to 183 $\mu$m are observed. In each GNPs suspension, large GNP agglomerates still exist. However, with increasing duration of high shear mixing (dispersion cases H1, H2, and H3), more GNP particles with smaller size appear in the images. In addition, comparing the SEM images of the GNPs with and without probe ultrasonication, it can be concluded that the GNP suspensions where probe ultrasonication is combined with high shear mixing contain smaller GNPs. These observations are in line with the results obtained from optical microscopy and Raman spectra.

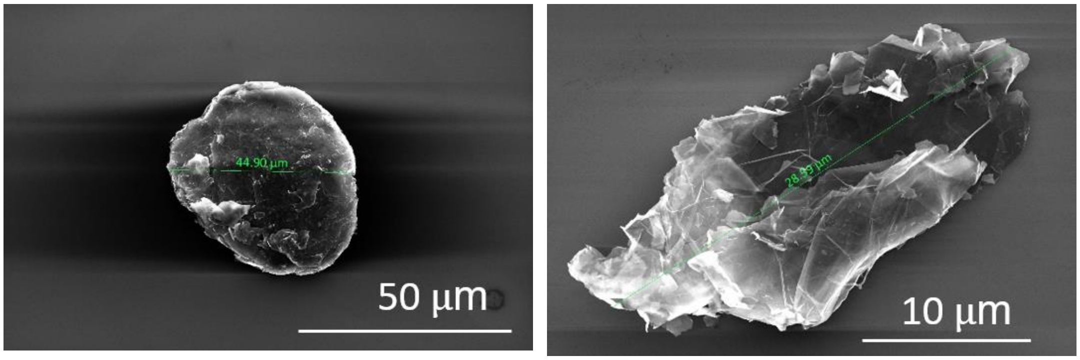

(a)

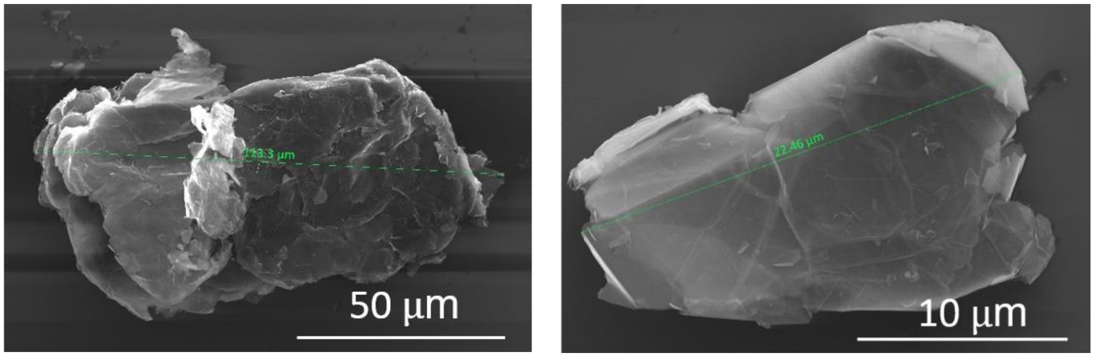

(b)

**Figure 3-8.** SEM images of GNPs for dispersion cases (a) H1 and (b) HU1.

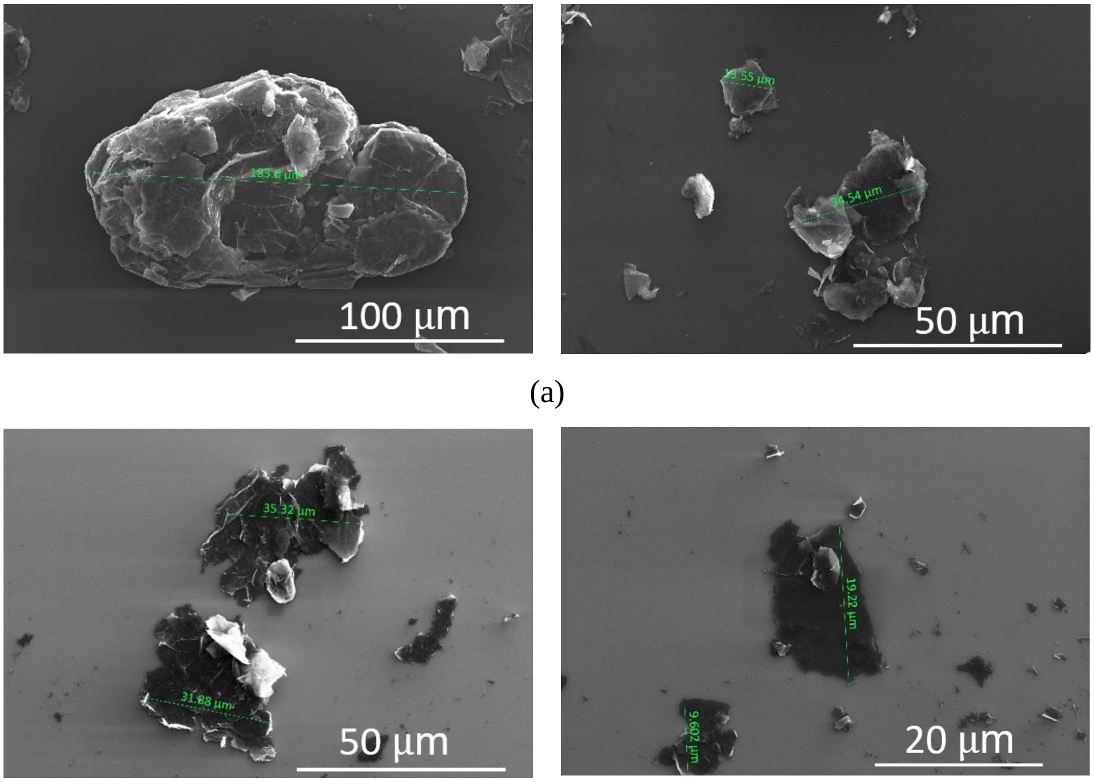

(a)

(b)

**Figure 3-9.** SEM images of GNPs for dispersion cases (a) H2 and (b) HU2.

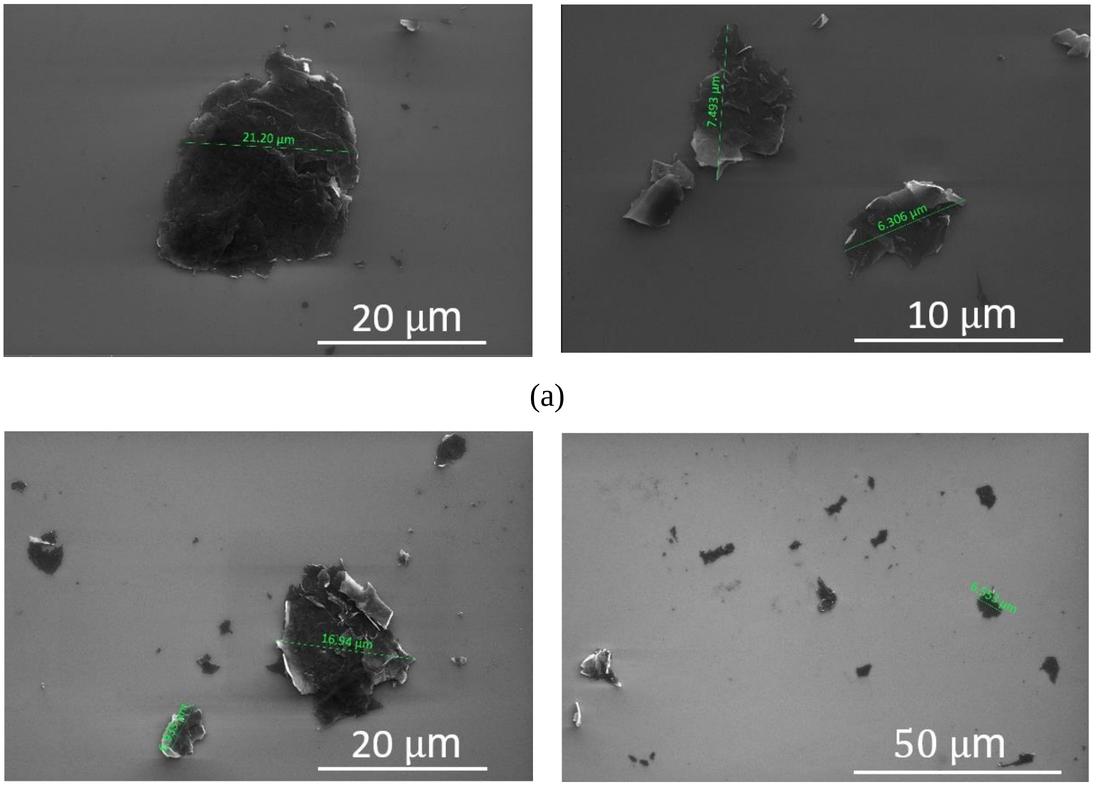

(a)

(b)

**Figure 3-10.** SEM images of GNPs for dispersion cases (a) H3 and (b) HU3.

## 3. 7. Mechanical Properties of GNP-reinforced Concrete

Earlier studies have identified potential mechanisms that lead an enhancement in mechanical properties of cementitious composites, mostly cement pastes and mortars, with the addition of GNPs. Two mechanisms mentioned frequently are nucleation effect and filling effect. The graphene sheets can serve as nucleation sites for the C-S-H crystals, and promote the hydration reactions. As graphene sheets bond to C-S-H crystals, they can also increase the strength of C-S-H gels [141]. In addition, incorporating GNPs into cementitious matrix can eliminate the weak cement hydration crystals, which are mostly disorderedly stacked needle-shaped and bar-shaped crystals, and produce finer and denser microstructure [142]. This decrease in porosity leads to an improvement in mechanical properties.

Figure 3-11 shows the compressive strength and flexural strength test results for the concrete specimens with different GNP concentrations. As can be seen in Figure 3-11(a), with the addition of 0.025% and 0.05% GNPs the compressive strength of concrete increased by 17% and 12%, respectively. However, when GNP ratio is further increased to 0.075% and 0.1%, the compressive strength of concrete decreased by 12% and 13%, respectively, compared to the control specimen. As discussed above, the improvements at lower GNP ratios could be attributed to the role of graphene as nucleation site during the hydration and improvement in the microstructure and porosity of concrete. This results in considerably tight cross-linking structures, which are also shown in SEM images of specimens with 0.05% GNPs in Figure 1-12. However, at higher GNP reinforcement ratios, more agglomerations of GNPs reduce available nucleation sites for hydration and creates weak zone inside concrete thereby decrease the strength. Note that the results obtained this study are in agreement with those obtained in Chen [118] where a maximum increase of 22% in compressive strength of concrete observed for a GNP ratio of 0.05% and then a decrease in compressive strength reported for increasing GNP ratios.

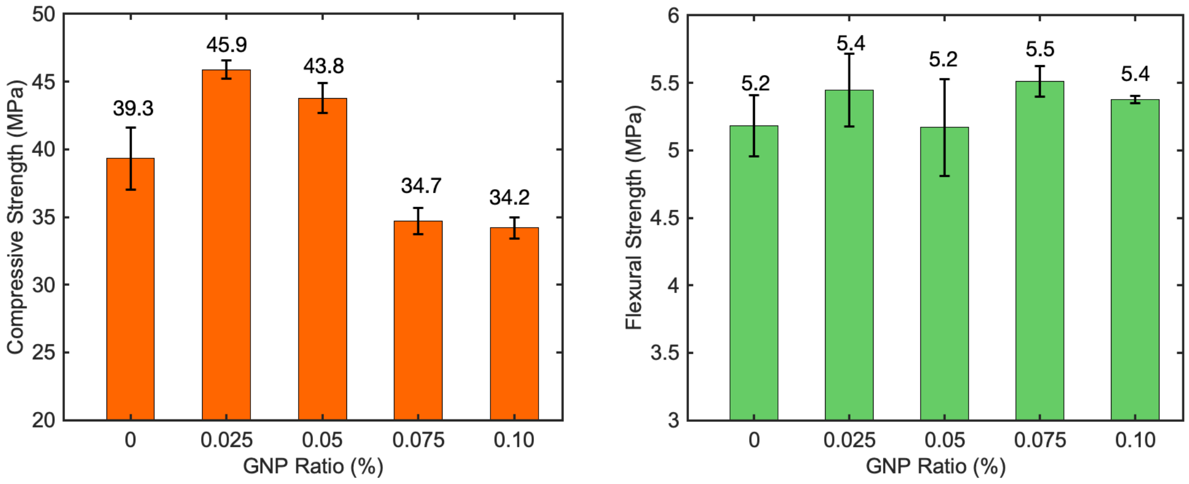

(a) (b)

**Figure 3-11.** (a) Compressive strength and (b) flexural strength of GNP-reinforced concrete with different GNP ratios.

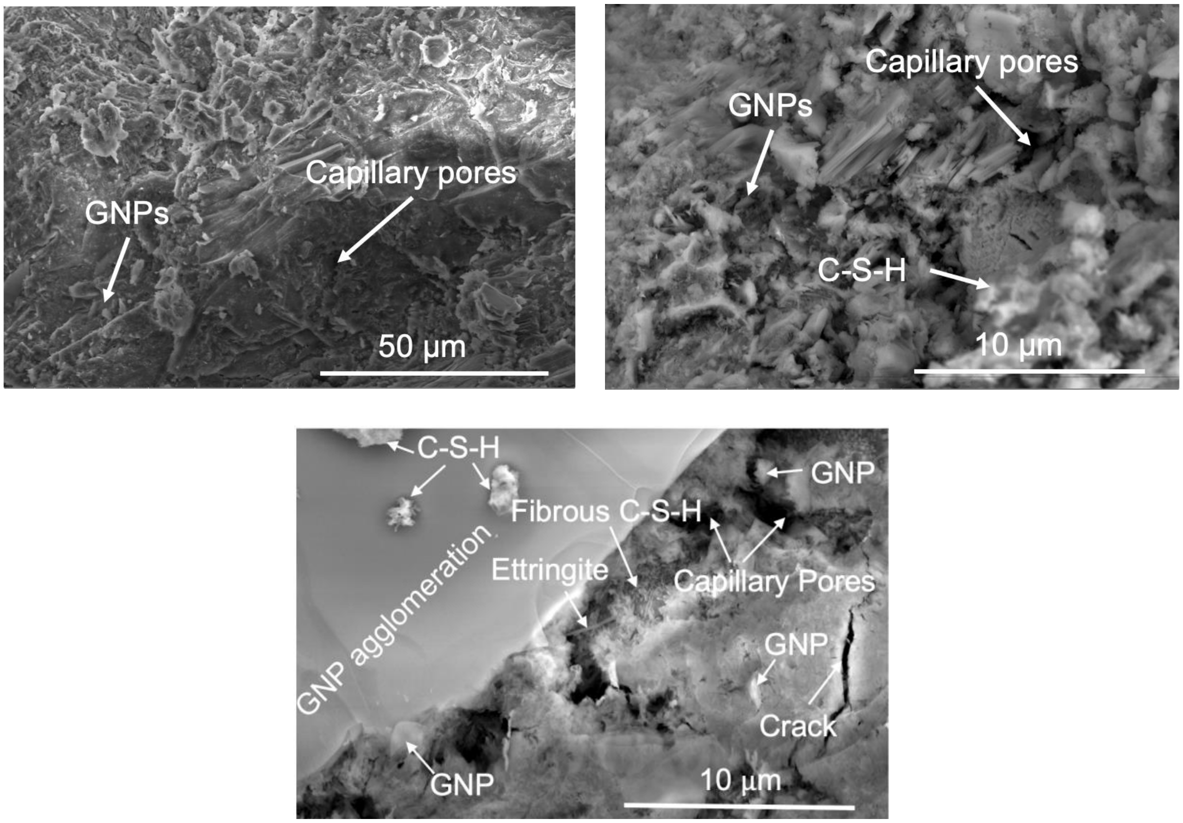

**Figure 3-12.** SEM images of specimens with 0.05% GNPs.

Due to the bridging effects of graphene sheets, an increase in flexural strength of cement pastes or mortar composites have mostly been reported in the literature. However, the flexural strength of concrete is not affected considerably by GNP addition in this study. In particular, the flexural strength of concrete specimens with various GNP concentrations increased only by up to 6% compared to the control mixture. A similar almost null effect of GNPs on the flexural strength of concrete composites was also observed in [117]. Although GNPs are planar materials and have high tensile strength, the full advantages of GNP reinforcement in flexural strengthening can be obtained when GNPs with high aspect ratios are used. The interfacial transition zone (ITZ) between coarse aggregates and cement matrix plays a critical role in mechanical properties of concrete. The size of graphene sheets might not be sufficient to offer strengthening effect to the microstructure of the ITZ in concrete composites, while the GNPs may mitigate the weak zone in cement paste and mortar composites [117]. In addition, a recent study [143] reported only 5.5% increase in interfacial bond strength between coarse aggregates and mortar matrix in three-point bending tests when multi-layer graphene sheets were added at 0.1% concentration ratio. However, when the reinforcement ratio was increased to 0.3%, the enhancement in the bond strength was reached to its maximum value of 28%. Therefore, small particle size and insufficient reinforcement could be the reason for only slight increases in flexural strength observed in this study.

Figure 3-13 presents test results for the concrete specimens containing 0.05% GNPs and fabricated with different dispersion procedures. When the results obtained from the specimens prepared only high shear mixing of GNPs (specimens GC1 to GC3) are compared, it can be seen that increasing high shear mixing duration from 30 min to 60 min then to 90 min does not have any important effect on compressive strength and flexural strength of the GNP-reinforced concrete specimens. When 15 min ultrasonication is combined with 30 min or 60 min high shear mixing when preparing the GNP suspension, this additional sonication does not change the compressive strength of GNP-reinforced concrete (specimens GC4 and GC5) compared to those prepared only by high shear mixing of GNPs (specimens GC1 and GC2). On the other hand, the specimens prepared by 90 min high shear mixing and 15 minutes ultrasonication of GNPs (specimen GC6) exhibit a 17% decrease in compressive strength compared to the specimens prepared by only 90 min high shear mixing of GNPs (specimen GC3). Note that this dispersion case results in the smallest size for the GNPs, as confirmed by the characterization results presented in previous section, and a higher chance of re-agglomeration was reported in literature for smaller size graphene sheets [138]. Therefore, the decrease in specific surface area due agglomeration and the decrease in aspect ratio as a result of fragmentation of GNPs in specimen GC6 might be the reason for the observed reduction in the compressive strength of this specimen. Also, note that the lowest value of the flexural strength of GNP-reinforced concrete specimens was observed for the specimen with the smallest graphene flake size (specimen GC6). There was no significant change in flexural strength with different dispersion techniques considered here. This can be attributed to the fact that the size and aspect ratio of the graphene sheets obtained with these dispersion cases and the used GNP concentration (0.05%) may not be optimal for flexural strengthening as discussed earlier.

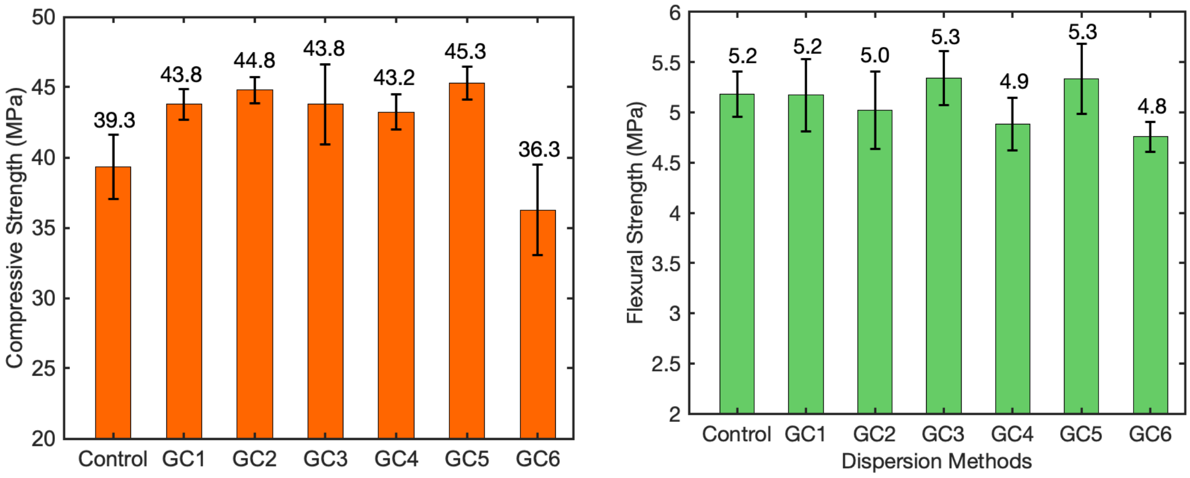

(a) (b)

**Figure 3-13.** (a) Compressive strength and flexural strength of GNP-reinforced concrete prepared by different dispersion procedures.

## 3. 8. Summary

In this study, an effective dispersion method and an optimal concentration for the incorporation of GNPs into concrete mixtures are investigated. To this end, the concrete specimens with varying concentrations of GNPs are prepared and different dispersion methods for the addition of GNPs into concrete mixtures are considered. Various characterization techniques based on optical microscopy and Raman spectroscopy are used to assess the dispersion of GNPs in water, while the SEM is used to evaluate the dispersion of GNPs both in water and cementitious matrix. The effects of GNPs on the hardened properties of the concrete mixtures are evaluated through compressive strength and flexural strength. The key outcomes of the study are as follows:

- The dispersion of GNPs into water in the presence of polycarboxylate-based superplasticizer through only high shear mixing or together with ultrasonication produces smaller size graphene sheets and exhibits good dispersion performance in water.
- Both increasing duration of high shear mixing or combining high shear mixing with 15-minute probe ultrasonication reduce the mean flake size. However, probe ultrasonication is more prominent in reducing the flake size of GNPs.

- None of the dispersion durations considered in this study produces shear-induced vacancy defects or basal defects in graphene sheets. However, the considered dispersion methods also could not exfoliate GNPs into few-layer graphene sheets.
- The compressive strength of concrete is improved at low dosages of GNPs (0.025% and 0.05%) as GNPs can eliminate the weak cement hydration crystals with tight cross-linking structures. However, higher ratios of GNPs result in a decrease in the compressive strength, which might be attributed to the weak zone in the concrete matrix created by agglomeration of GNPs.
- GNPs at any concentration considered in this study do not have a significant influence on the flexural strength. This could be attributed to small size and aspect ratio of graphene sheets obtained in this study after dispersion in water.
- Although the considered GNP dispersion techniques produces uniform dispersion of GNPs in water, their effectiveness in creating strong bonds between cement hydration products and graphene sheets as well as in preventing agglomerates in alkaline cementitious environment is limited. Future studies are needed to develop a dispersion approach that can lead to consistent and higher improvements in mechanical properties of concrete composites.

# 4. EFFECTS OF GNPs ON TENSILE STRENGTH OF MORTAR COMPOSITES

## 4. 1. Overview

This study characterizes tensile behavior of graphene nanoplatelets (GNPs) reinforced cementitious composites using acoustic emissions (AE). Two acoustic sensors were attached to dog-bone specimens that were cast using GNP nano-reinforced mortar composites at concentration levels of 0% to 0.5 % by weight of cement. The specimens were tested under direct tensile loading and the average tensile strength was calculated. AE parameters such as average frequency (AF) and rise time over amplitude (RA) were used to analyze the cracking mode. Average RA was studied to investigate the effect of GNPs reinforcement. A correlation between average acoustic energy and the tensile strength was established. In addition, the acoustic emissions data was analyzed for the localization of cracks along the length of the specimens. Results indicated that the addition of GNPs increased the tensile strength of the cementitious composites by 8%–48%. In addition, the AE analysis revealed a delay in crack initiation shear stress transfer on the matrix -GNPs interface for mortar composites with GNPs and was able to localize cracks as they are initiated.

## 4. 2. Materials

Portland cement type I/II and ASTM graded sand were used to prepare mortar mixtures. GNP M-25 produced by XG Science was employed as nanofillers to reinforce the cementitious matrix. Table 4-1 illustrates the properties of GNP M-25. A superplasticizer, ViscoCrete® Ferro-1000, was used to disperse the GNPs into the mixing water and to increase the workability of the GNP reinforced cementitious composite.

**Table 4-1.** Properties of GNP M-25

| Properties | Values |
|---|---|
| Surface Area ($m^2/g$) | 120~150 |
| Diameter (µm) | 25 |
| Thickness (nm) | 6~8 |
| Density (g/cc) | 2.2 |

| | |
|---|---|
| Carbon Content (%) | >99.5 |
| Tensile Modulus (GPa) | 1000 |
| Tensile Strength (GPa) | 5 |

## 4. 3. Sample Preparation

Initially, the required weight ratios of GNPs and superplasticizer were measured and added to the mixing water. A probe ultrasonicator was utilized to mix the GNP suspension for 10 min. During this time, the cement and sand were mixed in a Hobart commercial mixer at 125 rpm for 2 min. The GNP suspension was then added to the mixer over 10 seconds and the mixing continued for an additional 5 min at 300 rpm. The mortar was then cast into dog-bone molds for tensile testing. Six separate batches of cementitious composites containing different GNP ratios were prepared using the mixing method mentioned above. Each batch of mortar was prepared in accordance with ASTM C109 [144], and a water to cement ratio of 0.485 was maintained. Superplasticizer was used at a dosage of 1.0% in each batch. Each batch had six dog-bone specimens that were casted and tested.

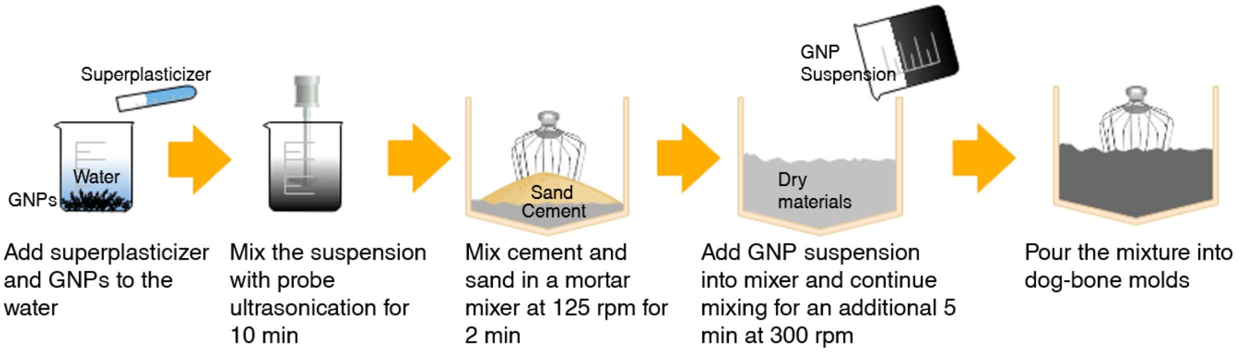

**Figure 4-1.** Typical mixing procedure for GNP reinforced cementitious composites.

## 4. 4. Test Methods

A uniaxial tensile test, configured in displacement-control, was conducted to evaluate the tensile performance of GNP-reinforced cementitious composites. The displacement rate was chosen to be 5 mm/min as per ASTM C307-03. As the mortar specimens cannot be directly fitted into the MTS machine, a set of metal clamps were designed to grip to the specimens. Figure 4-

2(a) illustrates the test setup for the GNP-reinforced cementitious composites with AE sensors. An acoustic emission sensor was attached by wax to the specimen at each end of dog-bone specimens. The AE sensors were narrow band resonant sensors with a sensitivity of 80 dB and resonant frequency of 75 kHz. The linear distance between the two sensors is 203.2 mm. Figure 4-2(b) illustrates the dimensions of the dog-bone specimen with the attached sensors. The thickness of the dog-bone specimens was 12.7 mm and the whole surface of the sensor was in contact with the specimen.

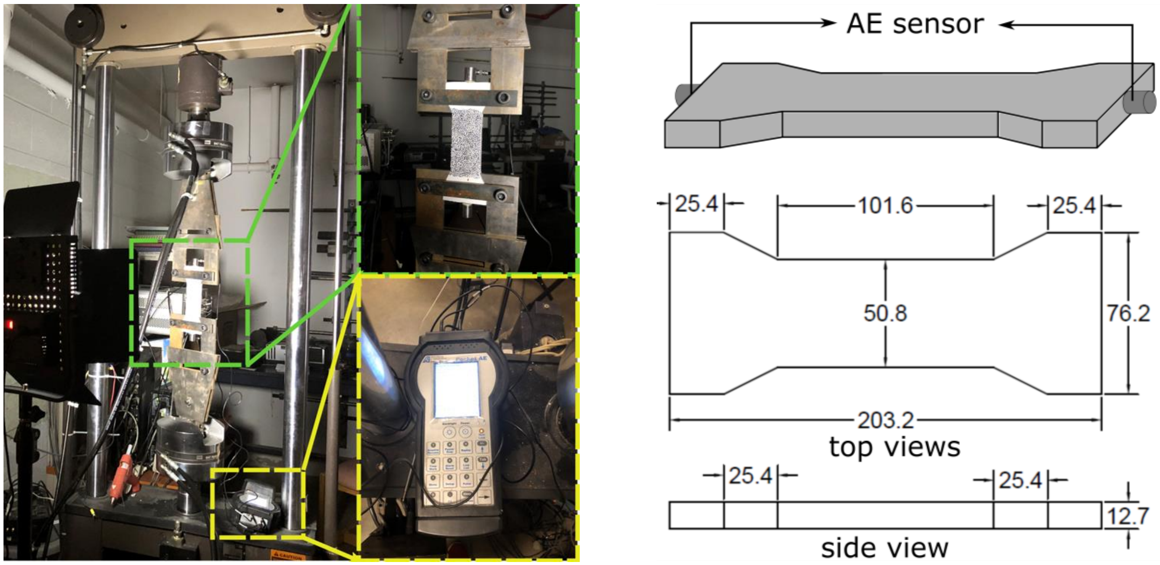

(a) (b)

**Figure 4-2.** (a) Experimental tensile test setup with acoustic emission sensors attached to cementitious composite specimen and (b) Schematic drawings of cementitious composite dog-bone specimen dimensions (unit in mm).

## 4. 5. Tensile Properties of GNP-reinforced Mortar Composites

Figure 4-3 illustrates the average tensile strength of the control specimen and specimens reinforced with GNP. In general, the addition of GNPs at various dosages increased the tensile strength of the specimens. Specimens with 0.1 wt.% GNPs reached the highest average strength, whereas specimens reinforced with 0.5 wt.% GNPs had the lowest increase in tensile strength. GNPs can bridge and block the cracks attributing to its platelet shapes as micro-cracks initiate in the matrix as load is applied. This mechanism impedes and slows the crack propagations. In addition, GNPs can improve interfacial bond strength between GNPs and the matrix due to Van der Waals forces. This enhances the efficiency of stress transfer and enhances the tensile strength [145–148]. In particular, the average tensile strength of the mortar specimens with 0.1 wt.% GNPs was 3.72 MPa, which indicates a 48% increase compared to the control specimen that had a tensile strength of 2.52 MPa. Further increasing GNP concentration did not result in additional enhancement over 0.1% GNP-reinforced mortar composites. This could be attributed to difficulties in dispersion of GNPs at higher dosages as GNP agglomerations forms weak zones inside matrix, leading to stress concentration [118,149]. However, the specimens with 0.2%, 0.3%, and 0.4% GNPs also exhibited 29%, 26%, and 37% increase in tensile strength compared to the control specimen without any GNPs. The specimen with 0.5% GNPs attained a tensile strength of 2.73 MPa, which was only 8% higher than the control specimen. The results indicate that low dosages of GNPs can considerably improve tensile strength.

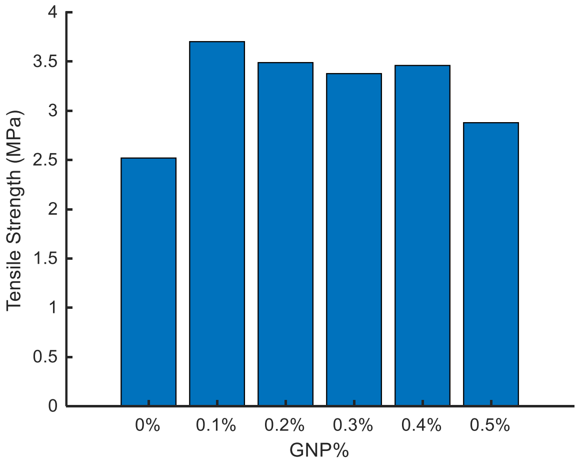

**Figure 4-3.** Average tensile strength of control specimens and GNP-reinforced cementitious composites.

## 4. 6. Acoustic Emissions and Ib-value Analysis

Figure 4-4 illustrates a typical acoustic signal with the acoustic parameters such as amplitude, rise time, duration and counts. First, to eliminate the influence of noise due to the surrounding environment a threshold is set. The maximum measured voltage in a waveform is called amplitude (A). The time interval between the first threshold crossing and the peak voltage of the signal is known as rise time (RT). Duration (D) is the time difference between the first and last threshold crossing, while counts (n) refers to the number of AE signals crossing the threshold. Average frequency (AF) is calculated as AE counts (n) divided by duration (D).

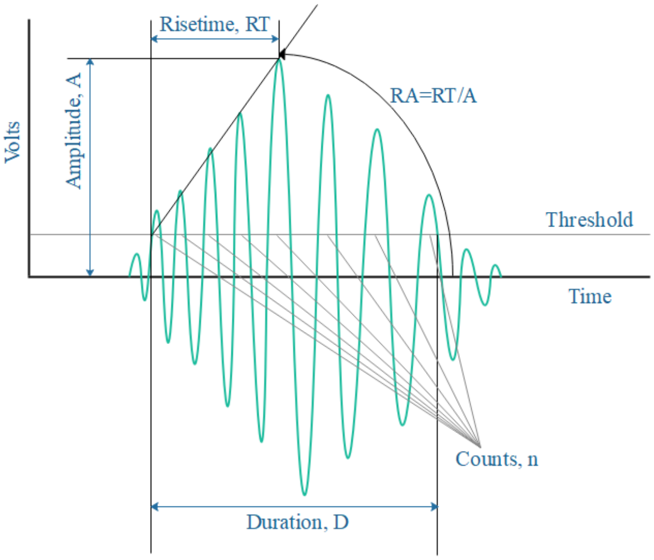

**Figure 4-4.** A typical acoustic emission signal and its characteristics.

The b-value analysis applies Gutenberg-Richter law, and expresses the relationship between the magnitude and total number of earthquakes in any given period, which is usually used in seismology. The formula is given as:

$$log_{10}N = a - bM \qquad 4\text{-}1$$

where *M* is the Richer magnitude of earthquakes; *N* is the total number of the earthquake with a magnitude larger than *M*; *a* and *b* are empirical constants. The parameter *b* is also known as b-value which is commonly selected to be close to 1.0 in seismology. The Richer magnitude of an earthquake is proportional to the logarithm of the maximum amplitude, $A_{max}$, recorded by seismographs, which can be expressed as:

$$M \propto log_{10}A_{max} \qquad 4\text{-}2$$

Modifying Equation 4-1, the b-value analysis can be defined as:

$$log_{10}N = a - b'A_{dB} \qquad 4\text{-}3$$

where $A_{dB}$ is the peak-amplitude of AE events. Colombo et al. [150] proved that b-value analysis can be applied to assess the damage level and cracking size in concrete structures. When cracks initiate, the b-value is high, as cracks grow, the b-value gets smaller. Ib-value, proposed by Shiotani et al. [151], enhances the b-value analysis and can be computed by Equation 4-4:

$$Ib = \frac{\log_{10} N(\mu - \alpha_1 \sigma) - \log_{10} N(\mu + \alpha_2 \sigma)}{(\alpha_1 + \alpha_2)\sigma} \qquad 4\text{-}4$$

where $\mu$ and $\sigma$ are the mean and standard deviation of the AE amplitude among the group of chosen numbers of signals, $\alpha_1$ and $\alpha_2$ are filtering parameters which are both set to 0.5 based on previous studies conducted to investigate acoustic emissions of cementitious composites [152]. Furthermore, AE can be used to define the transient elastic wave from the energy released which occurred with the change of microstructure inside a material [153]. AE hits represent the number of transient elastic wave, which can be an indication for the initiation of micro-cracks. Thus, the larger the value of AE hits, the higher the number of cracks that are initiated.

## 4. 7. Acoustic Emission Analysis of Tensile Test Results

### *4.7.1. Acoustic Emission Parameters Analysis*

Figures 4-5(a) to (f) present the cumulative AE counts and energy against time together with temporal load variation for control specimen and specimens reinforced with GNPs, respectively. Furthermore, the change in cumulative AE activity and energy at different stages are calculated and presented in Figures 4-5(g) and 4-5(h), respectively. For the specimens reinforced with GNPs and during the initial 4s, there are negligible AE activities, indicating limited crack initiation. This might be attributed to the bridging effect of GNPs that can delay the formation of cracks [146]. Beyond the silent period and between 4s to 10s, the AE activity begin to increase due to the initiation of cracks. During this stage, GNPs start to deform and absorb energy leading to a lower AE activity compared to the control specimen. After 10s and until failure, the AE energy and activity increase due to the fracturing of the specimen. At this stage, cracks propagate and branch resulting in reaching the bond strength limit of the GNP-matrix interface [145]. At failure, specimens reinforced with GNPs have a higher AE activity as a larger amount of energy is released due to the fracture of the specimen and breakage or pulling of the GNPs. However, in these four stages, there is not a clear trend between AE parameters and GNP concentrations due to the non-uniform dispersion of GNPs. Therefore, the addition of GNPs can improve the tensile behavior of cementitious composite by crack bridging to impede crack propagation at initial stages, and absorb energy by deforming to slow cracks, while at failure the GNPs are pulled-out.

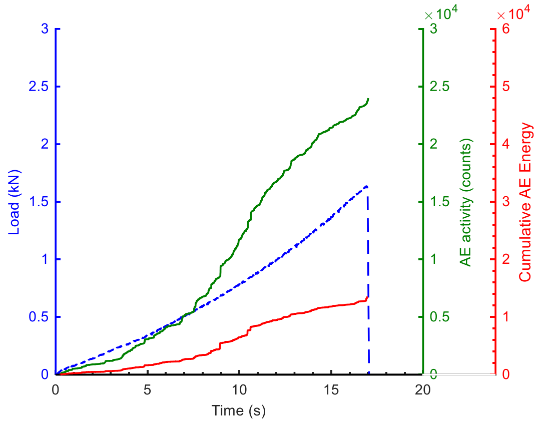

(a)

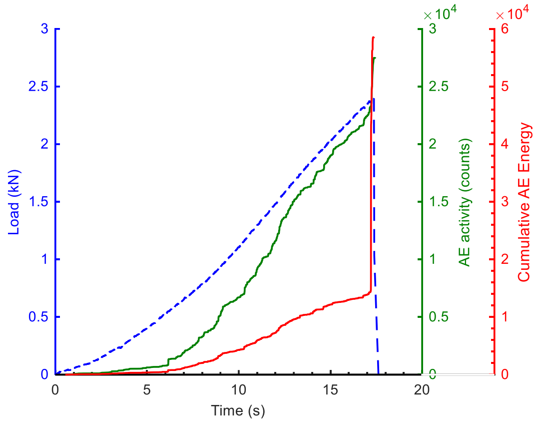

(b)

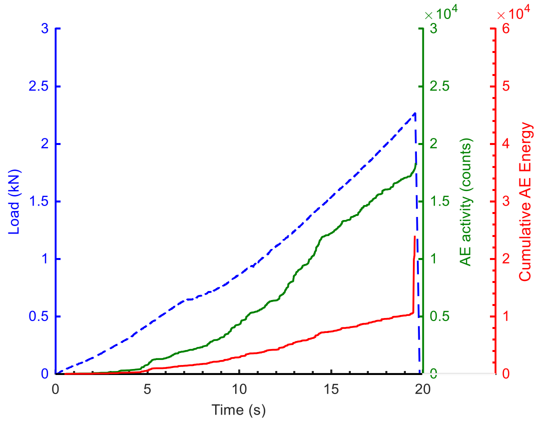

(c)

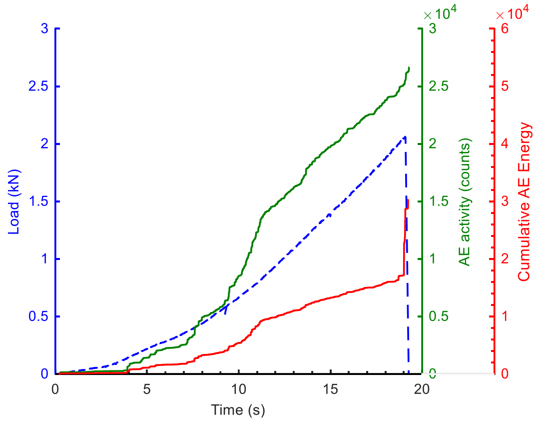

(d)

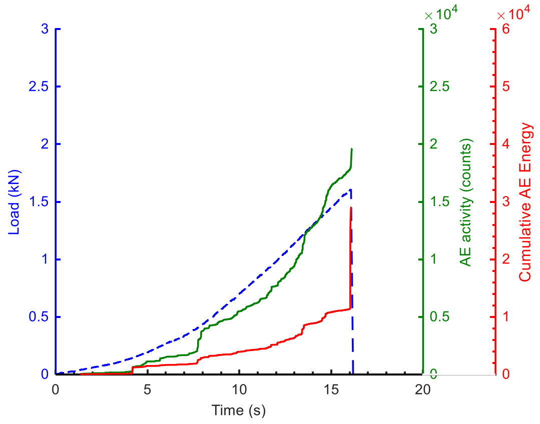

(e)

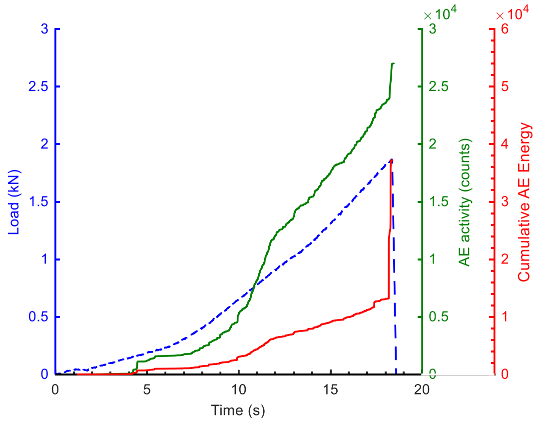

(f)

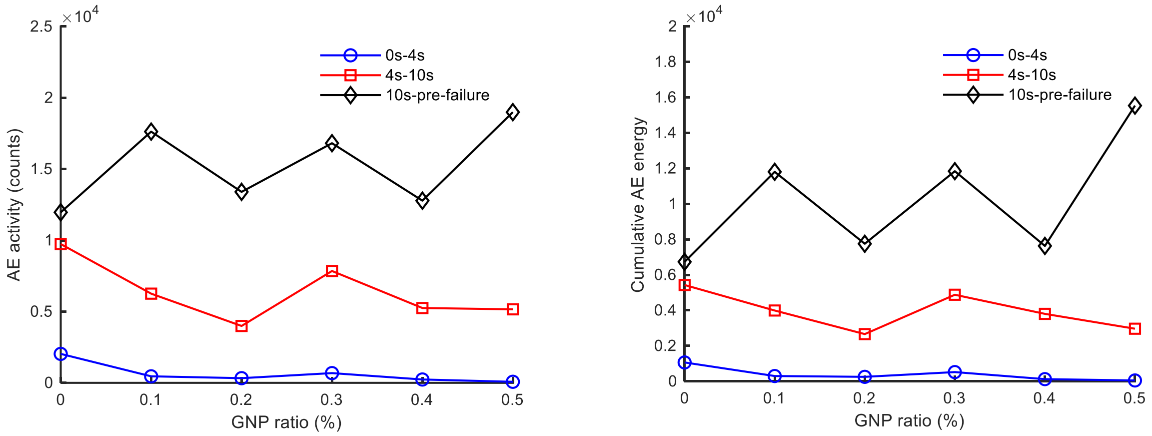

(g) (h)

**Figure 4-5.** Tensile load, AE counts, and cumulative AE energy versus time: (a) control specimen, and specimens reinforced with GNPs at (b) 0.1 wt.%, (c) 0.2 wt.%, (d) 0.3 wt.%, (e) 0.4 wt.% and (f) 0.5 wt.%; and the change in acoustic emissions (g) counts and (h) energy per loading stage.

The average acoustic energy is calculated as the total AE energy divided by total AE hits. Figure 4-6 illustrates the AE activity and average AE energy during the complete loading period and the pre-failure period. In general, the number of cumulative AE activities (i.e. counts) of specimens reinforced with GNPs is higher than the control specimens at failure. However, specimens reinforced with 0.2 wt.% and 0.4 wt.% GNP had a lower number of cumulative AE activities at failure. This might be due to the non-uniform dispersion and agglomerations of GNPs. During the pre-failure, the AE activities of specimens reinforced with GNPs are less than or similar to those in the control specimen. This indicates that the addition of GNPs can impede the formation of cracks. The average energy of GNPs-reinforced specimens is clearly higher than that of the control specimen all cases. However, the average energy of all specimens in pre-failure period are similar, revealing that the major difference appears during failure period. This indicates that specimens with GNP reinforcement release more energy by breaking or pulling out GNPs. Furthermore, the trend of average AE energy during the failure period is consistent with the trend of tensile strength.

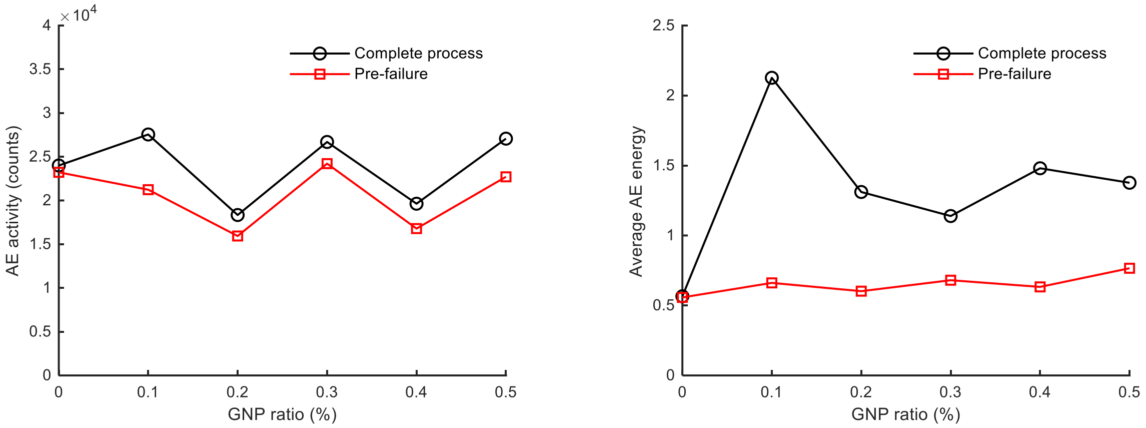

(a) (b)

**Figure 4-6.** (a) Acoustic emission counts and (b) average AE energy for control specimen and specimens reinforced with GNPs for the complete loading duration, and for the last second pre-failure.

Cracks can be classified into tensile and shear cracks by analyzing the correlation between average frequency (AF) and RA values, defined as the ratio of rise time over amplitude. Tensile cracks appear with high AF and low RA values, while shear cracks have large RA value and low AF. However, the criterion of the proportion of AF and RA value have not been defined, which makes it difficult to classify cracks. In this research, the Gaussian mixture modeling (GMM) is employed to classify AE data into the two main clusters, considering data distribution properties [154]. The results of all specimens are presented in Figure 4-7. The yellow regions represent high probability density and the blue regions have a small probability density. It is obvious that in all specimens, the dominant cracking mode is the tensile mode. However, the probability of the occurrence of shear cracks increases slightly with the increase of GNP reinforcement ratio. This indicates that addition of GNPs increases the shear failure on the GNP-matrix interface. Furthermore, the addition of GNPs enforces the occurrence of cracks in a region of RA with a value less than 1 ms/dB compared to 2 ms/dB for control specimens.

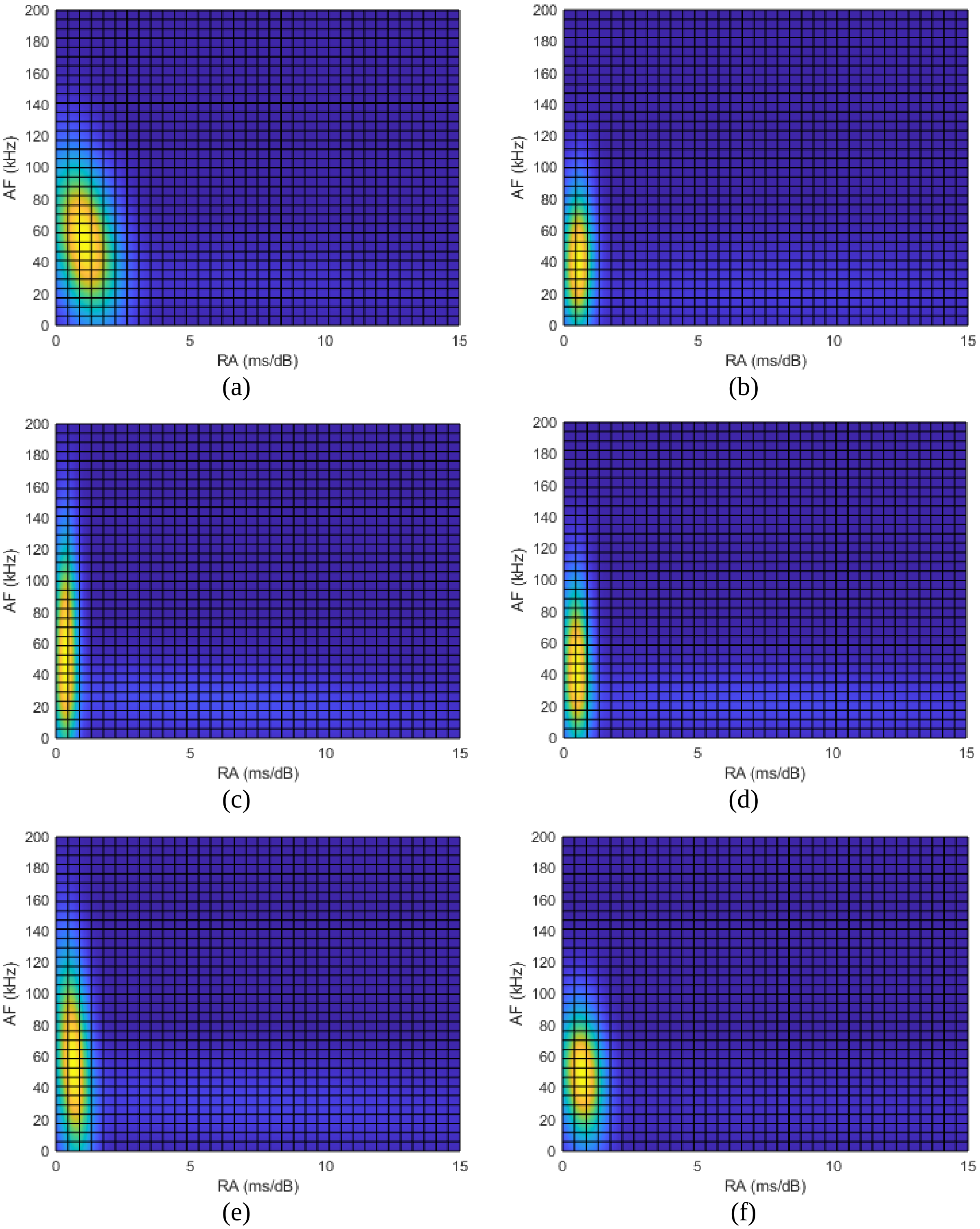

(a) (b) (c) (d) (e) (f)

**Figure 4-7.** Gaussian mixture modeling (GMM) of feature vectors for cementitious composites: (a) control specimen, and specimens reinforced with GNPs at (b) 0.1 wt.%, (c) 0.2 wt.%, (d) 0.3 wt.%, (e) 0.4 wt.% and (f) 0.5 wt.%.

The average RA value are calculated and presented in Figure 4-8. It can be seen that the average RA value of the specimens with GNP reinforcement is considerably higher than that of the control specimen. Higher RA indicates the shear fracture occurs on the matrix-GNPs interface, thus enhancing the tensile behavior with the high interfacial bond strength of GNPs [155,156]. This result is consistent with the increasing probability of the occurrence of shear cracks in specimens with GNPs reinforcement.

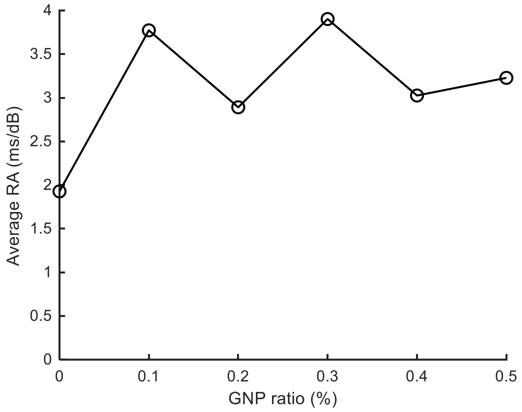

**Figure 4-8.** Variation of the average RA value for cementitious composites with GNP content ranging from 0% to 0.5%.

### *4.7.2. Ib-value Analysis*

The Ib-value is calculated from the amplitude distribution of the 100 consecutive signals and is illustrated in Figure 4-9 for all cementitious composite specimens. Different types of acoustic emission signals with variable frequency and amplitude are generated by different fracture modes. The appearance of microcracks at the early stage is usually accompanied with plenty of AE signals with small amplitude, while the high amplitude AE signal would arise with macrocracks. According to Equation 4-4, the group with highest amplitude, which would usually occur at the maximum force, will have relatively lower Ib-value. Instead, the microcracks generated at early stages will lead to higher Ib-value. There is a clear and abrupt drop of the Ib-value drop at the maximum force, except for control specimens. GNP reinforced specimens have significantly higher amplitude AE signal at the maximum force. The control specimen had three relatively high amplitude appearing around 10s, indicating the occurrence of macrocracks without causing failure. However, the Ib-value analysis did not distinguish the difference between different mixtures, indicating that Ib-value analysis might not be as necessary as other AE parameter analysis in tensile behavior of cementitious composite.

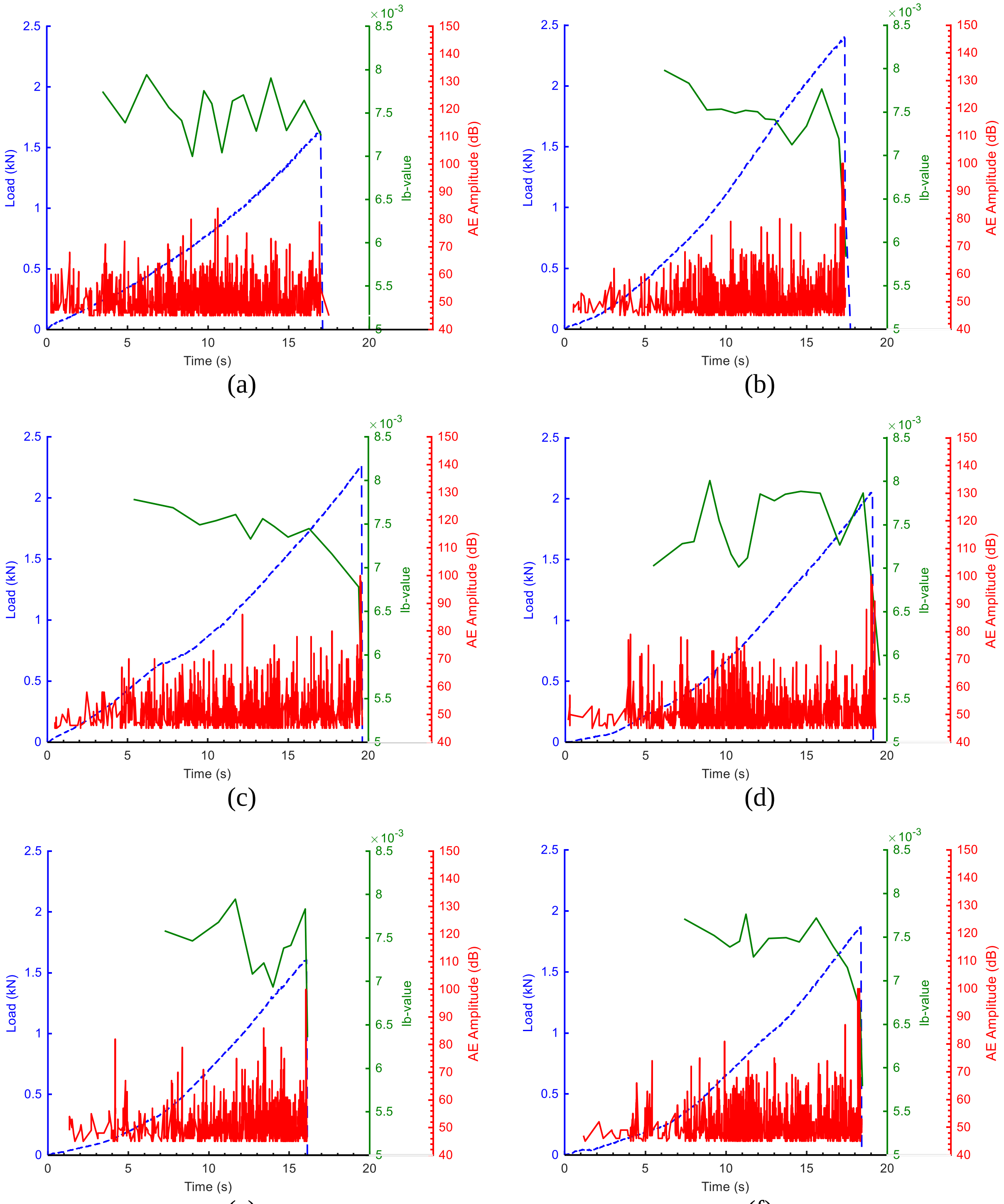

(a) (b)

(c) (d)

(e) (f)

**Figure 4-9.** Interaction of load, acoustic emissions amplitude and Ib-value for cementitious composites: (a) control specimen, and specimens reinforced with GNPs at (b) 0.1 wt.%, (c) 0.2 wt.%, (d) 0.3 wt.%, (e) 0.4 wt.% and (f) 0.5 wt.%.

### *4.7.3. Crack Location Analysis*

AEwin$^{TM}$ software analyzes AE hit data to mathematically calculate the location of all AE events. Figures 4-10(a) and 4-10(b) present the AE counts along the specimen length, and a photo of a cementitious composite with 0.5 wt.% GNP. The acoustic emissions data indicates that most cracks occur at a position of 142.24 in. This is similar to the failure position shown in Figure 4-9(b). Due to using an estimated wave velocity value based on mortar, the localization of acoustic emissions is approximate. It should be noted that GNPs might change the wave velocity of cementitious composites. Therefore, it is necessary to calibrate the acoustic parameters for each reinforcement ratio of cementitious composites. Furthermore, only linear crack position can be determined due to the use of two acoustic sensors. Thus, it is recommended in future work to utilize larger number of sensors to enable 3D crack localization.

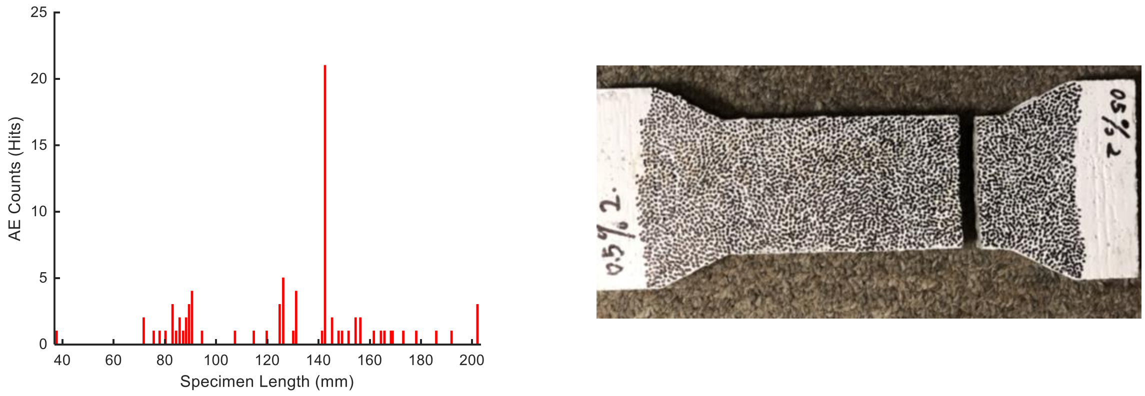

(a) (b)

**Figure 4-10.** (a) Acoustic emission counts across the linear length and (b) image of the failure position for a cementitious composite reinforced with 0.5 wt.% GNP.

## 4. 8. Summary

In this chapter, the tensile performance of GNP-reinforced cementitious composite with reinforcement ratios from 0% to 0.5 wt.% was investigated. Acoustic emission was used to monitor the behavior of GNP-reinforced cementitious composites and to characterize and localize the cracks as they are initiated. Based on the findings, the following conclusions can be made:

- The addition of GNPs increased the tensile strength of cementitious composite. With the addition of GNPs at a concentration level of 0.1 wt.%, the maximum increase in tensile strength (48%) was achieved compared to plain mortar.
- The addition of GNPs can improve the tensile behavior of cementitious composite by crack bridging to impede crack propagation at initial stages, and absorb energy by deforming to slow cracks, while at failure the GNPs are pulled-out.
- The addition of GNPs resulted in a higher cumulative acoustic energy that correlates to the increased tensile force required to initiate and propagate cracks.
- Average AE energy (i.e. total AE energy/ total AE activity) of GNPs reinforced specimens was higher than that of the control specimen in complete process and similar with the one of the control specimen during pre-failure, indicating more energy released by breaking or pulling out GNPs.
- Average RA value of cementitious material was increased with GNPs reinforcement, which indicates the shear fracture on the GNPs-matrix interface, thus improving the tensile behavior.
- The location of cracks initiated, and propagating can be identified through analyzing the travel time of the acoustic emissions.

Further studies are needed to enhance the localization of cracks by calibrating the travel speed of acoustic emissions for each reinforcement ratio and by using multiple sensors to pinpoint the location of a crack in a three-dimensional domain. A detailed understanding of the effects of GNPs into cementitious microstructure was out of the scope of current study, but it needs to be assessed in future studies.

# 5. OPTIMAL DISPERSION PROCESS PARAMETERS FOR FABRICATION OF GRAPHENE-CEMENT COMPOSITES

## 5. 1. Overview

This chapter explores the optimal disperson process for incorporating graphene nanoplatelets (GNPs) into cement-based composites. Surfactant-assisted sonication is used as the dispersion method. The effects of six factors (sonication time, sonication amplitude, sample volume, surfactant type, surfactant/GNP ratio, and GNP concentration) with five control levels are studied on the dispersion performance. As for surfactant type, two ionic surfactants, one non-ionic surfactant, and two polycarboxylate superplasticizers are considered. Taguchi method of experimental design is employed to minimize the number of experiments needed to assess the effects of selected factors on the dispersion process. An orthogonal array of L25 is used for the experimental design and the dynamic light scattering and UV-vis spectroscopy tests are conducted to characterize the dispersion and stabilit of GNPs. The average particle size, UV-vis absorbancy in aqueous and alkaline environments, zeta potential in aqueous and alkaline environments, residual absorbance after 24 h in aqueous and alkaline environments are seclected as performance criteria. Two multi-criteria decision making methods, namely Technique for Order Preference by Similarity to an Ideal Solution (TOPSIS) and Principle Component Analysis (PCA) methods, are then employed to determine the optimal values of experimental factors. The additional experiments are conducted to refine the findings from the Taguchi-based optimization study and then optimal parametes for each factor are identified.

## 5. 2. Materials and Sample Preparation

### *5.2.1. Materials*

GNP Grade C-300 manufactured by XG Science through mechanical exfoliation is used in this study. Table 5-1 shows various properties of the C-300 GNPs.

**Table 5-1.** Properties of GNP C-300

| **Properties** | **Values** |
|---|---|
| Surface Area ($m^2/g$) | 300 |
| Diameter (μm) | <2 |
| Thickness (nm) | 1-2 |
| Density (g/cc) | 0.2-0.4 |
| Carbon Content (%) | >99.5 |

Five different dispersion agents were considered in this study: two commercially available polycarboxylate-based superplasticizers (named as PCE-1 and PCE-2), sodium doecylbenzene sulfonate (SDBS), sodium cholate (SC), and Pluronic F-127 (F127). Polycarboxylate-based superplasticizer (PCE) consisits of a main carbon chain with carboxylate groups and poly-ethylene oxide side chains. Since PCE contains both anionic and non-ionic components and is already used in concrete industry, it has been commonly used to disperse carbon-based nanomaterials in cementitious composites. The structures of the SDBS, SC, and F-127 are illustrated in Figure 5-1. SDBS is one of the most popularly used surfactant for the dispersion of nanomaterials in aqueous solutions [157]. It is an anionic surfactant, comprising a hydrophilic sulfonate head-group and a hydrophobic alkylbenzene tail-group. Several studies found the SDBS to be very effective for the dispersion of graphene in cement composites[31,88]. Pluronic F-127 has previously been used as an effective steric stabilizer for nonionic aqueous dispersions of graphene in cement composites [158]. Sodium cholate is an anionic bio-surfactant and was considered for the dispersion of graphene in concrete and found to be effective [121].

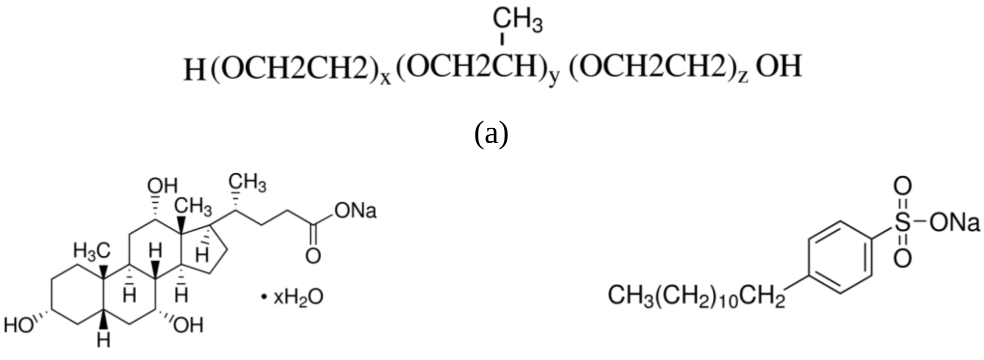

$$H(OCH2CH2)_x(OCH2\overset{CH_3}{CH})_y(OCH2CH2)_z OH$$

(a)

(b) (c)

**Figure 5-1.** Molecular structure of select surfactants: (a) Pluronic F127; (b) Sodium Cholate; and (c) SDBS.

When GNPs are added into the cementitious materials, they are dispersed in a strong alkaline environment, which might influence their dispersion quality. Hence, the dispersion quality of GNPs in high alkaline environment was assessed through the addition of GNP suspensions into a simulated cement pore solution (CPS) and then conducting the relevant characterization tests. For the UV-vis spectroscopy tests, the chemicals given in Table 5-2 are used at given concentration levels to create a simulated cement pore solution. To this end, the powders of $Ca(OH)_2$ and $CaSO_4{\cdot}2H_2O$ as well as the NaOH and KOH pellets were added into a beaker with deionized water. The solutions were stirred with a magnetic mixer for 5 min at 1000 rpm and then filter twice to obtain the clear solution. For the zeta potential measurements, a saturated $Ca(OH)_2$ solution is prepared in a similar way and used as alkaline environment.

**Table 5-2.** Concentration of added chemicals in CPS [48]

| **Compounds** | **Concentration (g/L)** |
|---|---|
| NaOH | 8 |
| KOH | 22.4 |
| $CaSO_4{\cdot}2H_2O$ | 27.6 |
| $Ca(OH)_2$ | Saturated |

### *5.2.2. Preparation of GNP Suspension*

The GNP suspension was prepared by blending select amounts of water, GNPs, and surfactants. The liquid (PCEs) or powder (SC, SDBS, F127) surfactants were mixed with water first and the GNPs were added then and stirred gently. To obtain a homogenous dispersion of GNPs, the ultrasonication was carried out using a probe sonicator (Cole-Parmer-750). Six factors with five control levels are explored their effects on disperison quality of GNPs as shown in Table 5-3. The sonication amplitude was varied from 20% to 100%, while the sonication duration was varied from 15 min to 120 min. The volume of the water for the suspensions was another factor and changed from 30 mL to 200 mL. Five surfactants described earlier were used to disperse GNPs at surfactant-to-GNP ratios from 0.5 to 2.5. The GNP concentration in the suspensions was varied from 1 g/L to 10 g/L.

**Table 5-3.** Factors and levels

| **Factors** | **Definition** | **Levels** | | | | |
|---|---|---|---|---|---|---|
| | | **1** | **2** | **3** | **4** | **5** |
| F1 | Sonication amplitude (%) | 20 | 40 | 60 | 80 | 100 |
| F2 | Sonication time (min) | 15 | 30 | 60 | 90 | 120 |
| F3 | Sample volume (mL) | 30 | 50 | 100 | 150 | 200 |
| F4 | Surfactant type | PCE-1 | PCE-2 | SC | SDBS | F127 |
| F5 | Surfactant/GNP ratio | 0.5 | 1 | 1.5 | 2 | 2.5 |
| F6 | GNP concentration (g/L) | 1 | 2 | 5 | 7.5 | 10 |

As there are relatively large number of factors and levels for each factor, the design of experiments via Taguchi method was considered in this study. The Taguchi method is an experimental design technique that helps understanding how different parameters affect the mean and variance of a process. It considerably reduces the required number of experiments by using orthogonal arrays. Here, an $L_{25}$ orthogonal array with six columns and 25 rows was used to design 25 experiments to assess the effects of six factors on the dispersion and stability of GNP suspensions. The specific design is shown in Table 5-4.

Table 5-4. $L_{25}$ Taguchi design for GNP dispersion

| Exp. No. | Factors | | | | | |
|---|---|---|---|---|---|---|
| | **F1** | **F2** | **F3** | **F4** | **F5** | **F6** |
| 1 | 20 | 15 | 30 | PCE-1 | 0.5 | 1 |
| 2 | 20 | 30 | 50 | PCE-2 | 1 | 2 |
| 3 | 20 | 60 | 100 | SC | 1.5 | 5 |
| 4 | 20 | 90 | 150 | SDBS | 2 | 7.5 |
| 5 | 20 | 120 | 200 | F127 | 2.5 | 10 |
| 6 | 40 | 15 | 50 | SC | 2 | 10 |
| 7 | 40 | 30 | 100 | SDBS | 2.5 | 1 |
| 8 | 40 | 60 | 150 | F127 | 0.5 | 2 |
| 9 | 40 | 90 | 200 | PCE-1 | 1 | 5 |
| 10 | 40 | 120 | 30 | PCE-2 | 1.5 | 7.5 |
| 11 | 60 | 15 | 100 | F127 | 1 | 7.5 |
| 12 | 60 | 30 | 150 | PCE-1 | 1.5 | 10 |
| 13 | 60 | 60 | 200 | PCE-2 | 2 | 1 |
| 14 | 60 | 90 | 30 | SC | 2.5 | 2 |
| 15 | 60 | 120 | 50 | SDBS | 0.5 | 5 |
| 16 | 80 | 15 | 150 | PCE-2 | 2.5 | 5 |
| 17 | 80 | 30 | 200 | SC | 0.5 | 7.5 |
| 18 | 80 | 60 | 30 | SDBS | 1 | 10 |
| 19 | 80 | 90 | 50 | F127 | 1.5 | 1 |
| 20 | 80 | 120 | 100 | PCE-1 | 2 | 2 |
| 21 | 100 | 15 | 200 | SDBS | 1.5 | 2 |
| 22 | 100 | 30 | 30 | F127 | 2 | 5 |
| 23 | 100 | 60 | 50 | PCE-1 | 2.5 | 7.5 |
| 24 | 100 | 90 | 100 | PCE-2 | 0.5 | 10 |
| 25 | 100 | 120 | 150 | SC | 1 | 1 |

## 5. 3. Characterization of GNP Dispersion

### *5.3.1. Size and Zeta Potential Measurements Using Dynamic Light Scattering*

Hydrodynamic size distribution and zeta potentials measurements were conducted using a ZetaNano ZS90 (Malvern Instruments). The size detection was carried out at a scattering angle of 90°. The viscosity value of water was used in all measurements. Prior to the measurements, 1 mL sample was equilibrated to 25 °C for 120s. The zeta potentials were calculated from the mobilities using the Smoluchowski model [91]. For each sample, three measurements were performed with an automatic measurement duration setting. The mean value of three measurements is reported. The zeta potential measurements were carried out for the dispersion of GNPs in both aqueous and alkaline environments.

### *5.3.2. UV-vis Spectroscopy*

UV-vis spectroscopy is an efficient, rapid, and quantitative method to assess the dispersion and stability of nanoparticles in aqueous suspensions [159]. In the UV-vis spectroscopy, the light absorbed by the nanofluid, which is proportional to the concentration of nanoparticles, is measured within the visible wavelength range. The higher absorbency refers to an increase in nanoparticles, i.e., better dispersion of GNPs. Here, the absorbance of GNP suspensions was measured using a Shimadzu UVmini-1240 spectrophotometer. The peak absorbance observed a wavelength of 260 nm was recorded for each suspension. The absorbance measurements were taken from dispersion of GNPs in both aqueous and alkaline environments immediately after sonication. The measurements were also carried out 24 hours later to evaluate the stability.

## 5. 4. Analysis Methods

### *5.4.1. Dispersion Performance Criteria*

To assess the dispersion and stability of GNPs, seven performance characteristics are selected as shown in Table 5-5. These characteristics include average particle size, the absolute value of zeta potential, UV-vis absorbency in aqueous and alkaline environments, the absolute value of zeta potential in alkaline environment, the residual absorbance after 24 h in aqueous and alkaline environments. Residual absorbance is calculated as the ratio of the absorbance value measured immediately after dispersion to that of measured after 24 h. For the particle size, a smaller value indicates better response while for all the other performance characteristics a larger value implies better dispersion and/or stability.

**Table 5-5.** Quality criteria and weights

| **Quality Criteria** | **Definition** | **Target values** | **Weights** |
|---|---|---|---|
| R1 | Average particle size | Smaller is better | 1 |
| R2 | Absolute value of zeta potential | Larger is better | 1 |
| R3 | Absorbency in water | Larger is better | 1 |
| R4 | Absorbency in alkaline environment | Larger is better | 1 |
| R5 | Residual absorbance after 24 h in water | Larger is better | 1 |
| R6 | Absolute value of zeta potential in alkaline environment | Larger is better | 1 |
| R7 | Residual absorbance after 24 h in alkaline environment | Larger is better | 1 |

### *5.4.2. Analysis Methods*

The performance for Taguchi method is measured by signal-to-noise (S/N) ratio, which is calculated based on selected performance characteristics for the experiments. The S/N ratios is mostly defined either as the smaller-the-better or the larger-the-better responses, and can be are calculated by Eq. 1 and Eq. 2 [160,161] as follows:

$$\eta_{ij} = -10log_{10}[\frac{1}{n}\sum_{k=1}^{n} y_{ijk}^2] \qquad 5\text{-}1$$

$$\eta_{ij} = -10log_{10}[\frac{1}{n}\sum_{k=1}^{n} \frac{1}{y_{ijk}^2}] \qquad 5\text{-}2$$

where $\eta_{ij}$ is the S/N ratio for the response *j* for the experiment i, $y_{ijk}^2$ is the experiment result for the response *j* of the experiment *i*, in the *k*th replication; *n* is the total number of replications.

Typically, a multi-criteria decision making method is used with Taguchi method to to convert the multi-response problem into a one-response prolem [162–164]. Here, two such methods, Technique for Order Preference by Similarity to an Ideal Solution (TOPSIS) and Principle Component Analysis (PCA) methods were combined with the Taguchi method to determine the optimal values of experimental factors. The TOPSIS method is a simple method used for solving decision making problems [165]. It is easy to perform compared with other multi-response simulation optimization methods. The method aims to find the alternative that has the shortest Euclidean distance from the postive ideal solution and the farthest from the negative ideal solution. The TOPSIS method involves the following steps:

Step 1: Determine the decision matrix:

The decision matrix contains the S/N ratios

$$D = \begin{bmatrix} \eta_{11} & \eta_{12} & \cdots & \eta_{1k} \\ \eta_{21} & \eta_{22} & \cdots & \eta_{2k} \\ \cdots & \cdots & \cdots & \cdots \\ \eta_{m1} & \eta_{m2} & \cdots & \eta_{mk} \end{bmatrix} \tag{5-3}$$

Step 2: Normalization

$$r_{ij} = -\frac{\eta_{ij}}{\sqrt{\sum_{i=1}^{m} \eta_{ij}{}^{2}}} \tag{5-4}$$

i = 1,…, m and j = 1,…, k.

Step 3: Determine the weighted normalized decision matrix

$$V = \left[v_{ij}\right]_{m\times k}, \qquad \mathrm{i} = 1, \dots, \mathrm{m \ and \ j} = 1, \dots, \mathrm{k} \tag{5-5}$$

$$v_{ij} = w_j r_{ij}, \qquad \mathrm{i} = 1, \dots, \mathrm{m \ and \ j} = 1, \dots, \mathrm{k} \tag{5-6}$$

$w_j$ is the weight of resposne j and $\sum_{j=1}^{k} w_j = 1.$

Step 4: Positive ideal and negative ideal solutions (A* and $A^-$)

The positive ideal solution is made of all the maximum S/N ratio, while the negative ideal solution is made of all the minimum S/N ratio at the responses in the weighted normalized desicion matrix.

$$A^* = [v_j^*]_k \tag{5-7}$$

$$A^- = [v_j^-]_k \tag{5-8}$$

and,

$$v_j^* = v_{j,max}$$

$$v_j^- = v_{j,min}$$

<u>Step 5:</u> Calculate the separation mesures

The distance of experiment i to the positive ideal solution is calculated as:

$$S_i^* = \sqrt{\sum_{j=1}^{k} (v_{ij} - v_j^*)^2} \tag{5-9}$$

The distance of experiment i to the negative ideal solution is calculated as:

$$S_i^- = \sqrt{\sum_{j=1}^{k} (v_{ij} - v_j^-)^2} \tag{5-10}$$

<u>Step 6:</u> Calculate the ranking score $C_i^*$

$$C_i^* = \frac{S_i^-}{S_i^- + S_i^*} \tag{5-11}$$

A larger ranking score indicates better performance of the alternatives.

Note that many multicriteria decision making methods, including TOPSIS, assumes the response variable or evaluation criteria is statically independent, which may not be the case in real problem. PCA can be used to overcome this shortcoming as it can identify patterns in the correlated data and then eliminates the dependencies without much loss of information [166].The PCA method is presented below:

Step 1: Determine the decision matrix:

The decision matrix contains the S/N ratios

$$D = \begin{bmatrix} \eta_{11} & \eta_{12} & \cdots & \eta_{1k} \\ \eta_{21} & \eta_{22} & \cdots & \eta_{2k} \\ \cdots & \cdots & \cdots & \cdots \\ \eta_{m1} & \eta_{m2} & \cdots & \eta_{mk} \end{bmatrix}$$

Step 2: Normalize the decision matrix

$$N_{ij} = \frac{\eta_{ij} - \eta_{i,min}}{\eta_{i,max} - \eta_{i,min}} \tag{5-12}$$

Step 3: Calculate the covariance matrix

$$C_{pq} = \frac{Cov(N_{ip}, N_{iq})}{\sqrt{Var(N_{ip})Var(N_{iq})}} \tag{5-13}$$

p,q = 1,..., k.

Step 4: Calculate the eigenvalues and eigenvectors

The eigencalues and eigenvectors are calculated by the following equation:

$$(\boldsymbol{C} - \lambda \boldsymbol{E})\boldsymbol{V} = 0 \tag{5-14}$$

where $\lambda$ refers to the eigenvalues and [V] refers to the eigenvectors.

The jth eigenvector is formulated as:

$$V_j = \begin{bmatrix} a_{1j} \\ a_{2j} \\ \vdots \\ a_{kj} \end{bmatrix}$$

Step 5: Calculate the principal components

The jth principal components is formulated as:

$$P_j = \sum_{l=1}^{k} a_{lj} \times N_l \tag{5-15}$$

Step 6: Calculate the composite principal components

$$P = \sum_{m=1}^{k} \psi_m \times P_m \tag{5-16}$$

## 5. 5. Results and Discussion

### *5.5.1. Main Effects Plots*

The experimental tests on the dispersion quality were conducted based on L25 Taguchi design considering six factors. The seven performance criteria described in Table 5-6 was evaluated for each of 25 experiments and the results are provided in Table 5-6.

**Table 5-6.** $L_{25}$ experimental results

| Exp. No. | R1 (nm) | R2 (mV) | R3 (a.u.) | R4 (a.u.) | R5 | R6 (mV) | R7 |
|---|---|---|---|---|---|---|---|
| 1 | 470.1 | -16.77 | 0.315 | 0.267 | 0.6367 | -2.92 | 0.3109 |
| 2 | 444.6 | -19.23 | 0.273 | 0.203 | 0.7216 | -3.47 | 0.3350 |
| 3 | 387.1 | -43.27 | 0.255 | 0.205 | 0.8498 | -7.78 | 0.1659 |
| 4 | 421.7 | -33.47 | 0.274 | 0.447 | 0.7770 | -15.73 | 0.1365 |
| 5 | 411.5 | -13.03 | 0.235 | 0.188 | 0.6468 | -0.37 | 0.3723 |
| 6 | 380.1 | -27.53 | 0.330 | 0.229 | 0.7217 | -9.98 | 0.2489 |
| 7 | 398.5 | -27.90 | 0.452 | 0.557 | 0.7140 | -14.97 | 0.0880 |
| 8 | 428.2 | -13.03 | 0.378 | 0.324 | 0.7540 | -0.34 | 0.6481 |
| 9 | 395.6 | -15.73 | 0.355 | 0.289 | 0.7653 | -2.17 | 0.6125 |
| 10 | 386.2 | -19.37 | 1.013 | 0.867 | 0.8147 | -3.56 | 0.0369 |
| 11 | 451.9 | -12.83 | 0.382 | 0.341 | 0.7670 | -0.62 | 0.5337 |
| 12 | 428.0 | -17.53 | 0.387 | 0.352 | 0.6925 | -1.94 | 0.6307 |
| 13 | 408.9 | -16.43 | 0.482 | 0.479 | 0.7455 | -3.71 | 0.1148 |
| 14 | 387.7 | -29.63 | 1.531 | 1.109 | 0.8922 | -8.14 | 0.0009 |
| 15 | 363.3 | -21.63 | 1.269 | 1.024 | 0.8458 | -10.77 | 0.0205 |
| 16 | 401.7 | -19.50 | 0.355 | 0.258 | 0.6732 | -3.49 | 0.2946 |
| 17 | 428.6 | -21.10 | 0.495 | 0.389 | 0.6606 | -8.27 | 0.0026 |
| 18 | 404.2 | -22.70 | 1.218 | 0.815 | 0.8571 | -7.07 | 0.0012 |
| 19 | 375.1 | -13.17 | 1.755 | 1.727 | 0.8991 | -0.71 | 0.7481 |
| 20 | 411.2 | -18.20 | 1.147 | 0.967 | 0.7942 | -2.83 | 0.2420 |
| 21 | 420.8 | -29.97 | 0.459 | 0.401 | 0.7370 | -8.87 | 0.0474 |
| 22 | 405.3 | -12.93 | 0.983 | 0.889 | 0.8494 | -0.71 | 0.7885 |

| | | | | | | | |
|---|---|---|---|---|---|---|---|
| 23 | 407.8 | -18.73 | 1.135 | 0.976 | 0.8194 | -2.21 | 0.5123 |
| 24 | 418.8 | -17.50 | 0.956 | 0.830 | 0.7626 | -4.19 | 0.0181 |
| 25 | 373.8 | -23.40 | 1.317 | 1.220 | 0.8130 | -8.29 | 0.0385 |

The main effects plots provide an understanding on the optimal combination of dispersion process parameters for the desired dispersion performance such as smaller particle size or high absorbency value. These plots also indicates the relative significance of the process parameters on the dispersion quality. If the main effects plots remain almost horizontal for a particular parameter then the parameter has little effect on the dispersion quality. On the other hand, if the main effects plots possess high inclination then this indicates significant effect of this particular parameter on the dispersion performance. Figure 5-2 presents the main effects plot for the average particle size of GNPs after being dispersed in water using different surfactants and dispersion parameters. The particle size has a decrease when the sonication amplitude is increased from 20% to 40% and then almost becomes stable, indicating that further increase of sonication amplitude does not have significant effect on particle size. However, the particle size of GNPs consistently decreases with the increasing of sonication time. The sample volume also does not affect the particle size considerably. Among different surfactants, the SC provides the smallest particle size, followed by the SDBS. Increasing surfactant ratio somewhat decreases the particle size, while the an increase in the GNP ratio did not produce a clear trend on the particle size.

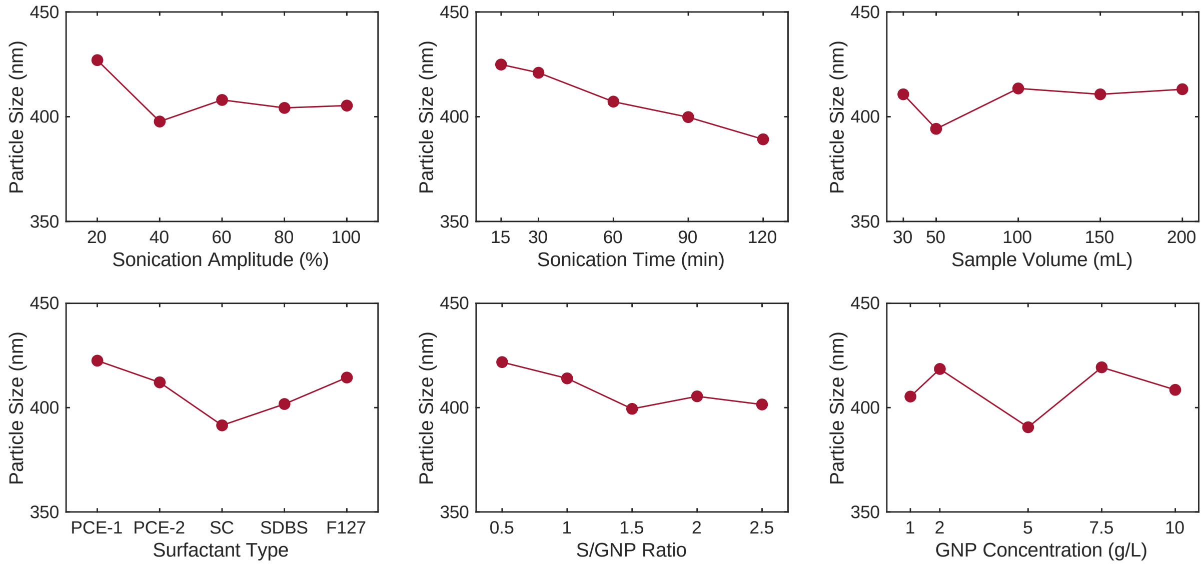

**Figure 5-2.** Main effects plot for average particle size of GNPs

The main effects results for absorbency values are presented in Figure 5-3. Note that the results for the dispersion performance of the GNPs both in water and alkaline environment are provided in the figure. The absorbance values considerably increase with either increasing sonication amplitude up to 80% amplitude or sonication duration up to 90 min, indicating improvement in degree of dispersion with increasing sonication power. Further increasing these values to 100% amplitude and 120 min, respectively does not affect the absorbance. On the other hand, using larger sample volume while keeping the same sonication power results in a decrease in the absorbency. The mean effects plots with surfactant type, surfactant ratio and GNP concentration do not present much variation and remains mostly horizontal, indicating similar dispersion performance when these factors are varied. In addition, when the dispersed GNPs are added to simulated cement pore solution, there is a slight decrease in absorbance values for all cases, however, the general trend of the plots remains very similar to those obtained for the dispersion of GNPs in water. The decrease in the absorbance value in alkaline environment indicates potential agglomeration of GNPs.

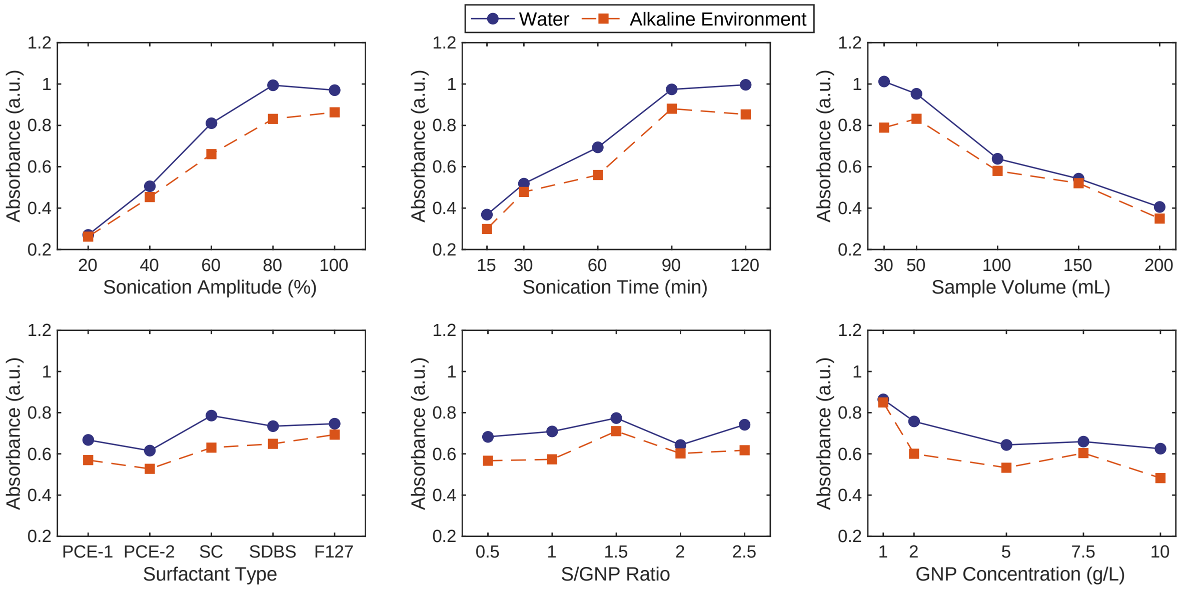

**Figure 5-3.** Main effects plot for UV-vis absorbance

To assess the stability of the GNP dispersions, the main effects plots for the zeta potential and residual absorbency values were created. Figure 5-4 shows the main effects plot for zeta potential in aqueous and alkaline media, while the main effects plots for residual absorbency are provided in Figure 5-5. The stability of colloidal suspensions is commonly assessed by their zeta potential ($\zeta$), which measures the electrostatic repulsion between nanoparticles [56,167]. Five surfactants considered in this study can be divided into three groups: ionic surfactants (SC and SDBS), non-ionic surfactants (F127), and two polycarboxylate superplasticizers (PCE-1 and PCE-2). Thus, the stabilization mechanisms are different because of their different structures. For ionic surfactants, the dispersed particles will be stabilized mainly by the electrostatic repulsion between electric double layer and the mechanism is described by the Derjaguin-Landau-Verwey-Overbeek (DLVO) theory [168]. The ion tail group of ionic surfactants absorb onto GNP particles by van der Waals interactions, forming the inner layer. The head groups will disassociate and introduce an effective charge on the particles, which is the outer layer. A repulsive pressure will be generated between like-charged dispersed particles when two layers overlap. The potential at a region outside the inner layer is named as zeta potential and helps to quantify the stability of charged dispersions [87,169]. In other words, a higher magnitude ($|\zeta|$) for zeta potential indicates more absorbed ions, higher electrostatic repulsion, and better stability.

Colloidal particles with |ζ| > 30 mV are expected to have moderate stability with no agglomeration [170].

On the other hand, in non-ionic surfactants, hydrophobic tail groups absorb onto GNP particles, while the long hydrophilic groups of the molecule spread into media. When two particles overlap, the hydrophilic groups interact, leading to a steric hindrance and preventing the agglomerations of particles [87,171]. Both the steric hindrance and the electrostatic repulsion exist in polycarboxylate superplasticizer. However, their stabilization mechanism is dominant by the steric hindrance [56,68]. These different stabilization mechanisms need to be considered while evaluating the zeta potential measurements.

As mentioned above, a high absorbance value is proportional to the concentration of GNP particles and indicates better dispersion. Therefore, a reduction in absorbance can directly imply the deterioration of the dispersion. As a result, for the residual absorbance values, a value closer to one indicates better dispersion stability.

When the main effects plots for zeta potential and residual absorbency shown in Figures 5-4 and 5-5 are evaluated, it can be seen that the surfactant type produce plots with higher inclinations compared to all other parameters. The samples with ionic surfactants (SC and SDBS) have |ζ| close to 30 mV in aqueous suspension, which is considerably higher than the |ζ| value obtained for other surfactants. As steric hinderance is dominant in the dispersion of polycarboxylate superplasticizers and non-ionic surfactant (F127), zeta potential is not precise to describe the dispersion stability. The coating of polycarboxylate superplasticizer and non-ionic surfactant might mask the negative surfaces charges of GNP particles, resulting in decreased |ζ| value [172]. Also, an increase in pH value decreases the zeta potential values for all surfactants, indicating less stability in alkaline environment.

Residual absorbance values in aqueous solution with all the surfactants attains a similar value around 0.8. However, in alkaline environment, the absorbance value decreases below 0.2 for the dispersions with SC, SDBS, and PCE-2, while it is 0.42 and 0.6 for PCE-1 and F127.

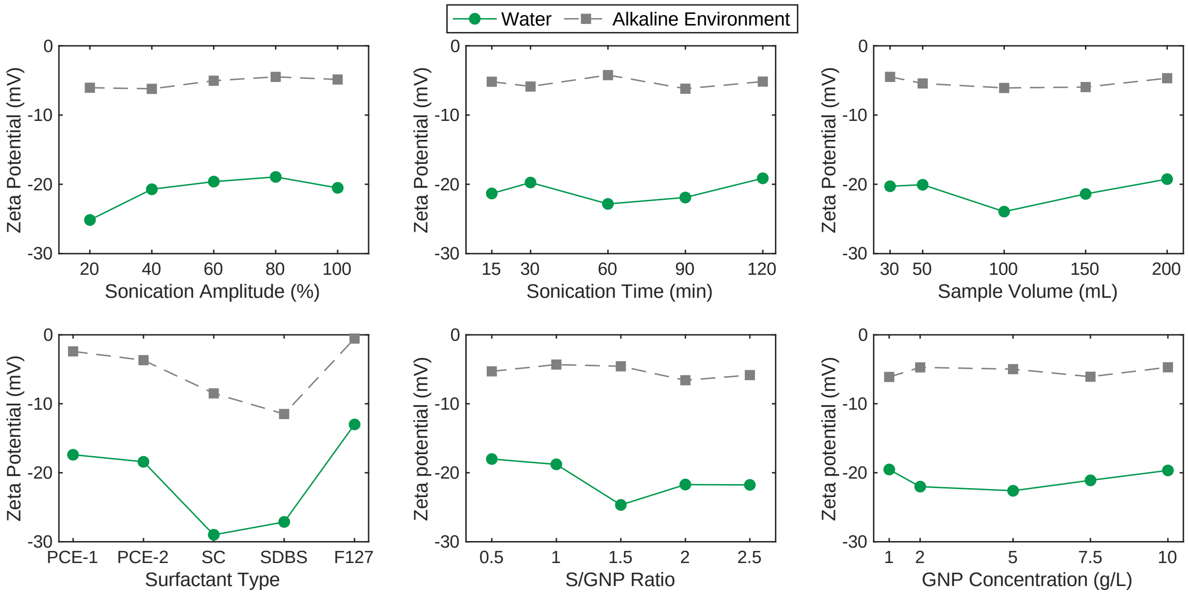

**Figure 5-4.** Main effects plot for zeta potential in aqueous and alkaline media

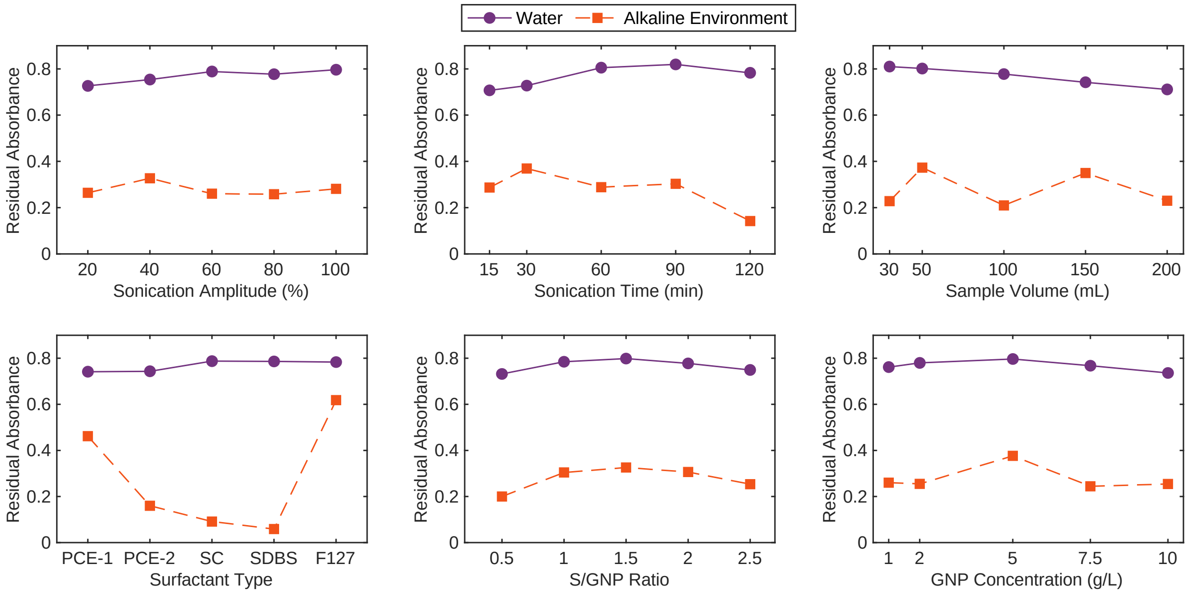

**Figure 5-5.** Main effects plot for residual absorbance after 24 hours in aqueous and alkaline media

### *5.5.2. Optimization using TOPSIS-based and PCA-based Taguchi Methods*

Seven performance measures (responses) given in Table 5-6 are converted into a single optimal response using TOPSIS and PCA-based optimization methods. For the TOPSIS-based optimization, the ranking scores $C_i^*$, i = 1,2,…, 25, which represent the surrogate responses for the multi-response optimization problem, are calculated and provided in Table 5-7. The mean responses by factor levels are determined and plotted in Figure 5-6. TOPSIS-based optimization leads the following values for each of six factors: Sonication amplitude: 100%; sonication time: 120 min; sample volume: 50 mL; surfactant type: SDBS; surfactant/GNP ratio: 2; and GNP concentration 1 g/L.

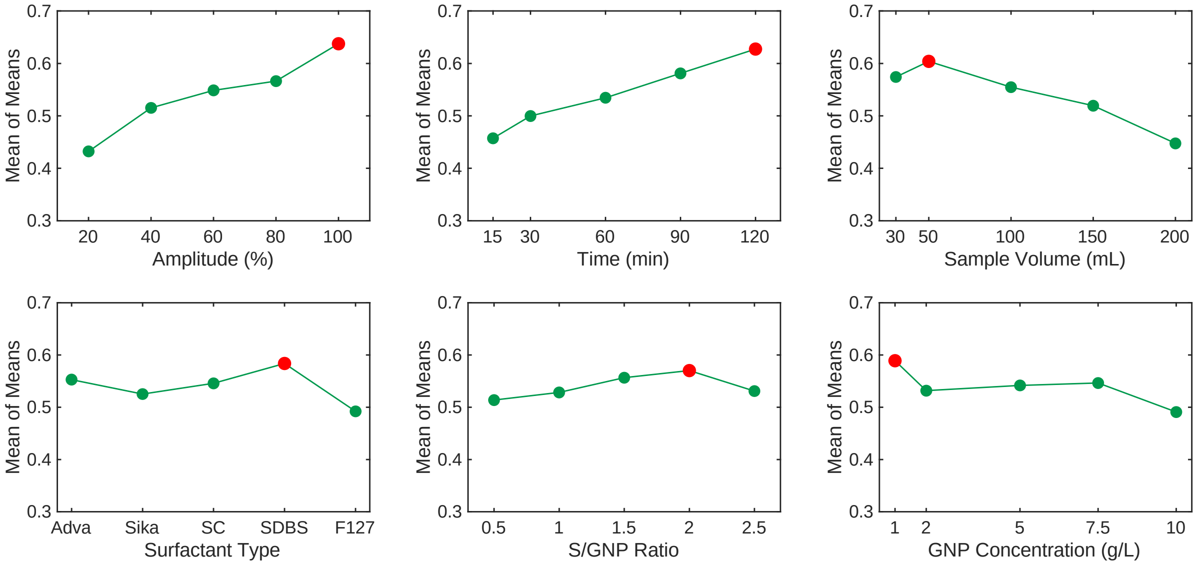

**Figure 5-6.** Mean plots and optimal levels of each factor based on TOPSIS optimization

For the PCA-based Taguchi method, the principal components ($P_i$) were determined first. The eigenvalues for $P_1$ to $P_7$ are 0.30, 0… Figure 5-7 shows the accountability proportions and their cumulative percentages. The first three principal components have the predominant percentage of variance with a total of 90%, almost the total variability (98.7%) can be accounted by the first five principal components. The first five principal components for each experiment are calculated and shown in Table 5-8.

**Table 5-7.** S/N ratios and TOPSIS method implementation

| Response | Decision matrix (S/N ratios) | | | | | | | Weighted normalized decision matrix | | | | | | | $S_i^*$ | $S_i^-$ | $C_i^*$ |
|---|---|---|---|---|---|---|---|---|---|---|---|---|---|---|---|---|---|
| | R1 | R2 | R3 | R4 | R5 | R6 | R7 | $v_{i1}$ | $v_{i2}$ | $v_{i3}$ | $v_{i4}$ | $v_{i5}$ | $v_{i6}$ | $v_{i7}$ | | | |
| Weight | 1/7[b] | 1/7 | 1/7 | 1/7 | 1/7 | 1/7 | 1/7 | | | | | | | | | | |
| 1 | -53.44[b] | 24.49 | -10.02 | -11.47 | -3.92 | 9.30 | -10.15 | -0.0292[b] | 0.0268 | -0.0391 | -0.0399 | -0.0453 | 0.0187 | -0.0113 | 0.0937[c] | 0.0694[d] | 0.4253[e] |
| 2 | -52.96 | 25.68 | -11.28 | -13.85 | -2.83 | 10.80 | -9.50 | -0.0290 | 0.0281 | -0.0440 | -0.0482 | -0.0327 | 0.0217 | -0.0105 | 0.0973 | 0.0713 | 0.4227 |
| 3 | -51.76 | 32.72 | -11.86 | -13.76 | -1.41 | 17.82 | -15.61 | -0.0283 | 0.0358 | -0.0463 | -0.0479 | -0.0163 | 0.0358 | -0.0173 | 0.0939 | 0.0802 | 0.4607 |
| 4 | -52.50 | 30.49 | -11.26 | -6.99 | -2.19 | 23.94 | -17.30 | -0.0287 | 0.0334 | -0.0439 | -0.0243 | -0.0253 | 0.0481 | -0.0192 | 0.0783 | 0.0893 | 0.5328 |
| 5 | -52.29 | 22.30 | -12.58 | -14.52 | -3.78 | -8.54 | -8.58 | -0.0286 | 0.0244 | -0.0491 | -0.0505 | -0.0437 | -0.0172 | -0.0095 | 0.1211 | 0.0580 | 0.3240 |
| 6 | -51.60 | 28.80 | -9.62 | -12.80 | -2.83 | 19.98 | -12.08 | -0.0282 | 0.0315 | -0.0375 | -0.0445 | -0.0327 | 0.0401 | -0.0134 | 0.0873 | 0.0823 | 0.4855 |
| 7 | -52.01 | 28.91 | -6.90 | -5.08 | -2.93 | 23.50 | -21.11 | -0.0285 | 0.0316 | -0.0269 | -0.0177 | -0.0338 | 0.0472 | -0.0234 | 0.0654 | 0.0898 | 0.5785 |
| 8 | -52.63 | 22.30 | -8.45 | -9.79 | -2.45 | -9.50 | -3.77 | -0.0288 | 0.0244 | -0.0330 | -0.0340 | -0.0283 | -0.0191 | -0.0042 | 0.1011 | 0.0691 | 0.4061 |
| 9 | -51.95 | 23.94 | -9.00 | -10.78 | -2.32 | 6.71 | -4.26 | -0.0284 | 0.0262 | -0.0351 | -0.0375 | -0.0268 | 0.0135 | -0.0047 | 0.0861 | 0.0752 | 0.4663 |
| 10 | -51.74 | 25.74 | 0.11 | -1.24 | -1.78 | 11.03 | -28.66 | -0.0283 | 0.0282 | 0.0004 | -0.0043 | -0.0206 | 0.0222 | -0.0318 | 0.0498 | 0.0901 | 0.6440 |
| 11 | -53.10 | 22.17 | -8.36 | -9.34 | -2.30 | -4.18 | -5.45 | -0.0291 | 0.0242 | -0.0326 | -0.0325 | -0.0266 | -0.0084 | -0.0060 | 0.0931 | 0.0691 | 0.4262 |
| 12 | -52.63 | 24.88 | -8.25 | -9.07 | -3.19 | 5.74 | -4.00 | -0.0288 | 0.0272 | -0.0322 | -0.0315 | -0.0369 | 0.0115 | -0.0044 | 0.0839 | 0.0749 | 0.4719 |
| 13 | -52.23 | 24.31 | -6.33 | -6.39 | -2.55 | 11.40 | -18.80 | -0.0286 | 0.0266 | -0.0247 | -0.0222 | -0.0295 | 0.0229 | -0.0208 | 0.0695 | 0.0744 | 0.5171 |
| 14 | -51.77 | 29.44 | 3.70 | 0.90 | -0.99 | 18.22 | -60.90 | -0.0283 | 0.0322 | 0.0144 | 0.0031 | -0.0114 | 0.0366 | -0.0675 | 0.0678 | 0.1054 | 0.6084 |
| 15 | -51.21 | 26.70 | 2.07 | 0.21 | -1.45 | 20.65 | -33.76 | -0.0280 | 0.0292 | 0.0081 | 0.0007 | -0.0168 | 0.0415 | -0.0374 | 0.0416 | 0.1059 | 0.7180 |
| 16 | -52.08 | 25.80 | -9.00 | -11.77 | -3.44 | 10.86 | -10.62 | -0.0285 | 0.0282 | -0.0351 | -0.0409 | -0.0397 | 0.0218 | -0.0118 | 0.0889 | 0.0714 | 0.4454 |
| 17 | -52.64 | 26.49 | -6.11 | -8.20 | -3.60 | 18.35 | -51.80 | -0.0288 | 0.0290 | -0.0238 | -0.0285 | -0.0416 | 0.0369 | -0.0574 | 0.0896 | 0.0662 | 0.4247 |
| 18 | -52.13 | 27.12 | 1.71 | -1.78 | -1.34 | 16.98 | -58.22 | -0.0285 | 0.0297 | 0.0067 | -0.0062 | -0.0155 | 0.0341 | -0.0646 | 0.0693 | 0.0935 | 0.5743 |
| 19 | -51.48 | 22.39 | 4.89 | 4.75 | -0.92 | -2.96 | -2.52 | -0.0282 | 0.0245 | 0.0191 | 0.0165 | -0.0107 | -0.0059 | -0.0028 | 0.0552 | 0.1208 | 0.6863 |
| 20 | -52.28 | 25.20 | 1.19 | -0.29 | -2.00 | 9.05 | -12.32 | -0.0286 | 0.0276 | 0.0046 | -0.0010 | -0.0231 | 0.0182 | -0.0137 | 0.0420 | 0.1003 | 0.7049 |
| 21 | -52.48 | 29.53 | -6.76 | -7.94 | -2.65 | 18.96 | -26.49 | -0.0287 | 0.0323 | -0.0264 | -0.0276 | -0.0306 | 0.0381 | -0.0294 | 0.0725 | 0.0775 | 0.5166 |
| 22 | -52.16 | 22.23 | -0.15 | -1.02 | -1.42 | -3.02 | -2.06 | -0.0285 | 0.0243 | -0.0006 | -0.0036 | -0.0164 | -0.0061 | -0.0023 | 0.0623 | 0.0986 | 0.6127 |
| 23 | -52.21 | 25.45 | 1.10 | -0.21 | -1.73 | 6.89 | -5.81 | -0.0286 | 0.0278 | 0.0043 | -0.0007 | -0.0200 | 0.0138 | -0.0064 | 0.0431 | 0.1035 | 0.7061 |
| 24 | -52.44 | 24.86 | -0.39 | -1.62 | -2.35 | 12.45 | -34.86 | -0.0287 | 0.0272 | -0.0015 | -0.0056 | -0.0272 | 0.0250 | -0.0387 | 0.0558 | 0.0856 | 0.6054 |
| 25 | -51.45 | 27.38 | 2.39 | 1.73 | -1.80 | 18.37 | -28.29 | -0.0282 | 0.0300 | 0.0093 | 0.0060 | -0.0208 | 0.0369 | -0.0314 | 0.0362 | 0.1077 | 0.7484 |
| | 261.0[a] | 130.6 | 36.6 | 41.1 | 12.4 | 71.1 | 128.8 | $A^*$ =-0.0280 | 0.0358 | 0.0191 | 0.0165 | -0.0107 | 0.0481 | -0.0023 | | | |
| | | | | | | | | $A^-$ =-0.0291 | 0.0242 | -0.0491 | -0.0505 | -0.0437 | -0.0191 | -0.0675 | | | |

a The square root of sum of squares of each element in the columns.

b 1/7*[(-53.44)/(261.0)] = -0.0292.

c $\{[(-0.0292) - (-0.0280)]^2 + \ldots\ldots + [(-0.0113) - (-0.0280)]^2\}^{1/2} = 0.0937$.

d $\{[(-0.0292) - (-0.0291)]^2 + \ldots\ldots + [(-0.0113) - (-0.0291)]^2\}^{1/2} = 0.0694$.

e 0.0694/(0.0694+0.0937) = 0.4253.

$A^*$ maximum $v_i$.

$A^-$ minimum

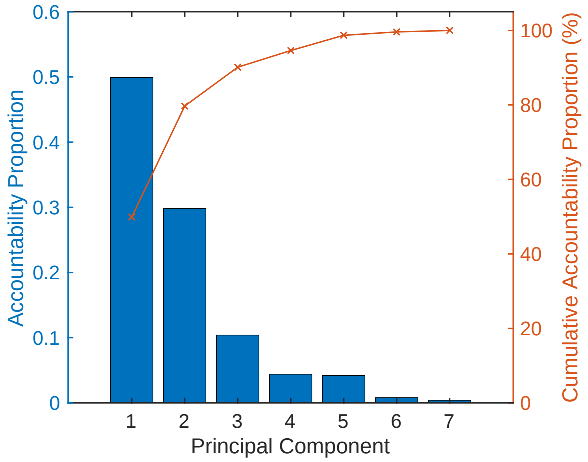

**Figure 5-7.** Principal components with their accountability proportions and cumulative percentages

**Table 5-8.** Principal component analysis results.

| | **PC1** | **PC2** | **PC3** | **PC4** | **PC5** | **Composite PC** |
|---|---|---|---|---|---|---|
| **Proportion** | **0.499** | **0.298** | **0.104** | **0.044** | **0.042** | |
| 1 | 0.0275 | -0.0806 | -0.5714 | -0.4268 | -0.7655 | -0.1206 |
| 2 | 0.1693 | -0.1685 | -0.9120 | -0.2372 | -0.6189 | -0.0970 |
| 3 | 0.6923 | -0.6669 | -1.5434 | -0.0719 | -0.4285 | -0.0349 |
| 4 | 0.6935 | -0.6043 | -1.1307 | -0.2598 | -0.7890 | 0.0038 |
| 5 | -0.1095 | 0.2887 | -0.8450 | -0.4707 | -0.1413 | -0.0831 |
| 6 | 0.5475 | -0.5011 | -1.2634 | -0.5766 | -0.3951 | -0.0495 |
| 7 | 0.8385 | -0.4857 | -0.9819 | -0.6085 | -0.6459 | 0.1177 |
| 8 | 0.2538 | 0.5359 | -0.9295 | -0.1962 | -0.3958 | 0.1644 |
| 9 | 0.4507 | 0.1218 | -1.1696 | -0.4162 | -0.3776 | 0.1054 |
| 10 | 1.2787 | 0.0859 | -0.9170 | -0.4256 | -0.4344 | 0.5313 |
| 11 | 0.2682 | 0.4561 | -0.8221 | -0.1092 | -0.5796 | 0.1551 |
| 12 | 0.3075 | 0.0878 | -0.8988 | -0.4686 | -0.6177 | 0.0396 |
| 13 | 0.6934 | 0.0156 | -0.8690 | -0.4498 | -0.4939 | 0.2198 |
| 14 | 1.8320 | -0.3192 | -0.7350 | -0.1433 | -0.3739 | 0.7206 |

| | | | | | | |
|---|---|---|---|---|---|---|
| 15 | 1.5992 | -0.1154 | -1.0303 | -0.5491 | -0.4021 | 0.6154 |
| 16 | 0.3356 | -0.1636 | -0.9743 | -0.6070 | -0.4152 | -0.0268 |
| 17 | 0.7071 | -0.5020 | -0.3491 | -0.4546 | -0.3982 | 0.1302 |
| 18 | 1.5476 | -0.2335 | -0.6037 | -0.1396 | -0.3782 | 0.6178 |
| 19 | 1.4595 | 0.8793 | -1.1732 | -0.4531 | -0.5313 | 0.8260 |
| 20 | 1.1210 | 0.2771 | -0.9000 | -0.4475 | -0.7260 | 0.4982 |
| 21 | 0.7543 | -0.4820 | -0.8902 | -0.3341 | -0.6394 | 0.0987 |
| 22 | 0.9854 | 0.7216 | -1.0486 | -0.3104 | -0.5749 | 0.5599 |
| 23 | 1.1218 | 0.3561 | -1.0318 | -0.4066 | -0.7455 | 0.5094 |
| 24 | 1.1082 | 0.0358 | -0.5917 | -0.3962 | -0.5677 | 0.4609 |
| 25 | 1.5302 | -0.0670 | -0.9883 | -0.5863 | -0.5397 | 0.5924 |

These results are integrated into a comprehensive performance characteristics index using Equation 5-16 as described in Section 5.4.2. The mean values of this index by factor levels are calculated and plotted in Figure 5-8. PCA-based optimization leads the following values for each of six factors: Sonication amplitude: 100%; sonication time: 120 min; sample volume: 30 mL; surfactant type: F127; surfactant/GNP ratio: 1.5; and GNP concentration 1 g/L. Compared to the TOPSIS-based optimization, the optimal parameters for the factors sample volume, surfactant type and surfactant/GNP ratio are changed in the PCA-based optimization.

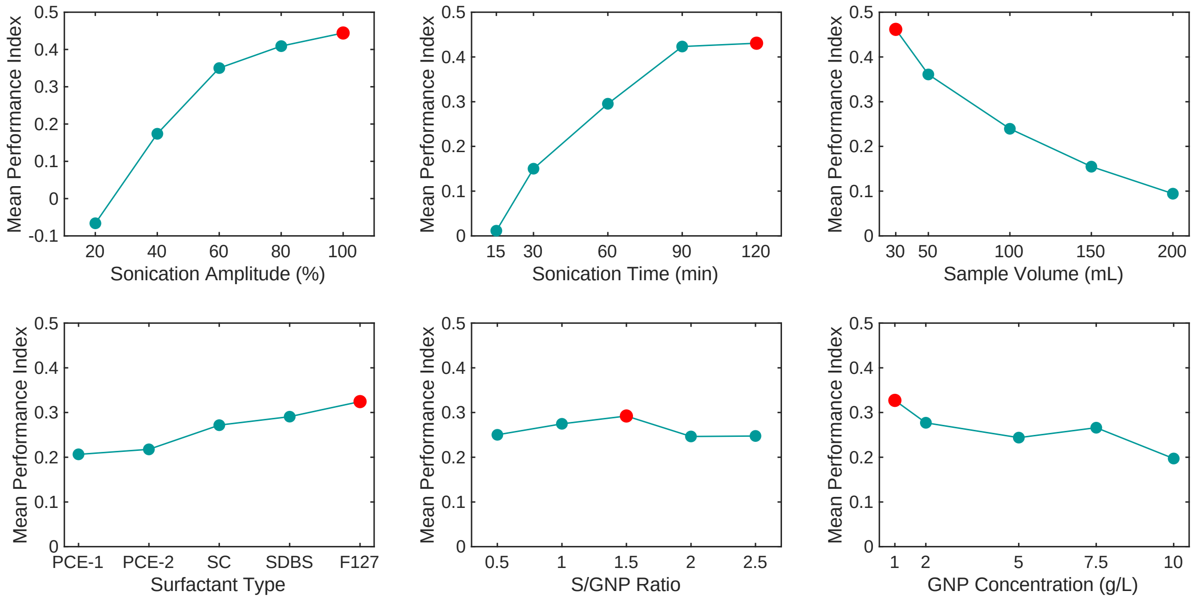

**Figure 5-8.** Mean plots and optimal levels of each factor based on PCA optimization

To gain an understanding about the dominant factor on major principal components, the first two principal components were computed for each of 25 experiments and the corresponding score plot is illustrated in Figure 5-9. The data is classified into two groups (blue and orange) by k-means method. The factors sonication time, sonication amplitude, and sample volume are represented with energy density defined as follows:

$$Energy\ Density = \frac{Amplitude \times time}{volume}$$

The corresponding energy density values are plotted in Figure 5-9 as varying dot size. It can be seen that the blue group has a smaller dot size, while the orange group has significantly larger dot size. This indicates that the energy density is the main factor in the classification of these two groups.

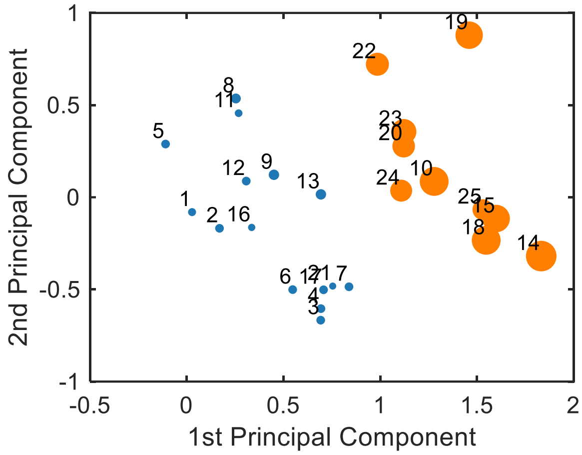

**Figure 5-9.** First two principal components for each experiment with corresponding energy densities

The analysis of variance (ANOVA) was conducted to quantify the relative importance and influence of each factor in the TOPSIS-based and PCA-based analysis results and the obtained results were presented in Table 5-9 and Table 5-10, respectively. The factors affecting the both the TOPSIS-based and PCA-based optimization performance are sonication amplitude, sonication time and sample volume. These results confirm that the sonication energy density has significant influence on the dispersion performance of GNPs in cementitious composites.

**Table 5-9.** Results of ANOVA for the TOPSIS performance

| **Factor** | **DF** | **SS** | **MS** | **Contribution (%)** | **Rank** |
|---|---|---|---|---|---|
| Sonication amplitude | 4 | 0.1124 | 0.0281 | 33.86 | 1 |
| Sonication time | 4 | 0.0891 | 0.0223 | 26.82 | 2 |
| Sample volume | 4 | 0.0723 | 0.0181 | 21.76 | 3 |
| Surfactant | 4 | 0.0231 | 0.0058 | 6.97 | 5 |
| Surfactant/GNP ratio | 4 | 0.0105 | 0.0026 | 3.15 | 6 |
| GNP concentration | 4 | 0.0247 | 0.0061 | 7.43 | 4 |
| Total | 24 | 0.3320 | - | 100 | |

Notes: DF: degree of freedom; SS: adjusted sum of squares; MS: adjusted mean of squares

**Table 5-10.** Results of ANOVA for the PCA performance

| Factor | DF | Adj SS | Adj MS | Contribution (%) | Rank |
|---|---|---|---|---|---|
| Sonication amplitude | 4 | 0.8912 | 0.2228 | 42.47 | 1 |
| Sonication time | 4 | 0.6548 | 0.1637 | 31.21 | 2 |
| Sample volume | 4 | 0.4492 | 0.1123 | 21.41 | 3 |
| Surfactant | 4 | 0.0496 | 0.0124 | 2.36 | 4 |
| S/GNP ratio | 4 | 0.0086 | 0.0021 | 0.40 | 6 |
| GNP concentration | 4 | 0.0451 | 0.0112 | 2.15 | 5 |
| Total | 24 | 1.5855 |  | 100 |  |

Notes: DF: degree of freedom; SS: adjusted sum of squares; MS: adjusted mean of squares

## 5. 6. Further Dispersion Studies

From previous section, it can be concluded that higher sonication amplitude, longer sonication time and smaller sample volume might have the greatest influence on the dispersion quality of GNPs. Although different surfactants led to similar dispersion performances, the SDBS and Pluronic F127 are the selected surfactants after implementing the TOPSIS-based and PCA-based Taguchi methods, respectively. Before casting graphene-cement composites, an additional study is conducted to determine the dispersion parameters for the GNP addition. To this end, SDBS and Pluronic F-127 as well as the hybrid use of these two surfactants (named as Hybrid) are considered to disperse GNPs. The surfactant to GNPs (S/GNP) ratio is kept as 2, while GNP concentration is selected to be 1 g/L. A sonication study is conducted to determine the sonication parameters. In this case, the sonication amplitude and sample volume are kept constant and the sonication time is varied. A sample volume of 50 mL and sonication amplitude of 60% are used. Note that although increasing the sonication amplitude is found to improve dispersion performance in previous section, a very high sonication amplitude both leads to a rapid temperature increase and also may cause structural defects in nanoparticles [96]. Therefore, the sonication amplitude is selected to be 60% instead of 100%. In order to determine the optimal sonication time, the dispersion quality of GNPs in aqueous suspension is studied with sonication times of 15, 30, 60, 90, and 120 min. The surfactant and GNPs are added into 50 g water and ultrasonicated for the desired time. The suspension is then diluted to 0.02 g/L in both aqueous solution and simulated pore solution. The dispersion plan and procedures are presented in Table 5-11 and Figure 5-10.

**Table 5-11.** Dispersion plan with different surfactants

| Dispersion | GNPs (g/L) | SDBS (g/L) | F127 (g/L) | Water (mL) | S/GNP |
|---|---|---|---|---|---|
| SDBS | 1 | 2 | -- | 50 | 2 |
| F127 | 1 | -- | 2 | 50 | 2 |
| Hybrid | 1 | 1 | 1 | 50 | 2 |

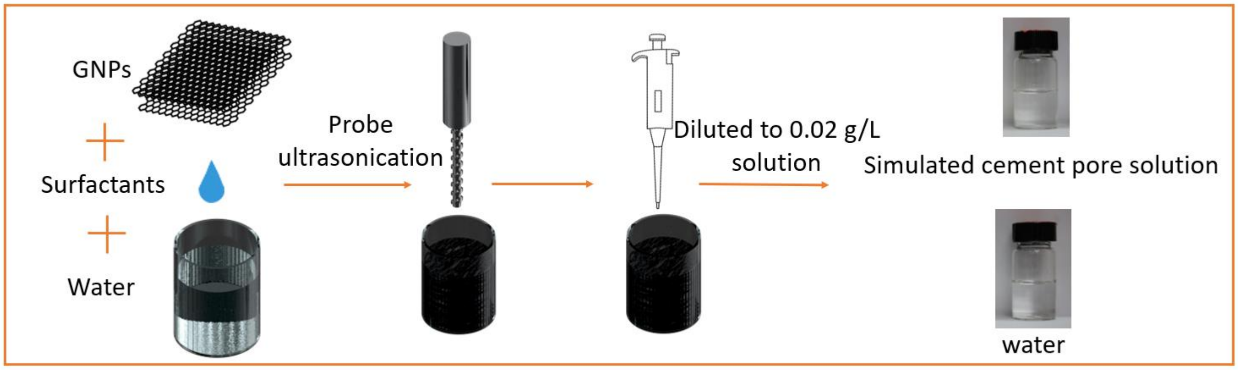

**Figure 5-10.** Dispersion procedures.

### *5.6.1. Characterization Results*

Figure 5-11 presents the variation of average particle size of GNPs dispersed by different surfactants with different sonication time. A decreasing trend is observed with increasing sonication time, but the rate of this decrease remains low. The GNPs dispersed with F127 have slightly larger particle size when the sonication duration is less than 90 min, comparing with the one prepared with SDBS and Hybrid. Overall, the average particle size remains small ranging from 355 nm to 428 nm in all cases.

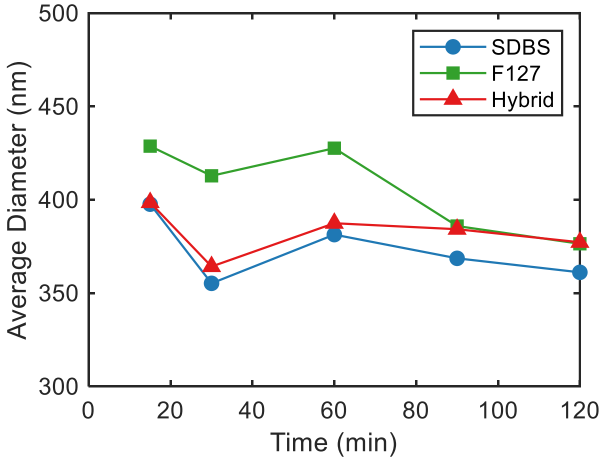

**Figure 5-11.** Average particle size of GNPs.

Figure 5-12 show the variation of absorbance in aqueous media and alkaline environment for the dispersion of GNPs with different surfactants. It can be seen that the absorbance in aqueous media and alkaline environment increases with the increasing sonication time. The absorbance decreases when the GNPs are added into alkaline environment, which should be due to the re-agglomeration of GNPs by divalent cations. This reduction increases with the increasing sonication time, which could be attributed to the availability of smaller size GNP particles in these cases. The GNPs with smaller size have a higher chance of re-agglomeration. However, the absorbance of the GNPs dispersed with F127 remains the same, indicating that GNPs with F127 have a better stability in alkaline environment.

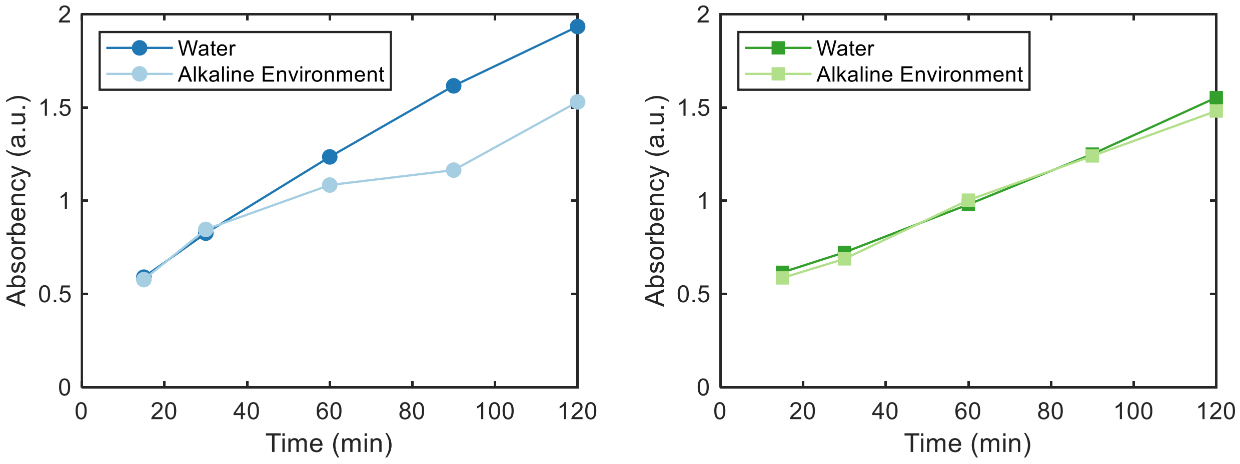

(a) (b)

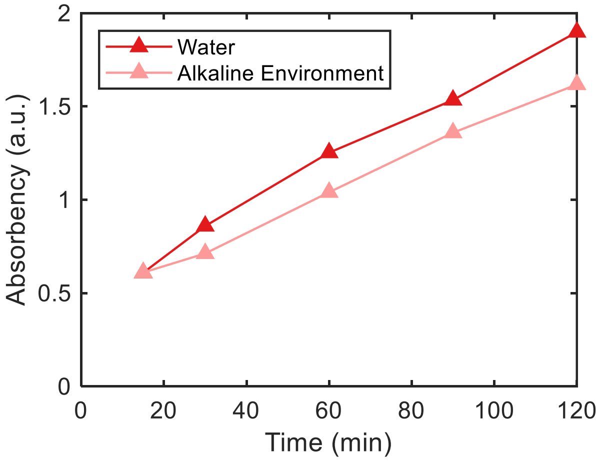

(c)

**Figure 5-12.** UV-vis absorbance of GNPs dispersed with (a) SDBS; (b) F127; and (c) Hybrid in aqueous and alkaline media

Figure 5-13 compares the absorbance of GNPs with different surfactants in aqueous media and alkaline environment, respectively. It can be seen that the GNPs with SDBS and Hybrid surfactants produces the almost same absorbance in aqueous media, while the GNPs with F127 has a smaller absorbance. However, in alkaline environment, the measured absorbance of GNP suspensions with different surfactants is similar.

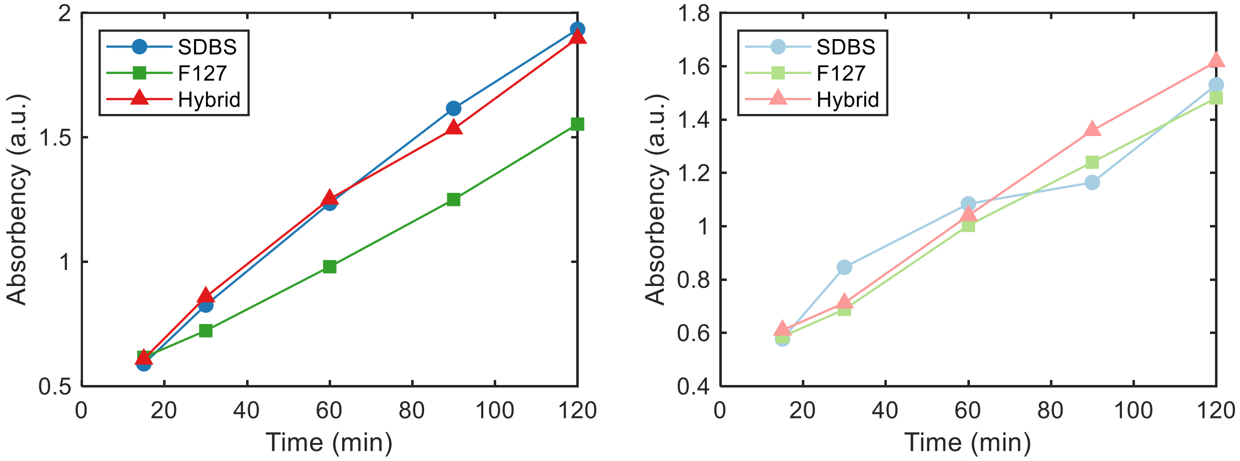

(a) (b)

**Figure 5-13.** Comparison of the UV-vis absorbance with different surfactants in (a) aqueous; and (b) alkaline media.

Figure 5-14 shows the zeta potential of GNPs with different surfactants in aqueous media and alkaline environment. In aqueous media, all samples have |ζ| larger than 15 mV or close to 15 mV, especially the GNPs dispersed with SDBS which have a considerably higher |ζ|. However, the |ζ| for all surfactants decreases in alkaline environment, implying the instability of GNPs in alkaline environment.

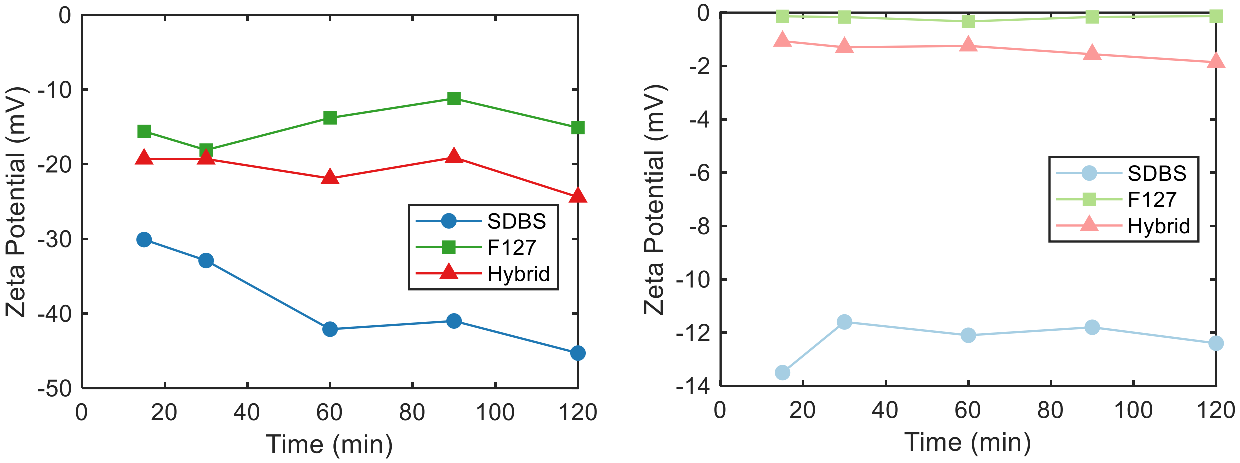

(a) (b)

**Figure 5-14.** Comparison of the zeta potential with different surfactants in (a) aqueous; and (b) alkaline media.

As discussed in Section 5.5.1, the ionic surfactant (SDBS) and non-ionic surfactant (F127) have different stabilization mechanisms. Thus, the zeta potential might not be precise measure to describe the dispersion stability. The stability of agglomerates can also be assessed using the end-over-end shaking method [94]. The residual absorbance after 24 h and 24 h with shaking are presented in Figure 5-15. It can be seen that the residual absorbance is higher in samples with longer sonication time. In aqueous media, the residual absorbance after 24 h remains approximately 85% in the samples with SDBS and Hybrid, indicating a better stability. The samples with F127 have a lower residual absorbance, especially in the samples prepared with less sonication time. The absorbance recovers to almost 100% when the sonication time reaches 60 min. The absorbance value for the GNP suspensions with F127 only recovers to around 85%. Although the SDBS and Hybrid present a better stability in aqueous media, the stability in alkaline environment shows the opposite results. The residual absorbance values range from 69% to 92% for different sonication times in the samples with F127. However, the residual absorbance of the samples with SDBS and Hybrid drops to less than 10%. After shaking, the absorbance of solutions with F127 recovers to 100%, while those with SDBS and Hybrid only recover to around 50% and 70%.

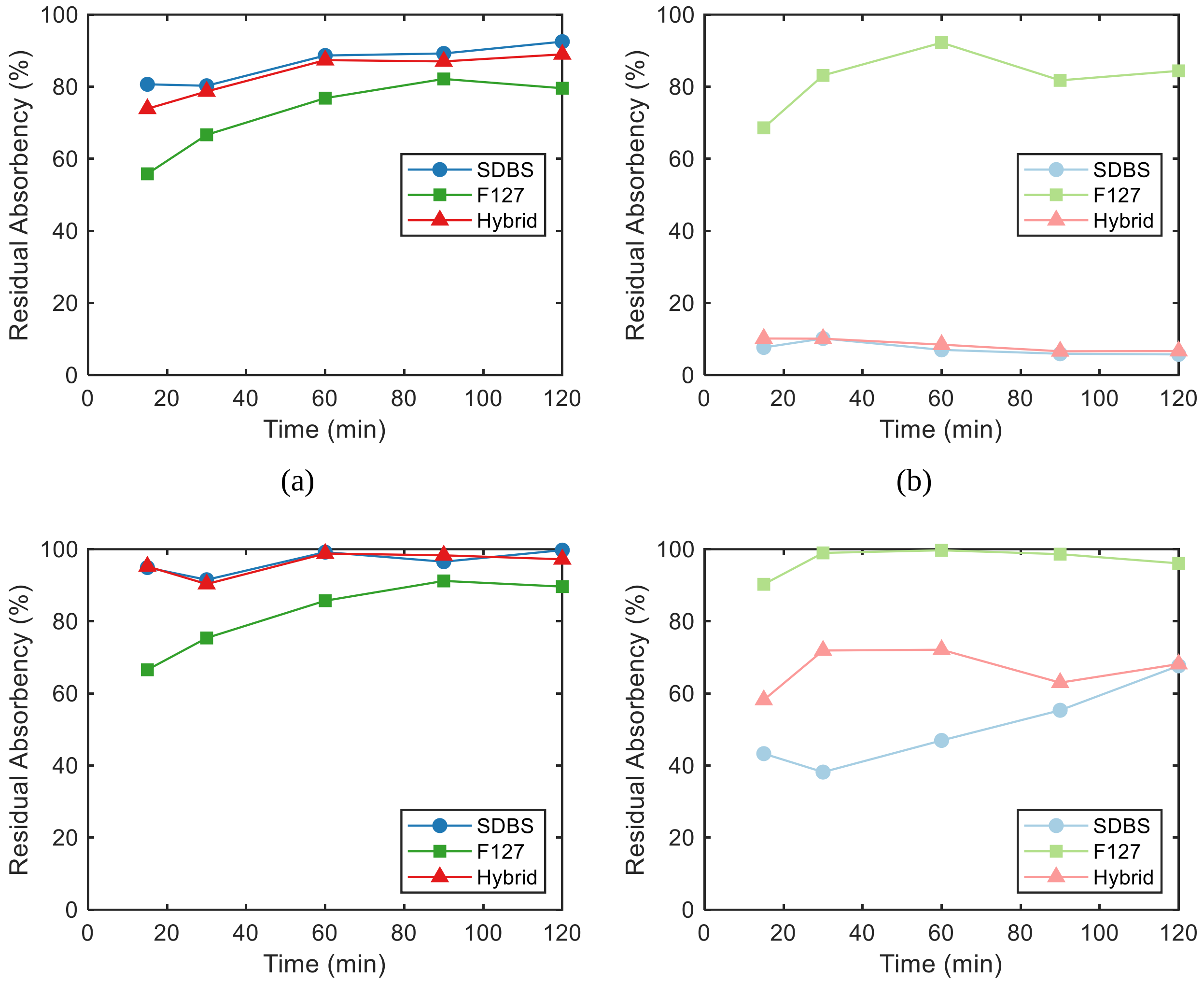

(a) (b)

(c) (d)

**Figure 5-15.** Residual absorbance of solutions after 24 h in (a) aqueous; (b) alkaline media; and after 24 h and shaking in (c) aqueous; (d) alkaline media.

Figure 5-16 to 5-18 shows the photos obtained from the visual observation of GNP suspensions with different surfactant and different sonication times (15 min to 120 min) in aqueous media and alkaline environment for immediately after sonication, 24 hours after sonication, and 24 hours after sonication and shaking, respectively. The color of solutions is darker with increasing sonication time, which is consistent with the UV-vis absorbance results. The GNPs in aqueous media present a good stability as no sediments are observed. The samples prepared with different surfactants show good dispersion after being added to the alkaline environment without any observed agglomeration. After 24 hours, the GNPs tend to deposition. The sediments are observed in samples with the SDBS and Hybrid and the solution are almost clear. As for the samples with the F127, although the color of solution still exists, the color is less dark compared with the initial solution. The solution visually recovers to color solution without observed agglomerations after shaking, indicating that these agglomerations are easily broken up by shaking.

SDBS – Aqueous Media SDBS – Alkaline Media

(a)

F127 – Aqueous Media F127 – Alkaline Media

(b)

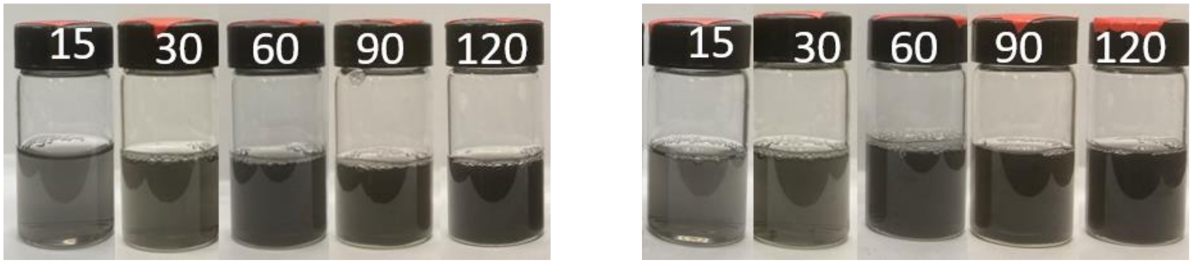

Hybrid – Aqueous Media Hybrid – Alkaline Media

(c)

**Figure 5-16.** Visual observation of GNP suspensions with (a) SDBS, (b) F-127, and (c) Hybrid in aqueous and alkaline media after sonication.

SDBS – Aqueous Media

SDBS – Alkaline Media

(a)

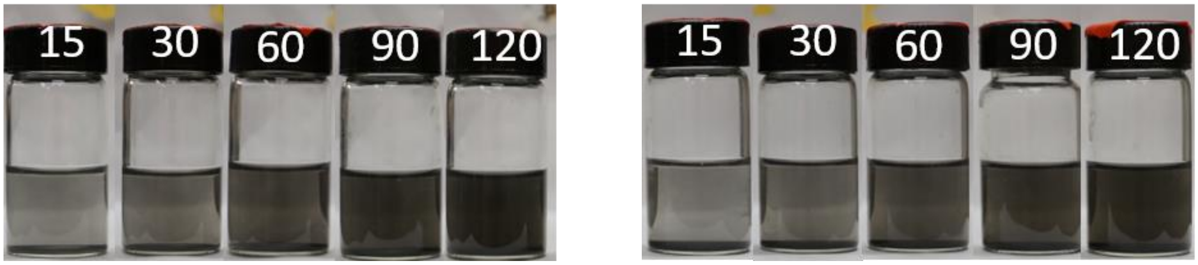

F127 – Aqueous Media

F127 – Alkaline Media

(b)

Hybrid – Aqueous Media

Hybrid – Alkaline Media

(c)

**Figure 5-17.** Visual observation of GNP suspensions with (a) SDBS, (b) F-127, and (c) Hybrid in aqueous and alkaline media 24 hours after sonication.

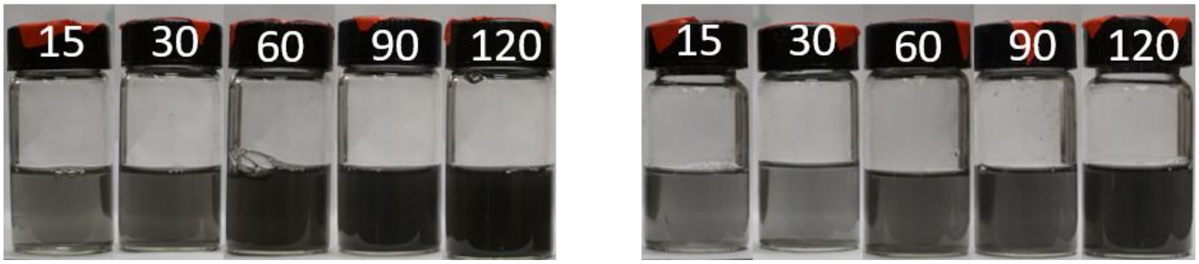

SDBS – Aqueous Media SDBS – Alkaline Media

(a)

F127 – Aqueous Media F127 – Alkaline Media

(b)

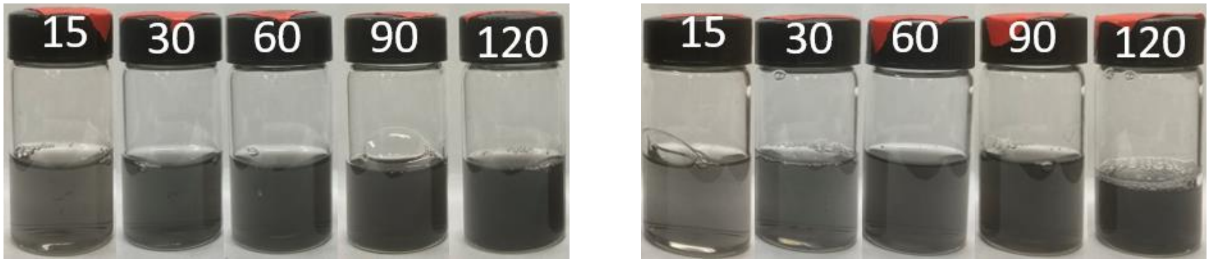

Hybrid – Aqueous Media Hybrid – Alkaline Media

(c)

**Figure 5-18.** Visual observation of GNP suspensions with (a) SDBS, (b) F-127, and (c) Hybrid in aqueous and alkaline media 24 hours after sonication and shaking.

All the characterization results (absorbency, zeta potential, and residual absorbency in aqueous and alkaline media) are converted into a single performance measure using TOPSIS method and the final score of GNPs with different surfactants and sonication time are summarized in Figure 5-19. The performance score increases with increasing sonication time and is saturated when the sonication time reaches 60 min for all surfactants, indicating that 60 min is sufficient for dispersion of GNPs.

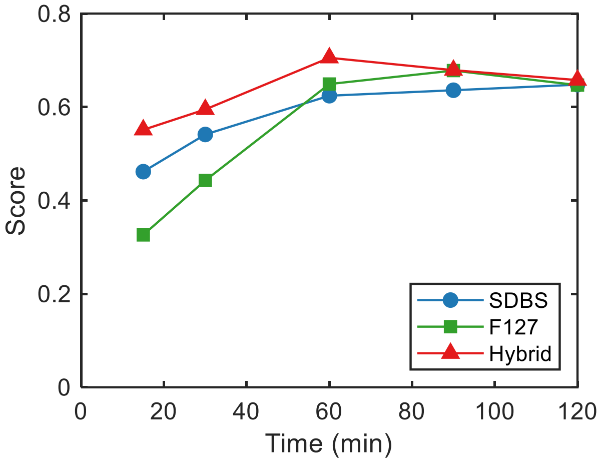

**Figure 5-19.** Final score plot of GNPs with different surfactants and sonication time.

## 5. 7. Summary

In this chapter, Taguchi-based TOPSIS and Taguchi-based PCA optimization methods are used to determine the optimal parameters for the dispersion of GNPs in cement-based composites. The findings of this study indicated that the sonication energy has the greatest influence on the dispersion quality of GNPs, while the SDBS and Pluronic F127 exhibit better performance than the other three surfactants considered. Further dispersion experiments are conducted considering the use of the SDBS, Pluronic F127, and their hybrid use to determine optimal sonication parameters. It was found that a sonication duration of 60 min is sufficient for the dispersion of GNPs, while further increasing the sonication time do not improve the dispersion performance. In addition, the SDBS, which is an ionic surfactant, the Pluronic F-127, which is a non-ionic surfactant, or their hybrid use result in a similar dispersion performance, while the hybrid surfactant exhibits better performance for most of the sonication durations. The following conclusions can be make based on the above results:

- TOPSIS-based optimization leads the following values for each of six factors: Sonication amplitude: 100%; sonication time: 120 min; sample volume: 50 mL; surfactant type: SDBS; surfactant/GNP ratio: 2; and GNP concentration 1 g/L.
- PCA-based optimization leads the following values for each of six factors: Sonication amplitude: 100%; sonication time: 120 min; sample volume: 30 mL; surfactant type: F127; surfactant/GNP ratio: 1.5; and GNP concentration 1 g/L.
- Compared to the TOPSIS-based optimization, the optimal parameters for the factors sample volume, surfactant type and surfactant/GNP ratio are changed in the PCA-based optimization. But the results of the two levels are close.
- Zeta potential is not precise to describe the stability of GNPs dispersed with superplasticizer and non-ionic surfactants as their stabilization mechanism is dominant by steric hindrance. It is essential to combine the zeta potential and residual absorbance and evaluate the stability.
- The energy density, which is calculated as amplitude × time /volume, is found to be the major factor that greatly influence the dispersion of GNPs based on PCA and ANOVA results.

# 6. MECHANICAL AND DURABILITY PROPERTIES OF GRAPHENE-MORTAR COMPOSITES

## 6. 1. Overview

This chapter explores the influence of GNP addition on the mechanical properties and durability of cement-based composites. Two types of GNPs with different lateral size (<2 µm and 25 µm) and specific surface area (300 $m^2/g$ and 120 $m^2/g$) are used in this study. The GNP concentration is varied from 0.05% to 0.1% by weight of cement in all mixtures. In order to study the effect of dispersion agents, SDBS, Pluronic F127 and hybrid of two surfactants are utilized to disperse and stabilize GNP particles in aqueous solution. The mechanical properties are assessed by conducting compressive strength test, while the durability is evaluated by performing the sorptivity and permeable porosity tests. In order to explore the effect of GNPs on hydration process and microstructure, the thermal gravimetric analysis (TGA) and scanning electron microscopy (SEM) tests are carried out at 28 days.

## 6. 2. Materials

Portland Cement type I/II and sand are used to prepare mortar samples. GNP M-25 and C-300 with different lateral size (<2 µm and 25 µm) and specific surface area (300 $m^2/g$ and 120 $m^2/g$) obtained from XG Science are used in this study. The properties of GNPs are shown in Table 6-1. Two types of surfactants, Sodium Dodecylbenzene Sulfonate (SDBS) and Pluronic F-127 (F127) are applied in this study to help disperse GNPs in water. A polycarboxylate-based superplasticizer, AdvaCast 555, is utilized to achieve the desired workability. The tributyl phosphate (TBP) is used as defoamer to eliminate bubbles generated during the ultrasonication process and entrapped air caused by the use of surfactants [159].

**Table 6-1.** Properties of GNPs

| **Properties** | **M-25** | **C-300** |
|---|---|---|
| Surface Area (m2/g) | 120~150 | 300 |
| Diameter (µm) | 25 | <2 |
| Thickness (nm) | 6-8 | 1-2 |
| Density (g/cc) | 2.2 | 0.2-0.4 |

| | | |
|---|---|---|
| Carbon Content (%) | >99.5 | >99.5 |

## 6. 3. Mix Design and Sample Preparation

Thirteen batches of specimens are prepared as per ASTM C109. The proportion of water: cement: sand ratio is adopted to be 0.485:1:2.75. Three levels of GNPs, i.e., 0%, 0.05% and 0.1% by weight of cement are designed. All the dry materials are placed into a Hobart mixer and mixed for 3 min at a low speed. The GNP solution together with the water, SP and TBP are added into the mixer and all the materials are mixed for another 5 min at high speed. The prepared mixtures are then poured into 50 mm × 50 mm × 50 mm cubic molds for compressive strength test and durability test, respectively. The specimens are demolded after 24 h and cured under water until 28 days. The detailed mix design is listed in Table 6-2.

**Table 6-2.** Mixture design

| **Batch** | **GNP** | | **Dispersion agent** | | **TBP wt.%** |
|---|---|---|---|---|---|
| | **Type** | **wt.%** | **SDBS wt.%** | **F127 wt.%** | |
| Control | -- | -- | -- | -- | -- |
| SC005 | C300 | 0.05 | 0.1 | -- | 0.2 |
| SC01 | C300 | 0.1 | 0.2 | -- | 0.2 |
| FC005 | C300 | 0.05 | -- | 0.1 | 0.2 |
| FC01 | C300 | 0.1 | -- | 0.2 | 0.2 |
| HC005 | C300 | 0.05 | 0.05 | 0.05 | 0.2 |
| HC01 | C300 | 0.1 | 0.1 | 0.1 | 0.2 |
| SM005 | M25 | 0.05 | 0.1 | -- | 0.2 |
| SM01 | M25 | 0.1 | 0.2 | -- | 0.2 |
| FM005 | M25 | 0.05 | -- | 0.1 | 0.2 |
| FM01 | M25 | 0.1 | -- | 0.2 | 0.2 |
| HM005 | M25 | 0.05 | 0.05 | 0.05 | 0.2 |
| HM01 | M25 | 0.1 | 0.1 | 0.1 | 0.2 |

## 6. 4. Test Methods

### *6.4.1. Compressive Strength Test*

The compressive strength tests are conducted on three cubic specimens at 28 days as per ASTM C109 for each mixture.

### *6.4.2. Thermogravimetric Analysis (TGA)*

The thermal behavior of mortar samples is analyzed using Thermogravimetric Analysis (TGA). At 28 days, the sample are collected from the core of cubic specimens and dried in the oven at 60 °C to stop hydration. The samples are then grounded and sieved through 53 μm sieve. The powdered sample is heated from room temperature to 1000 °C at 10 °C/min under nitrogen flow. TGA measures the mass loss of mortar samples as a result of decomposition of cement hydrates in mortar[173]. The decomposition can be divided into three phases [174]: (i) evaporable water and the C-S-H decomposition that occurs between 25 °C and 350 °C; (ii) the dihydroxylation of calcium hydroxide (CH) that occurs approximately between 350 °C and 550 °C [175]; (iii) the decarbonation of $CaCO_3$ that occurs between 550°C to 800°C. The CH content is determined using the following equation:

$$CH\%=W_{CH}\times\frac{74.1}{18.0}$$

where $W_{CH}$ is the mass loss during dehydration of CH as percentage of the initial mass (%). The ratio of 74.1:18.0 is the molar weight ratio of calcium hydroxide to water.

The hydration degree is calculated using the method described in Bhatty [176] as:

$$W_B=Ldh+Ldx+0.41(Ldc)$$

$$\alpha=\frac{W_B}{0.24}$$

where *Ldh*, *Ldx*, and *Ldc* are the mass loss in percentage due to the dehydration of C-S-H, dihydroxylation of CH and decarbonation of $CaCO_3$, respectively.

### 6.4.3. *Sorptivity Test*

The sorptivity test is conducted on cubic specimens as per ASTM C1585[177]. These specimens are dried in the oven at 60 °C until the daily mass variation within 0.1%. The side surface of each specimen is sealed with low permeable tape. The end of the specimen that will not be exposed to water is sealed with a plastic sheet to prevent evaporation. The specimen is weighed and placed on the support device in the water. The mass change of specimens is recorded after an interval of 1, 5, 10, 20, 30, 60 min and every hour up to 6 h. The absorption, $I$, is calculated as:

$$I = \frac{m_t}{a \times d}$$

where $m_t$ is the mass change of specimens (g), $a$ is the exposed area ($mm^2$), and $d$ is the density of water ($g/mm^3$). The sorptivity is defined as the slope of the $I$ against the square root of time curve.

### 6.4.4. *Porosity Test*

The porosity test is performed on cubic specimens as per ASTM C642 [178]. The specimens are oven dried at a temperature of 110 ± 5 °C for not less than 24 h and then cooled to room temperature. The mass of specimens is measured. Then the specimens are immersed in water at approximately 21 °C for not less than 48 h. The mass of surface-dry specimens is determined. The specimens are then subjected to water boiling in a metal container for not less than 5 h, followed by cooling for not less than 14 h to a final temperature of 20 to 25 °C. The mass of surface-dry specimens after boiling and the mass in water of specimens are recorded. The volume of permeable voids (%) is calculated as:

$$(C - A)/(C - D) \times 100$$

where:

$A$ = mass of oven-dried sample in air, g

$C$ = mass of surface-dry sample in air after immersion and boiling, g

$D$ = apparent mass of sample in water after immersion and boiling, g

## 6. 5. Results and Discussions

### *6.5.1. Compressive Strength*

Figure 6-1 shows the compressive strength of control specimens and specimens with different GNP types fabricated with different dispersion agents at different GNP concentrations. The standard deviation of each batch is lower than 5%, indicating that the dispersion process is effective and the GNPs are evenly dispersed in specimens. The addition of M25 GNPs or C300 GNPs significantly improves the compressive strength. This enhancement in compressive strength could be attributed to the following reasons: firstly, the GNPs with its relatively large surface area provides a nucleation site and enables production of more hydration products; secondly, GNPs can fill in pores and refine the cement matrix, leading to a more compacted structure; lastly, GNPs bridges the cracks, preventing and delaying formation of microcracks [55,70,141].

For both GNP types, a decrease in compressive strength is observed with the increasing GNP concentrations. The higher concentration of GNPs may cause the increasing number of agglomerations, resulting in reduction of interfacial bond between GNPs and hydration products [88]. Besides, the use of surfactants may increase the amount of entrapped air in matrix [179]. Though TBP is used to eliminate the entrapped air, the amount of TBP might not be sufficient for high concentration of surfactants.

For the specimens with the M25 GNPs, the compressive strength increases by a minimum of 25% and a maximum of 36%. All specimens produce similar strength except FM01 with a slightly lower compressive strength. For the C300 GNPs, the largest increase in compressive strength is 32% when SDBS is served as dispersion agent with 0.05% GNPs, while the lowest increase is 17% with hybrid dispersion agents with 0.1% GNPs. Overall, the M25 GNPs are observed to be more effective than C300 GNPs in improving the compressive strength of the GNP-reinforced mortar. Note that surfactants can be absorbed on the surface of the GNPs, repelling the GNPs by surrounding the particles with negative charges [149]. Thus, particles with larger surface area might need more surfactants to achieve uniform dispersion. Comparing with M25, the same amount of dispersion agent might not be sufficient for C300 with larger surface area. Besides, the GNPs can retard the crack propagation, transferring the crack tip stress to redistribute the stress. The opening cracks will be bridged and pinned by GNPs until it has been pulled out. These effects are stronger when the GNPs has a larger lateral size [126], which can also result in less improvement with C300 GNPs which has considerably smaller sheet size.

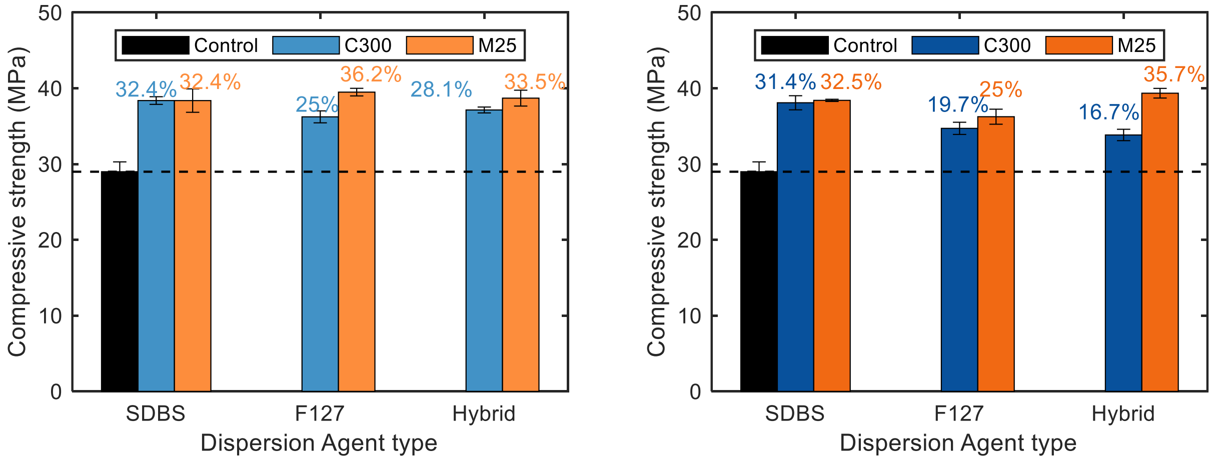

(a) (b)

**Figure 6-1.** Compressive strength of GNPs reinforced mortar with different dispersion agents at (a) 0.05%; (b) 0.1% GNPs.

### *6.5.2. Thermogravimetric Analysis (TGA)*

The Thermogravimetric (TG) curve and first derivative of TG (DTG) curve of all specimens are plotted in Figure 6-2. The peaks in DTG curves indicates the weight loss of different hydration products due to the thermal decomposition. In particular, the peaks represent the decomposition of C-S-H and ettringites, calcium hydroxide, and $CaCO_3$. The number and position of peaks do not change much with the incorporation of GNPs, indicating that GNPs did not significantly affect the hydration process.

The CH content and hydration degree are calculated based on the information of TG and DTG curves and listed in Table 6-3. The CH content and hydration degree is slightly decreased in most of the specimens with the GNP C300, except the specimen with Hybrid surfactants. This could be attributed to the flocculation of the GNPs that absorb and trap the surrounding water, resulting in less water for the growth of C-S-H [167,180]. The cement particle might be surrounded by GNPs particles, leading to the limitation of hydration reaction [181].

Nevertheless, the nucleation effect of GNPs can offset the decrease in hydration products. So, the CH content and hydration degree are improved in most specimens with M25 GNPs, implying that M25 has stronger nucleation effects than C300. There is no clear trend of CH content and hydration degree with increasing concentration of GNPs. A higher GNP concentration means more particles, higher chance of flocculation and less free water for hydration reaction, which has negative effect on CH content and hydration degree. On the other hand, higher concentration also means larger surface area and more nucleation site for growth of hydration products, which has the positive effect. These two effects offset. For both types of GNPs, the specimen prepared with Hybrid surfactants shows the highest CH content and hydration degree, suggesting that Hybrid surfactants work better in the hydration process.

In general, the improvements in CH content and hydration degree compared to the control specimen are not considerable for M25 GNPs. These results suggest the nano-filler effect and crack pinning and bridging effects of GNPs might have more important role than its nucleation effect.

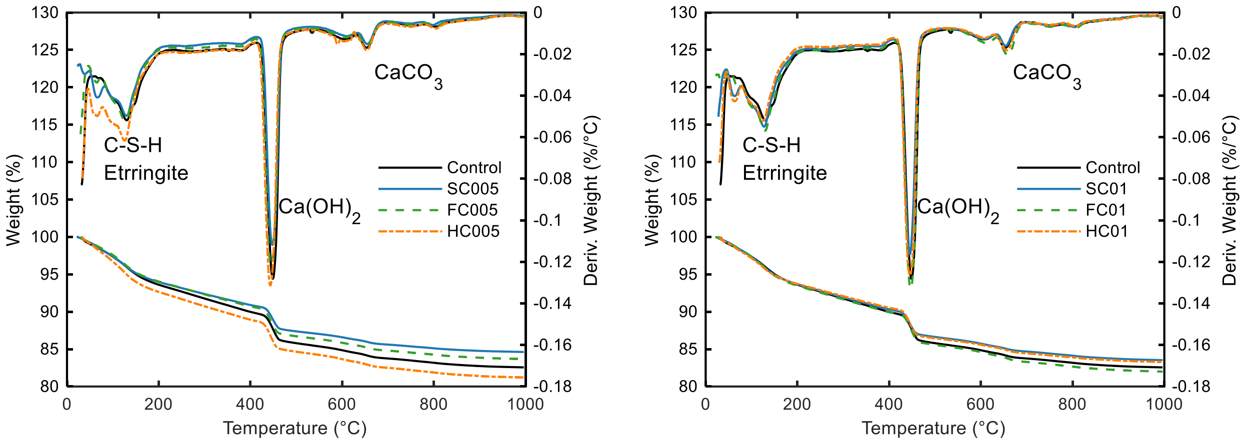

(a)

(b)

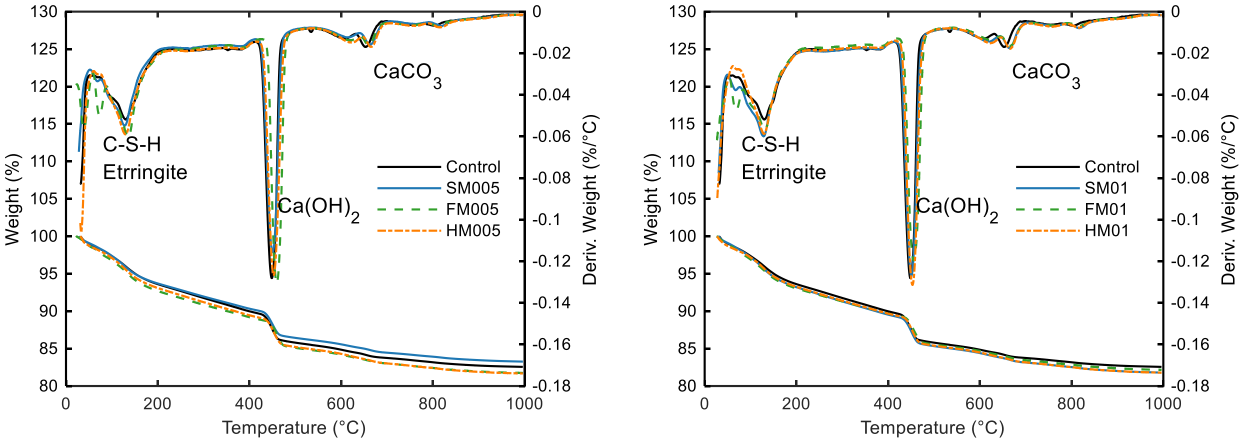

(c) (d)

**Figure 6-2.** TG and DTG curves of GNPs reinforced mortar of different dispersion agents with (a) 0.05% C300; (b) 0.1% C300; (c) 0.05% M25; and (d) 0.1% M25.

**Table 6-3.** Hydration degree and CH content

| **Specimens** | **Hydration degree (%)** | | **CH content (%)** | |
|---|---|---|---|---|
| | **0.05% GNPs** | **0.1% GNPs** | **0.05% GNPs** | **0.1% GNPs** |
| Control | 51.99 | | 14.57 | |
| SDBS-C | 47.91 | 48.52 | 13.13 | 13.83 |
| F127-C | 49.01 | 53.07 | 14.16 | 13.91 |
| Hybrid-C | 54.46 | 48.64 | 15.77 | 15.56 |
| SDBS-M | 49.71 | 54.12 | 14.61 | 15.97 |
| F127-M | 53.31 | 52.00 | 14.94 | 15.73 |
| Hybrid-M | 54.36 | 54.11 | 15.97 | 16.55 |

### 6.5.3. *Permeable Porosity*

The permeable pore content is presented in Figure 6-3. A noticeable reduction in permeable porosity can be observed, which can be mainly attributed to the refinement of pore diameter and enhancement of compactness of cementitious composite [141]. Impermeable GNPs particles can fill into pores to decrease the permeable porosity. The nucleation effect of GNPs can promote cement hydration, leading to a more homogenous microstructure.

For both types of GNPs, the increase in concentration lightly increases the permeable porosity. This might be due to the more dosage of surfactants used. The use of surfactants induces the increase in entrapped air in matrix. In specimens with the C300 GNPs, the one prepared with SDBS exhibits the largest enhancement, while the one with F127 shows the least improvement. Note that specimens with the C300 GNPs shows slightly less CH content and hydration degree in TGA results, which indicating that the nano-filling effects governs in here. With the relatively low density, the volume of the C300 GNPs is larger than the M25 GNPs. Thus, the C300 GNPs can fill in more voids and decrease the porosity. As for the M25 GNPs, the specimens prepared with Hybrid surfactants presents the lowest porosity. This can be attribute to the nucleation effect as the highest hydration degree and CH content shown in TGA results. It seems that SDBS well-disperse the GNPs in matrix, followed by the Hybrid and F127.

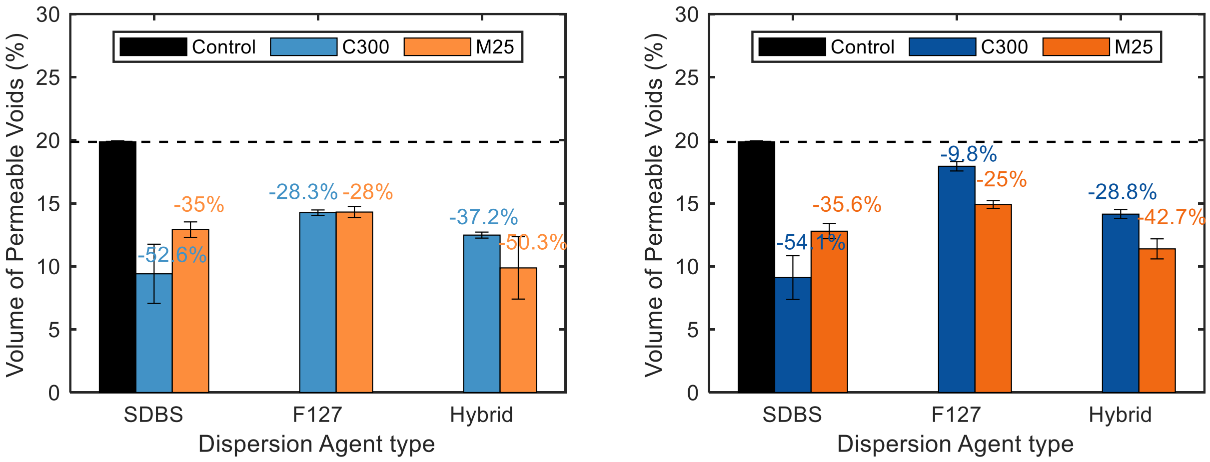

(a) (b)

**Figure 6-3.** Permeable voids of GNPs reinforced mortar with different dispersion agents at (a) 0.05%; (b) 0.1% GNPs.

### 6.5.4. *Sorptivity*

Figure 6-4 shows the sorptivity results of GNP-cementitious composites fabricated with different dispersion agents. It is obvious that addition of GNP reduces the sorptivity. The sorptivity is directly proportional to the volume of capillary pore in specimens [182]. As discussed above, GNPs somewhat accelerate the cement hydration process and densify the microstructure of mixtures. The transportation properties of cementitious composites is also greatly influenced by critical pore size [183]. GNPs can fill in the pores and divide the coarse pores into finer pores, decreasing the critical pore size and also the sorptivity [117,126]. Besides, the impermeable GNPs filling in the pores inside will form extensive barriers, which will create more tortuous path for the ingress of water [117,149].

Comparing with M25 GNPs, C300 GNPs have more improvement in sorptivity. This might be attributed to the better nano-filling effect of C300 GNPs. There is no clear trend in the change of sorptivity with increasing dosage of GNPs. As discussed above, the permeable porosity is slightly decrease with more GNPs. However, more tortuous path will be created with the incorporation of more GNPs particles. These two opposite effects offset.

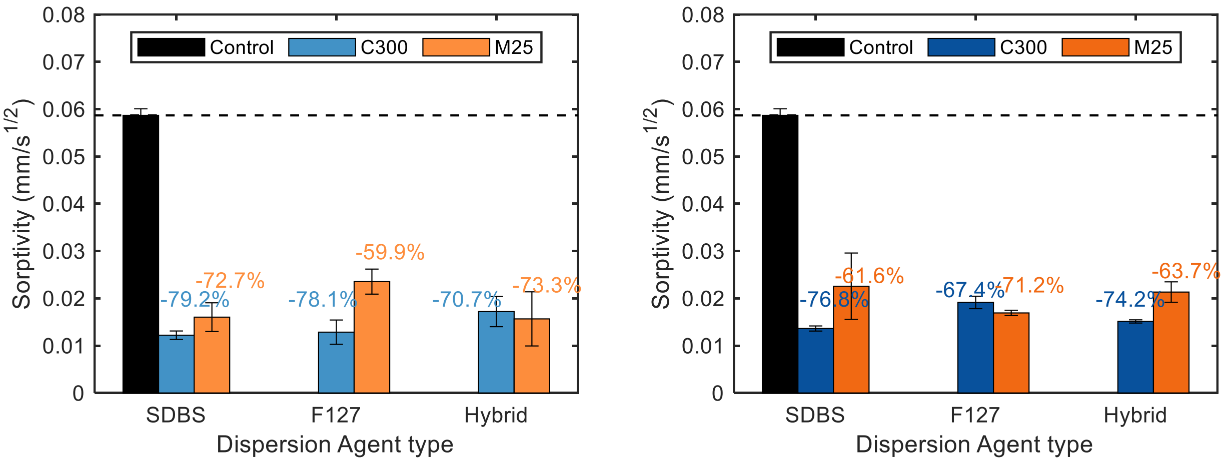

(a) (b)

**Figure 6-4.** Sorptivity of GNPs reinforced mortar with different dispersion agents at (a) 0.05%; (b) 0.1% GNPs.

### *6.5.5. Scanning Electron Microscopy (SEM)*

The microstructure of 0.05% GNP-reinforced mortar is further investigated by the SEM images in Figure 6-5 to 6-7. In SEM images, the regular and compact structure is mainly C-S-H phase. Ettringite is needle-like crystals, and $Ca(OH)_2$ crystals are plate-like crystals [184]. The disorderly needle-like ettringite and plate-like calcium hydroxide can be observed in control specimen. With the addition of GNPs, the needle-like crystals are hardly seen in the SEM images. The structure of GNP-reinforce mortar looks more compact. Though the CH content and hydration degree is not considerably enhanced, the calcium hydroxide crystal density is increased, and the structure is refined. This could be attributed to the nucleation effect. GNPs provide the nucleation site for the growth of C-S-H on its surface. A few CH crystals disperse in these C-S-H, forming a compact core-shell element. These core-shell elements distribute in the hydration products, leading to a refine and compact structure [126]. Due to the low concentration and small diameter of the C300 GNPs, it is hard to distinguish GNPs particles in the SEM images. But in other word, there is no GNP agglomerations shown in images. As shown in Figure 6-7 (a), GNPs are pinned in the crystals, indicating the bridge effect of GNPs.

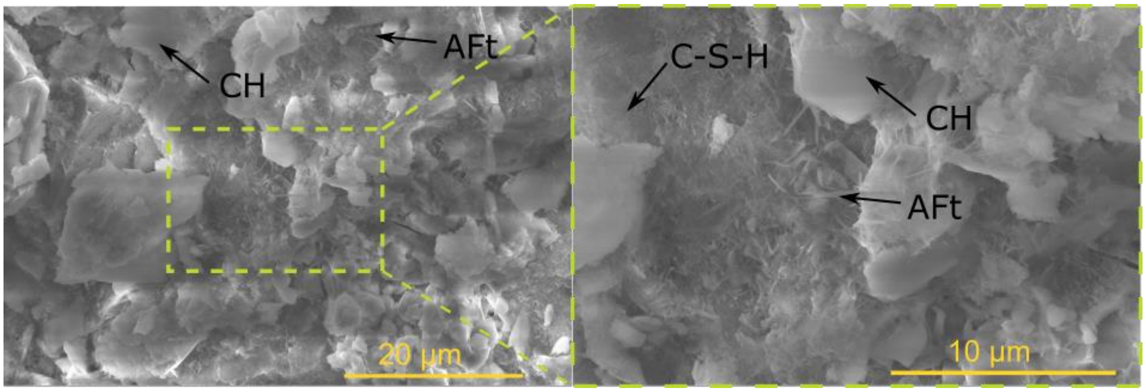

**Figure 6-5.** SEM of Control specimen

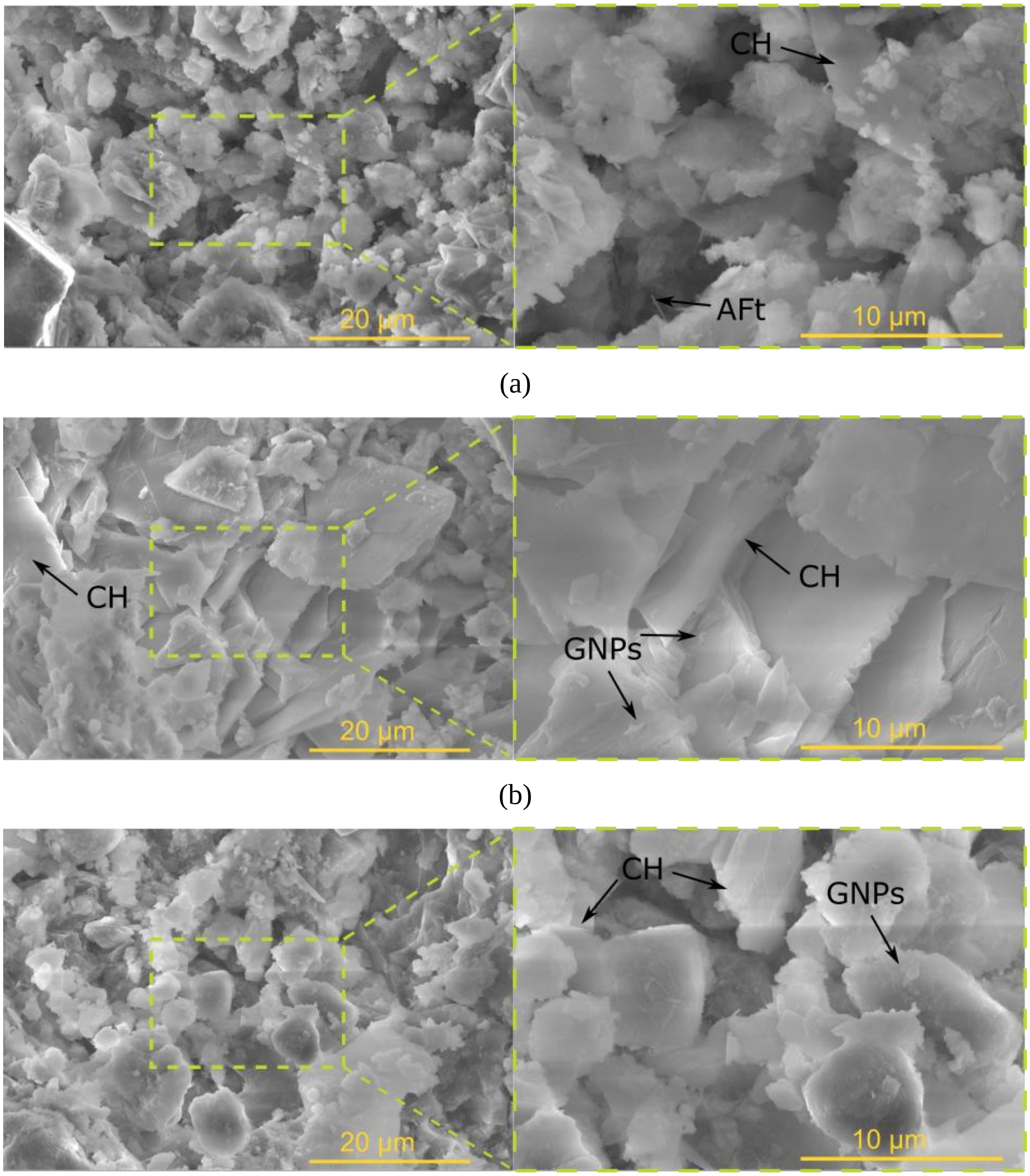

(a)

(b)

(c)

**Figure 6-6.** SEM of specimens with GNP C300 prepared with (a) SDBS; (b) F127; and (c) Hybrid.

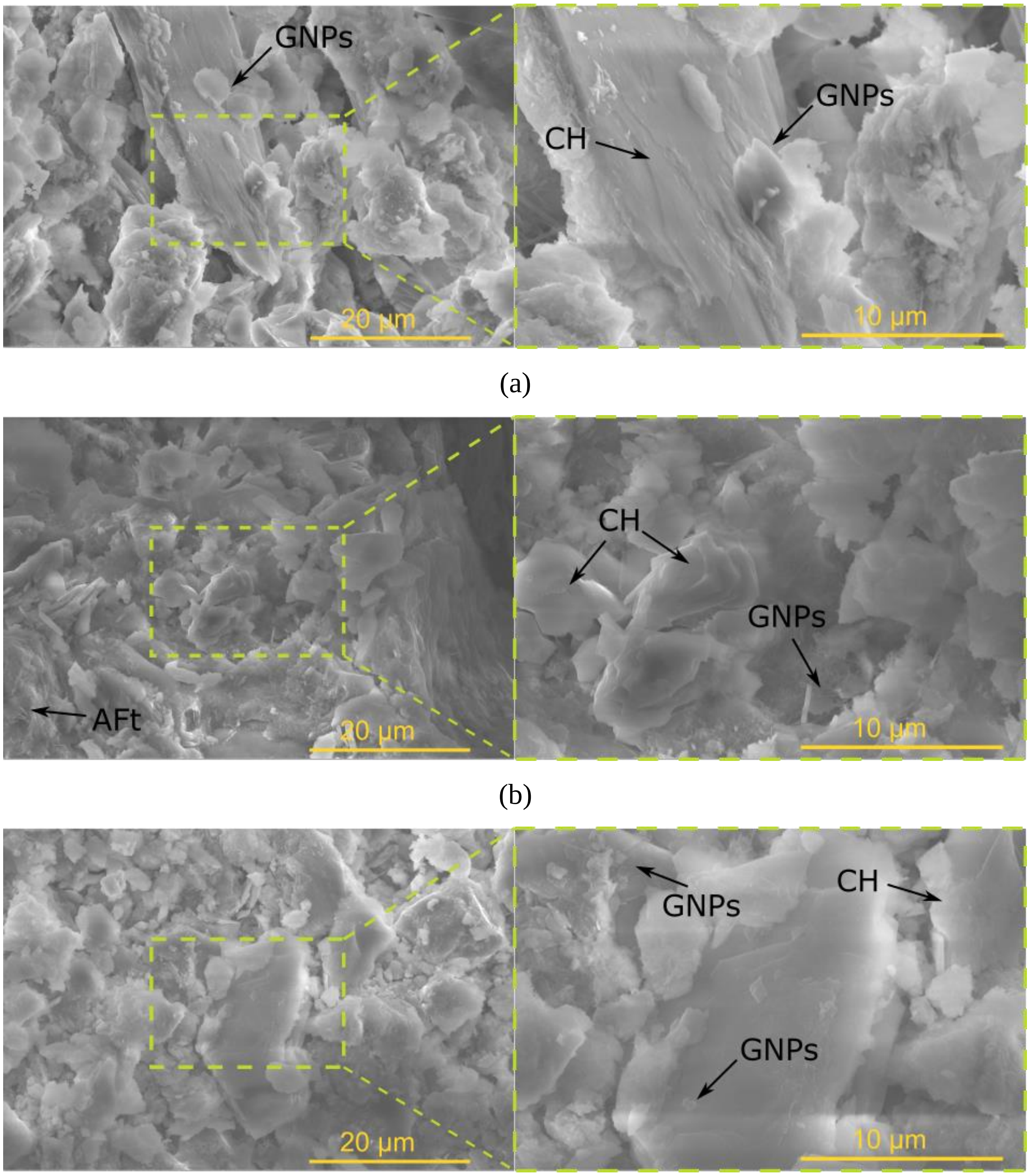

(a)

(b)

(c)

**Figure 6-7.** SEM of specimens with GNP M25 prepared with (a) SDBS; (b) F127; and (c) Hybrid.

Based on the results discussed above, the reinforcing mechanism of GNPs on cementitious composites is illustrated in Figure 6-8. During the hydration process, GNPs with large surface area can provide a nucleation site where C-S-H precipitate and grow, leading to a denser structure. The nucleation effect of GNPs will not only promote the hydration reaction, but also refine the structure of crystals. GNPs particles can fill into pores and divide coarse pores into fine pores, decreasing both the porosity and the critical pore size. The nano-filling effect of impermeable GNPs also increase the tortuosity of path for water or other chemicals, influencing the transport properties of cementitious composites. GNPs play the bridging effect when the cracks tend to propagate, preventing the formation of cracks. GNPs will delay the cracks until it has been pulled out.

C300 GNPs has a relatively larger surface area and a smaller particle size. If it is well-dispersed, it will have more particles compared to the M25 GNPs. From the results above, it can be seen that C300 GNPs are more difficult to be well-dispersed than the M25 GNPs. This could be due to the larger surface area which requires more surfactant. The nano-filling effect plays a key role in the reinforcement of C300 GNPs as more particles can fill into the pores. The C300 GNPs with larger surface area absorb the free water onto surface and might surround the unhydrated cement, reducing the amount of hydration products. Thus, the nucleation effect is offset. As for the M25 GNPs, the nucleation effect and bridge effect are dominant. This could be ascribed to the large diameter of the M25 GNPs.

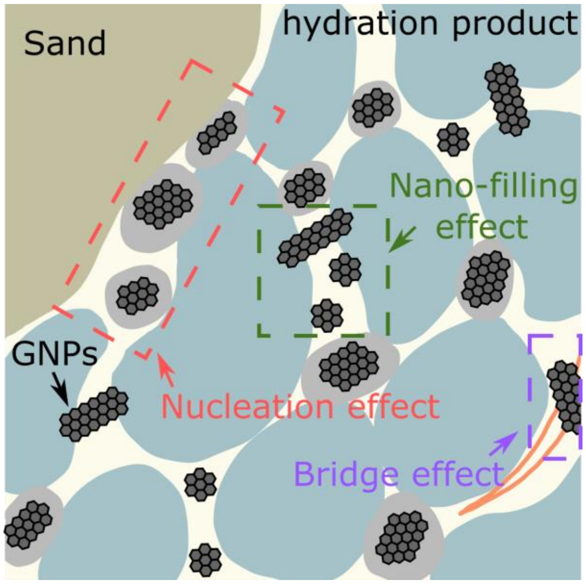

**Figure 6-8.** Schematic presentation of GNPs reinforcement in cementitious composites.

## 6. 6. Summary

This chapter explored the effect of different GNP types and different dispersion agents on mechanical properties, durability and microstructure of mortar specimens. The M-25 and C-300 GNPs with different lateral size (25 μm and <2 μm) and specific surface area (120 $m^2$/g and 300 $m^2$/g) are dispersed with SDBS, Pluronic F127 and hybrid of two surfactants. The compressive strength test is conducted to study mechanical properties of the fabricated GNP-cement composites, while the sorptivity and permeable porosity tests are conducted to evaluate their durability characteristics. In addition, thermogravimetric analysis is conducted to examine the effects of GNP addition to hydration process. SEM images are obtained to evaluate the microstructure of GNP-reinforced cementitious composites. Based on the findings, the following conclusions can be made:

- The compressive strength is significantly improved with the addition of GNPs. Further increasing the concentration of GNPs reduce the enhancement of compressive strength, which could be attributed to the insufficient dispersion and the use of high dosage of surfactants.
- The CH content and hydration degree are promoted with the addition of M25 GNPs, while they are slightly decreased with C300 GNPs. This could be due to the poor absorption of free water and limitation of surrounded unhydrated cement, which offset the nucleation effect.
- The sorptivity and permeable porosity is remarkably improved.
- The type of surfactants will not influence the dispersion results when they are sufficient for dispersing the GNPs. However, SDBS has a better dispersion when they are not sufficient.
- The nano-filling effect plays a key role in reinforcement of C300 GNPs, while nucleation effect and bridge effect are dominant for M25 GNPs.

# 7. LIFE CYCLE IMPACT AND COST OF GRAPHENE-CEMENT COMPOSITES

## 7. 1. Overview

Concrete is most widely used material in built environment with the advantages of ease of casting into shape and low cost. However, concrete production causes significant global carbon dioxide emissions, leading to various environmental and social impacts. This study explores the environment impact of GNP-reinforced mortar by means of Life Cycle Impact Assessment (LCIA) and Life Cycle Cost Analysis (LCCA). The system boundary of this study is selected to be “cradle to gate”, i.e., from the extraction of raw materials up to construction site of GNP reinforced mortar. The analyses shows that the production of 1 $m^3$ mortar normalized to compressive strength reduce the environment impact by 25% with addition of GNPs. The $CO_2$ emission of 0.05% GNPs, which is only 0.047 kg $CO_2$ eq, is neglectable comparing with cement. The sensitivity analysis shows that cement is the most sensitive ingredient from the environmental perspective. The addition of GNPs in cementitious composites can reduce the environment impact of cement-based composites by improving their mechanical properties and reducing the amount of cement used.

## 7. 2. Goal and Scope

The goal of this study is to evaluate the environmental impacts of GNP-reinforced concrete materials by means of a Life Cycle Assessment (LCA). In particular, three GNP-reinforced mortar composites with the addition of GNPs at 0%, 0.05 and 0.1% are evaluated. For the dispersion of GNPs, the hybrid use of SDBS and Pluronic F-127 is considered based on the findings of studies discussed in Chapters 5 and 6. The detailed mix design is presented in Table 7-1.

**Table 7-1.** Mix design and compressive strength of Control, GNP005 and GNP01 mortar

| **Materials** | **Unit** | **Mixtures** | | |
|---|---|---|---|---|
| | | **Control** | **GNP005** | **GNP01** |
| Cement | kg | 504.22 | 503.39 | 503.09 |
| Sand | kg | 1386.59 | 1384.31 | 1383.5 |
| Water | kg | 307.1 | 306.51 | 306.33 |
| GNP | kg | -- | 0.25 | 0.5 |
| SDBS | kg | -- | | 0.5 |
| F127 | kg | -- | 0.50 | 0.5 |
| SP | kg | 10.08 | 10.07 | 10.06 |
| TBP | kg | -- | 1.01 | 1.01 |
| Compressive Strength | MPa | 28.98 | 39.49 | 39.35 |

## 7. 3. Functional Unit and System Boundary

The functional unit is selected as 1 $m^3$ of GNP reinforced mortar. The environmental assessment of this functional unit is normalized to the compressive strength.

The system boundary of this study is from “cradle to gate”, i.e., from the extraction of raw materials up to construction site of GNP reinforce mortar, as shown in Figure 7-1. The production and use of mixer is excluded as it is used in all cases. So, it has the same impacts on environment and can be eliminated from the system. The use phase and the end-of-life demolition are not included.

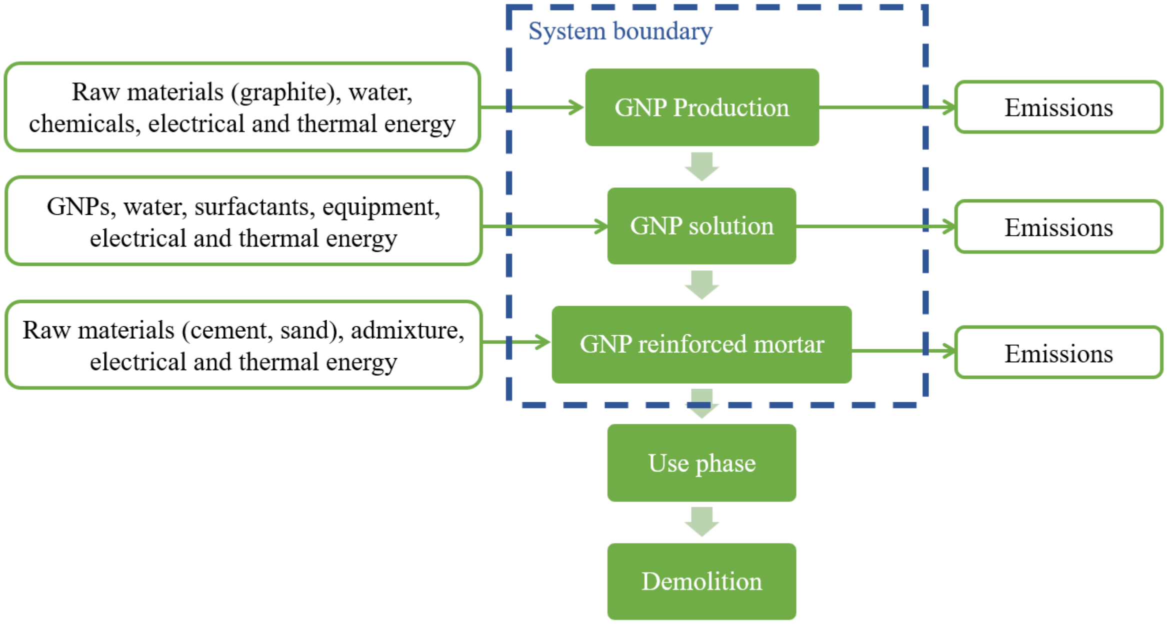

**Figure 7-1.** System boundary.

## 7. 4. Data Collection

In this study, the data is primarily obtained from scientific literature and Ecoinvent 3.0. Due to the lack of data from the manufacturer, the following assumptions have been made:

- GNPs are produced by liquid exfoliation method from graphite and chemical agent. The life cycle inventory (LCI) of materials, emission and energy consumption of GNP production is based on the experimental results of liquid exfoliation of graphene study by the author.
- The material composition of high shear mixer and ultrasonicator is assumed to be the same as the construction robot [185] and proportional by weight. The service life of high shear mixer and ultrasonicator is 10 years, with an assuming running time of 45000 h.
- The LCI of superplasticizer is obtained from scientific literature [186].
- The production of Pluronic F127 and TBP is not available in Ecoinvent database. Thus, the ratio of each ingredient to synthesize the product is applied to estimate the LCI [187].

### *7.4.1. GNP production*

Graphite powders and exfoliating liquid which consists of water and chemicals are mixed by a high shear mixer. The shear mixing process is maintained at 5000 rpm for 2 hours. After shear mixing, the suspension is simply poured into another beaker to discard the unexfoliated graphite. The detail of graphite powders and exfoliating liquid is presented in Table 7-2.

**Table 7-2.** Summary of input materials and final concentrations

| Input materials | | | Output product |
|---|---|---|---|
| **Graphite (kg)** | **Chemicals (kg)** | **Deionized water (kg)** | **GNPs (kg)** |
| 1 | 0.2 | 25 | 0.16 |

The production rate is around 16%. The unexfoliated graphite and the sodium cholate can be used to produce GNPs. Thus, to exfoliate 1 kg GNPs, 6.25 cycles of exfoliation process is needed, i.e., 12.5 hours of operation.

The high shear mixer is electrically powered by lithium-ion batteries with a capacity of 0.5 kWh. So, the energy consumption during the process is:

$$E = 0.5 \times 12.5 = 6.25\ kWh$$

The service life of higher shear mixer is 45000 h. The unit of high shear mixer for the process is:

$$U_{HSM} = \frac{12.5}{45000} = 2.78 \times 10^{-4}$$

The detailed life cycle inventory of GNPs production is listed in Table 7-3.

**Table 7-3.** Life cycle inventory of GNPs (1 kg)

| Flow | Unit | Amount |
|---|---|---|
| Graphite, at plant | kg | 1 |
| Chemicals | kg | 0.25 |
| Water, deionized, at plant | kg | 25 |
| High shear mixer | Item | $2.78 \times 10^{-4}$ |
| Electricity, medium voltage, at grid | kWh | 6.25 |

### *7.4.2. GNP-reinforced Mortar*

To fabricate 1 $m^3$ GNP-reinforced mortar, GNPs are first dispersed into water with the aid of surfactant by ultrasonicator for 1 h. The ultrasonicator is electrically powered by lithium-ion batteries with a capacity of 0.75 kWh. So, the energy consumption during the process is:

$$E = 0.75 \times 1 = 0.75\ kWh$$

The service life of higher shear mixer is 45000 h. The unit of high shear mixer for the process is:

$$U_{HSM} = \frac{1}{45000} = 2.72 \times 10^{-5}$$

The life cycle inventory of Control, GNP005 and GNP01 is presented in Table 7-4, 7-5 and 7-6, respectively.

**Table 7-4.** Life cycle inventory of Control mortar (1 $m^3$)

| Flow | Unit | Amount |
|---|---|---|
| Portland cement, strength class Z 42.5, at plant | kg | 504.22 |
| Silica sand, at plant | kg | 1386.59 |
| Superplasticizer | kg | 10.08 |
| Tap water, at user | kg | 307.01 |

**Table 7-5.** Life cycle inventory of GNP005 mortar (1 $m^3$)

| Flow | Unit | Amount |
|---|---|---|
| Portland cement, strength class Z 42.5, at plant | kg | 503.39 |
| Silica sand, at plant | kg | 1384.31 |
| Superplasticizer | kg | 10.07 |
| Tap water, at user | kg | 306.5 |
| GNPs | kg | 0.25 |
| Pluronic F127 | kg | 0.50 |
| TBP | kg | 1.01 |
| Ultrasonicator | Item | $2.72 \times 10^{-5}$ |

| | | |
|---|---|---|
| Electricity, medium voltage, at grid | kWh | 0.75 |

**Table 7-6.** Life cycle inventory of GNP01 mortar (1 $m^3$)

| Flow | Unit | Amount |
|---|---|---|
| Portland cement, strength class Z 42.5, at plant | kg | 503.09 |
| Silica sand, at plant | kg | 1383.50 |
| Superplasticizer | kg | 10.06 |
| Tap water, at user | kg | 306.33 |
| GNPs | kg | 0.50 |
| Pluronic F127 | kg | 0.50 |
| Alkylbenzene sulfonate, linear, petrochemical, at plant | kg | 0.50 |
| TBP | kg | 1.01 |
| Ultrasonicator | Item | $2.72 \times 10^{-5}$ |
| Electricity, medium voltage, at grid | kWh | 0.75 |

### *7.4.3. Cost*

The unit price of each ingredient is listed in Table 7-7.

**Table 7-7.** Unit price of ingredient

| Materials | Unit | Price |
|---|---|---|
| Portland cement | $/ton | 125 |
| Silica sand | $/ton | 100 |
| Superplasticizer | $/kg | 0.55 |
| Water | $/ton | 0.4 |
| GNPs | $/kg | 65 |
| Pluronic F127 | $/kg | 2.75 |
| SDBS | $/kg | 1 |
| TBP | $/kg | 1.56 |
| Ultrasonicator | $/item | 5113 |
| Electricity, medium voltage, at grid | $/kWh | 0.1375 |

## 7. 5. Life Cycle Impact Assessment (LCIA) Method

The LCIA is performed on the software openLCA. The method ReCipe Midpoint (H), which is commonly used in studying the impact of concrete, is used. The ReCipe Midpoint (H) evaluates the balance between short-term and long-term damaging effects, with an advantage of a lower uncertainty in environmental evaluations [188]. Comparing with other methods, ReCipe Midpoint contains more human related categories and also fine particle category, which are important in concrete production. Table 7-8 listed the selected Recipe Midpoint impact categories.

**Table 7-8.** Selected Recipe Midpoint impact categories

| Impact category | Reference unit |
|---|---|
| Global warming | kg $CO_2$ eq |
| Ozone formation | kg $NO_x$ eq |
| Human toxicity | kg 1,4-DCB |
| Terrestrial acidification | kg $SO_2$ eq |
| Terrestrial ecotoxicity | kg 1,4-DCB |
| Fine particulate matter formation | kg PM2.5 eq |
| Fossil resource scarcity | kg oil eq |
| Freshwater ecotoxicity | kg 1,4-DCB |
| Freshwater eutrophication | kg P eq |

## 7. 6. LCIA and Interpretation

### *7.6.1. GNP Production*

Figure 7-2 graphically depicts the relative contribution of raw materials, equipment and electricity use to the overall environment impact of synthesize 1 kg GNPs. It is apparent that the greatest effect comes from the electricity consumption during the exfoliation process. This could be attributed to the relative low production rate, which requires more cycles of exfoliation process and high electricity consumption. Although the relative impact of chemicals is the second highest, it remains low comparing with the one of electricity consumption. Chemicals are used to keep the exfoliated graphene sheets stable in solution, preventing the re-agglomeration

[121,189]. Thus, more GNPs can be synthesized during the process. The fabrication of high shear mixer is comparatively low in all indicators except the freshwater ecotoxicity, which might be due to the use of lithium batteries. The relative impact of water is negligible.

The environment impact of GNPs production can be reduced by decreasing the electricity consumption. Note that, the high shear mixer used in this study is a lab-scale equipment. In industry manufacturing, the equipment with high efficiency will be used, improving the production rate and reducing the electricity use. Besides, more chemicals can be utilized to enhance the productivity. In other word, more factors with low environment impacts can be used to reduce the electricity consumption. In addition, renewable energy, such as solar and wind, can be used to generate the required electricity [190].

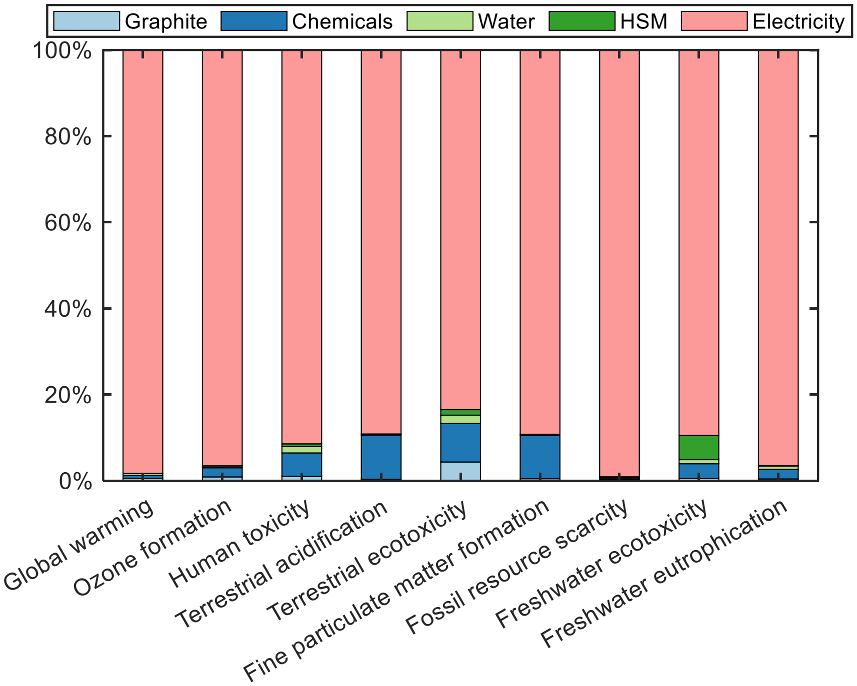

**Figure 7-2.** Relative contribution to the total environment impact of production of 1 kg of GNPs.

### *7.6.2. GNP-reinforced Mortar*

The life cycle cost analysis result is presented in Figure 7-3. It can be seen that the greatest cost comes from the sand, followed by cement and GNPs. Although the unit price of GNPs is tremendously higher than the one of cement and sand, the total price drops off due to the low dosage used in the mixture. Besides, with the addition of low dosage of GNPs, the compressive strength is improved by approximately 35%. Thus, the cost of fabricating 1 $m^3$ GNP005 and GNP01 mortar can reduce the cost by 19.8% and 13.6%, respectively.

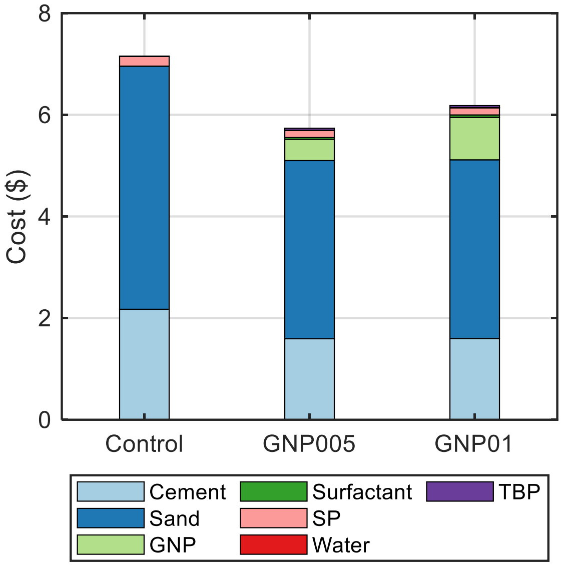

**Figure 7-3.** Cost of $1m^3$ Control, GNP005 and GNP01 normalized to compressive strength.

Figure 7-4 compares the normalized Recipe Midpoint indicator of three mixtures. It can be seen that GNP005 and GNP01 significantly reduce the environment impact by approximately 25% except the indicator of freshwater eutrophication. This means that GNPs can improving the environment impact of concrete materials by pronounced enhancement in compressive strength, though GNPs are served as additions rather than as replacements. GNP005 is 99.82% in freshwater eutrophication, while GNP01 is 102. 68%. This should be mainly attributed to the use of TBP and surfactants. GNP005 and GNP01 produce the similar compressive strength. But more surfactants are needed in GNP01 as more GNPs are used in this mixture, which also appears in the rest indicators. Comparing with GNP005, GNP01 results in a slightly higher environment impact, which should be due to the more GNPs and surfactants used in the mixture.

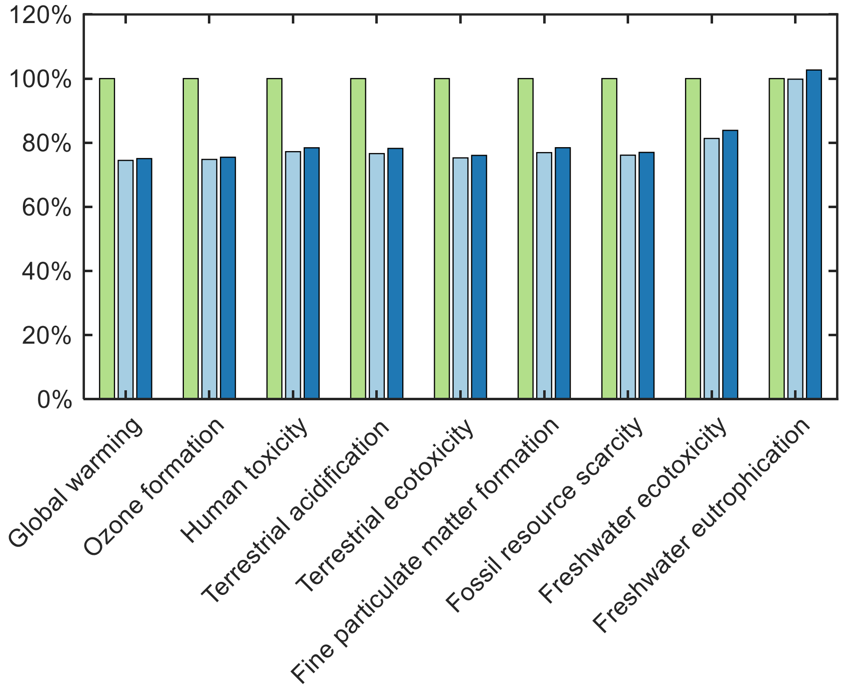

**Figure 7-4.** Comparison of environmental impacts of 1m$^3$ Control, GNP005 and GNP01 normalized to compressive strength.

Figure 7-5 presents the results of comparation of Global Warming Potential (GWP) associated with three different mixtures with the relative contribution of ingredients in mixtures. The electricity consumption and the use of ultrasonication for GNPs dispersion are included in the ingredient GNP. The $CO_2$ emission is reduced by 25.5% and 25% with the addition of 0.05% and 0.1% GNPs. As discussed above, this should be attributed to the enhancement in compressive strength. It is evident that cement is the major source of $CO_2$ emission, followed by sand in all mixtures. The $CO_2$ emission of GNPs, which is only 0.047 kg $CO_2$ eq and 0.079 kg $CO_2$ eq for GNP005 and GNP01, are neglectable comparing with other ingredients. Comparing with other admixture, superplasticizer produces a relative high $CO_2$ emission, which should be due to the higher dosage of superplasticizer applied.

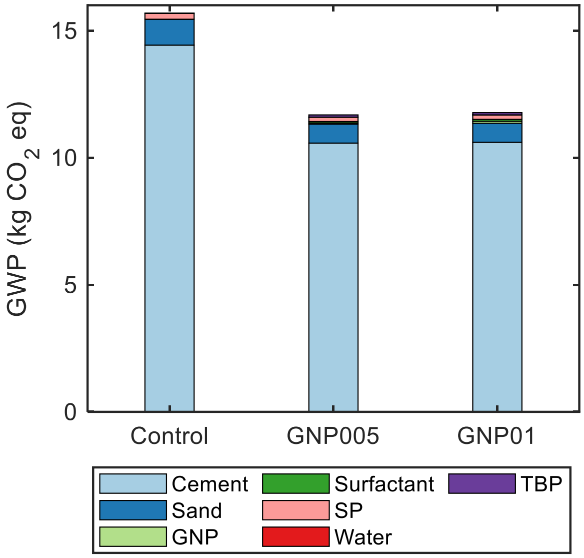

**Figure 7-5.** Relative contribution of ingredients in mixtures to climate change impact.

To evaluate the variability of $CO_2$ emission depending on different types of ingredients, the sensitivity analysis is processed by ± 10% of mass of each ingredient. The results of three different mixtures are shown in Figure 7-6. Cement is obviously the most sensitive ingredient due to the large amount of usage, following by sand, SP. Recall that, the results of 1 $m^3$ mixture is normalized with the compressive strength. This means that with the similar mixture design, the higher compressive strength leads to lower environment impact. The addition of GNPs with remarkably improvement in compressive strength can help to decrease the amount of cement in the mixture. Thus, the environment impact can be reduced. Despite of GNPs, superplasticizer is commonly used to increase the workability and reduce the water-to-cement ratio, leading to an improved strength with same amount of cement. This can also reduce the environment impact. Silica fume and fly ash, which is considered as industrial wastes with low environment impact, can also be used to partially replace the cement.

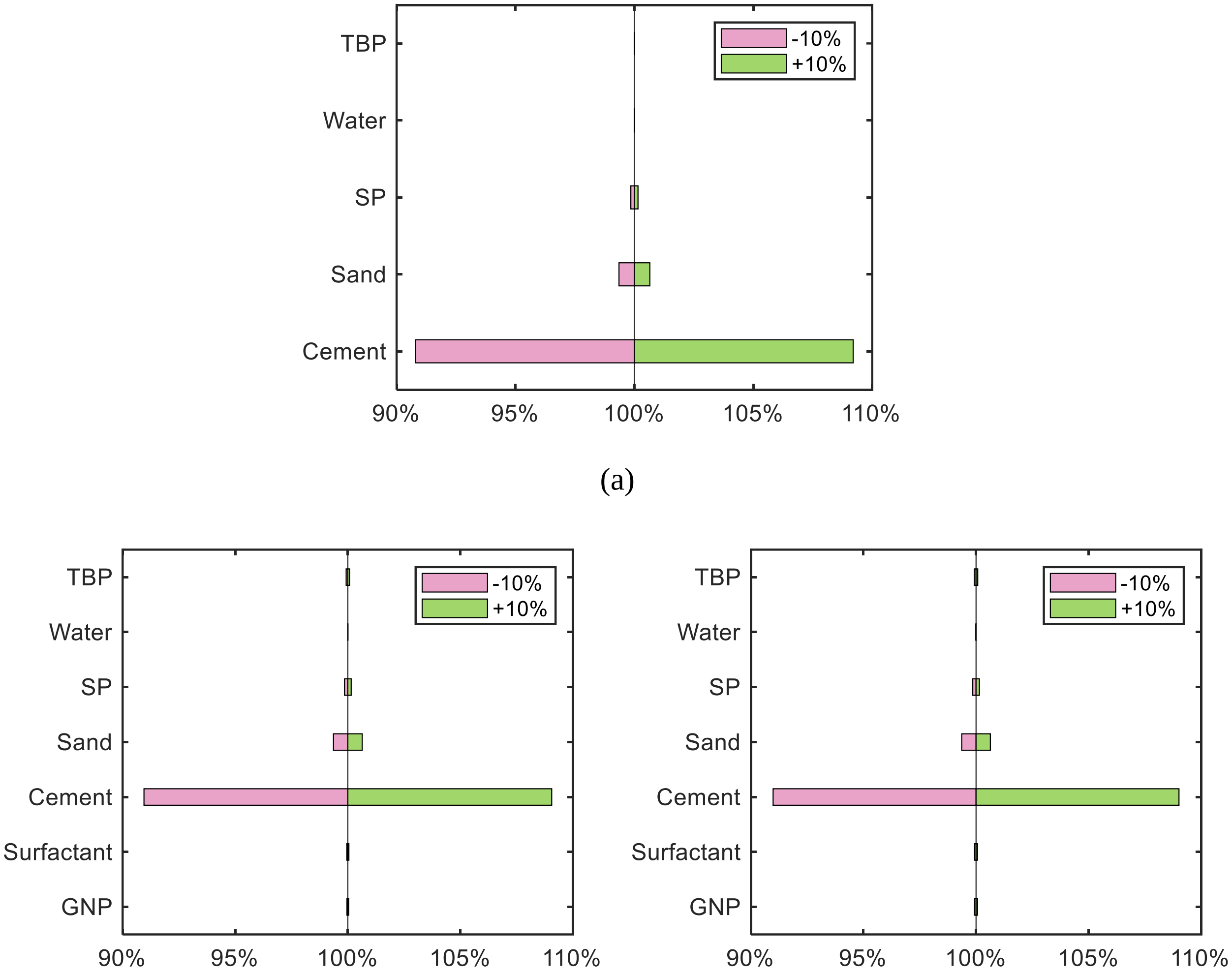

(a)

(b)

(c)

**Figure 7-6.** Senstitivity analysis of 1m$^3$ (a) Control; (b) GNP005; and (c) GNP01.

## 7. 7. Summary

In this study, the environmental impact of the lab-scale production of GNPs and three cases of GNP-reinforced mortar is evaluated by means of Life Cycle Impact Assessment (LCIA) and Life Cycle Cost Analysis (LCCA). The functional unit is 1 m$^3$ mortar normalized to the compressive strength. The system boundary is from “cradle to gate”. The following findings can be concluded:

- The greatest effect of environmental impact of lab-scale GNPs production comes from the electricity consumption. This could be attributed to the low production rate. The environment impact can be reduced by using chemicals and suitable equipment to increase the productivity and using renewable energy.
- The cost of GNP-reinforced mortar is lower than the control specimen, indicating that the addition of GNPs will not increase the cost.
- The addition of GNPs can reduce the environment impact of cementitious composites by 25%.
- The $CO_2$ emission is reduced by 25.5% and 25% with the addition of 0.05% and 0.1% GNPs. Cement is the major source of $CO_2$ emission in cementitious composites. The $CO_2$ emission of GNPs, which is only 0.047 kg $CO_2$ eq and 0.079 kg $CO_2$ eq for GNP005 and GNP01, are neglectable comparing with other ingredients, especially cement.
- The sensitivity analysis shows that cement is most sensitive ingredient. Thus, the use of GNP and supplementary cementitious materials with low environment impact should be used to either increase the mechanical properties or partially replace the cement.
- GNPs can improve both mechanical properties and transport properties of cementitious composites. Thus, the service life of cementitious composites will be extended, further reducing the environment impact.

# 8. CONCLUSIONS

## 8. 1. Summary

Graphene and its derivatives possess the unique potential to make concrete materials stronger and greener. As 2D nanomaterials with remarkable properties, they offer considerable enhancement in mechanical and transport properties and can enable functional properties when they are used as nano fillers in cement composites. Although graphene oxide (GO) has been more commonly studied in cement composites, as they have better dispersibility in water, the oxidization process introduces structural defects to graphene. Therefore, pristine graphene, rather than GO, shows more promise for the development of advanced cementitious materials and structures with high mechanical properties and durability. However, there are several challenges for the incorporation of graphene into cement matrices. The efficient dispersion of graphene within cement matrices is challenging, as the high surface energy and hydrophobic nature of graphene gives it a tendency to agglomerate in aqueous media.

This dissertation explores the use of graphene nanoplatelets (GNPs) in cement-based composites with an emphasis on determining optimal dispersion parameters and assessing the effects of GNPs on mechanical and durability performance.

In Chapter 3, the effects of different GNP dispersion methods on the dispersion quality and structural integrity of GNPs are studied. Then, the influences of GNP concentration and dispersion method on the mechanical properties of the concrete mixtures are investigated. The optical microscopy, Raman Spectra, and Scanning Electron Microscopy tests are used to assess the effectiveness of different dispersion methods. The compressive strength and flexural strength tests are conducted to evaluate the mechanical properties of the developed GNP-reinforced concrete composites.

In Chapter 4, the effects of the addition of GNPs on the tensile behavior of cementitious composites through direct tensile testing and use of AE monitoring are investigated. The mortar composites with GNP concentration levels of 0, 0.1, 0.2, 0.3, 0.4 and 0.5 wt.% of cement are prepared and tested under tension up to failure. The relation between GNPs and the microstructure and fracture modes is also explored through AE parameter analysis and Ib-value analysis.

In Chapter 5, the optimal parameters for the dispersion of GNPs are explored using TOPSIS-based and PCA-based Taguchi method. The effects of sonication parameters (time and amplitude), sample volume, surfactant type, surfactant/GNPs ratio, GNPs concentration are investigated. Seven performance criteria, which are the average particle size, the absolute value of zeta potential, UV-vis absorbency in aqueous and alkaline environments, the absolute value of zeta potential in alkaline environment, the residual absorbance after 24 h in aqueous and alkaline environments are used to characterize the dispersion quality of GNPs. The relative importance of each parameter is assessed by ANOVA.

In Chapter 6, the effects of GNP addition on the microstructure, mechanical properties, and durability of cement composites are studied. Two types of GNPs with different lateral size (<2 μm and 25 μm) and specific surface area (300 $m^2/g$ and 120 $m^2/g$) are used in this study. Two GNPs concentration of 0.05% and 0.1% by weight of the cement are used. In order to study the effect of dispersion agents, SDBS and Pluronic F127 are utilized to disperse and stabilize GNP particles in aqueous solution. Compressive strength test is conducted to assess the mechanical properties, while sorptivity test and permeable porosity test are carried out to evaluate the durability. In order to explore the effect of GNPs on hydration process and microstructure of cement mortar, thermalgravimetric analysis and SEM are conducted.

In Chapter 7, the environmental impact of the lab-scale production of GNPs and three cases of GNP-reinforced mortar by means of Life Cycle Impact Assessment (LCIA) and Life Cycle Cost Analysis (LCCA) are compared. The functional unit is selected as 1 $m^3$ mortar normalized to the compressive strength. The system boundary is set to be from cradle-to-gate.

## 8. 2. Findings and Recommendations

Major findings obtained in this research can be summarized as follows:

- For concrete composites with coarse aggregates, the effectiveness of GNPs in improving the mechanical properties is found to be limited. When the GNPs are added to the concrete mixture at a dosage of 0.025%, a maximum increase of 17% in compressive strength is observed. The compressive strength of concrete is improved at low dosages of GNPs (0.025% and 0.05%) as GNPs can eliminate the weak cement hydration crystals with tight cross-linking structures. However, higher ratios of GNPs result in a decrease in the compressive strength, which might be attributed to the weak zone in the concrete matrix created by agglomeration of GNPs. GNPs at any concentration considered in this study do not have a significant influence on the flexural strength. This could be attributed to small size and aspect ratio of graphene sheets obtained in this study after dispersion in water.

- For mortar composites, the addition of GNPs increased the tensile strength of cementitious composite. With the addition of GNPs at a concentration level of 0.1 wt.%, a maximum of 48% increase in tensile strength is achieved compared to plain mortar. The addition of GNPs improved the tensile behavior of cementitious composite by crack bridging to impede crack propagation at initial stages, and absorb energy by deforming to slow cracks, while at failure the GNPs are pulled-out.
- For the surfactant-aided sonication dispersion, the energy density, which is calculated as amplitude × time /volume, is found to be the major factor that greatly influence the dispersion of GNPs based on PCA and ANOVA results. Five different surfactants are considered for the dispersion provide similar dispersion performance. Nevertheless, the SDBS (an ionic surfactant) and Pluronic F-127 (a non-ionic surfactant) are found to be better than the other three surfactants.
- For mortar composites, the compressive strength, sorptivity, and permeable porosity are considerably improved with the addition of GNPs. In particular, a maximum of 36% increase in compressive strength is observed when the GNPs are added to the mortar composites. The hybrid use of SDBS or Pluronic F-127 for the dispersion of GNPs is provided the highest improvement. In addition, more than 50% reduction in permeable porosity is observed, which can be mainly attributed to the refinement of pore diameter and enhancement of compactness of cementitious composites. The sorptivity, which is directly proportional to the volume of capillary pores, is also reduced by 79%.

- The nano-filling effect plays a key role in reinforcement of GNPs with smaller particle size but larger surface area, while nucleation effect and bridge effect are dominant for GNPs with larger particle size.
- The addition of GNPs can significantly reduce the environment impact of cementitious composites by 25%.

The results obtained in this study indicates that graphene-based nanomaterials can enhance the mechanical and durability performance of cement-based composites, while reducing their adverse environmental impacts. However, there are still several challenges for the incorporation of graphene into cement matrices and more research is needed to implement widespread use of graphene in the construction industry. First, the mechanical properties of concrete composites, which includes coarse aggregates, are not considerably improved with the GNP addition in this study, while the GNPs considerably enhances the performance of mortar composites. Future studies are needed to develop a dispersion approach that can lead to consistent and higher improvements in mechanical properties of concrete composites. Furthermore, as the experimental work within in Chapter 6 displays, graphene's physical properties, such as thickness and surface area, have a significant effect on its reinforcing effects in cement. A more complete understanding of these factors needs to be obtained, to fabricate commercial graphene-based cementitious materials.

Another important long-term consideration is the environmental sustainability of widespread use and production of graphene-based nanomaterials. While self-sensing cementitious composites are expected to help relieve some environmental burdens in cities, through a potential reduction in the amount of concrete needed to achieve the same strength, the effects of the production and distribution of the graphene itself warrant more research. Furthermore, other sustainability impacts are still relatively unknown, such as potential human health effects. Such factors will need to be considered to ensure a sustainable and safe incorporation of graphene into civil structures.

# REFERENCES

[1] U.M. Angst, R.D. Hooton, J. Marchand, C.L. Page, R.J. Flatt, B. Elsener, C. Gehlen, J. Gulikers, Present and future durability challenges for reinforced concrete structures, Mater. Corros. 63 (2012) 1047–1051. https://doi.org/10.1002/maco.201206898.

[2] L. Barcelo, J. Kline, G. Walenta, E. Gartner, Cement and carbon emissions, Mater. Struct. Constr. 47 (2014) 1055–1065. https://doi.org/10.1617/s11527-013-0114-5.

[3] D.D.L. Chung, Electrical conduction behavior of cement-matrix composites, J. Mater. Eng. Perform. 11 (2002) 194–204. https://doi.org/10.1361/105994902770344268.

[4] D.D.L. Chung, Piezoresistive cement-based materials for strain sensing, J. Intell. Mater. Syst. Struct. 13 (2002) 599–609. https://doi.org/10.1106/104538902031861.

[5] P. Xie, P. Gu, J.J. Beaudoin, Electrical percolation phenomena in cement composites containing conductive fibres, J. Mater. Sci. 31 (1996) 4093–4097. https://doi.org/10.1007/BF00352673.

[6] R.M. Chacko, N. Banthia, A.A. Mufti, Carbon-fiber-reinforced cement-based sensors, Can. J. Civ. Eng. 34 (2007) 284–290. https://doi.org/10.1139/l06-092.

[7] F. Azhari, N. Banthia, Cement-based sensors with carbon fibers and carbon nanotubes for piezoresistive sensing, Cem. Concr. Compos. 34 (2012) 866–873. https://doi.org/10.1016/j.cemconcomp.2012.04.007.

[8] B. Han, S. Sun, S. Ding, L. Zhang, S. Dong, X. Yu, Nano carbon material--filled cementitious composites: Fabrication, properties, and application, in: Innov. Dev. Adv. Multifunct. Nanocomposites Civ. Struct. Eng., Elsevier, 2016: pp. 153–181. https://doi.org/10.1016/B978-1-78242-326-3.00008-7.

[9] R. Ranade, J. Zhang, J.P. Lynch, V.C. Li, Influence of micro-cracking on the composite resistivity of Engineered Cementitious Composites, Cem. Concr. Res. 58 (2014) 1–12. https://doi.org/10.1016/j.cemconres.2014.01.002.

[10] V.W.J. Lin, M. Li, J.P. Lynch, V.C. Li, Mechanical and electrical characterization of self-sensing carbon black ECC, Nondestruct. Charact. Compos. Mater. Aerosp. Eng. Civ. Infrastructure, Homel. Secur. 2011. 7983 (2011) 798316. https://doi.org/10.1117/12.880178.

[11] K. Gong, Z. Pan, A.H. Korayem, L. Qiu, D. Li, F. Collins, C.M. Wang, W.H. Duan, Reinforcing Effects of Graphene Oxide on Portland Cement Paste, J. Mater. Civ. Eng. 27 (2015) 1–6. https://doi.org/10.1061/(asce)mt.1943-5533.0001125.

[12] S. Chuah, Z. Pan, J.G. Sanjayan, C.M. Wang, W.H. Duan, Nano reinforced cement and concrete composites and new perspective from graphene oxide, Constr. Build. Mater. 73 (2014) 113–124. https://doi.org/10.1016/j.conbuildmat.2014.09.040.

[13] I.S.-Y. Wong, Effects of ultra-low concentrations of nanomaterials on the piezoresistivity of cementitious composites, University of California, Davis, 2015.

[14] X. Yu, E. Kwon, A carbon nanotube/cement composite with piezoresistive properties, Smart Mater. Struct. 18 (2009). https://doi.org/10.1088/0964-1726/18/5/055010.

[15] B. Han, K. Zhang, T. Burnham, E. Kwon, X. Yu, Integration and road tests of a self-sensing CNT concrete pavement system for traffic detection, Smart Mater. Struct. 22 (2013). https://doi.org/10.1088/0964-1726/22/1/015020.

[16] M.S. Konsta-Gdoutos, C.A. Aza, Self sensing carbon nanotube (CNT) and nanofiber (CNF) cementitious composites for real time damage assessment in smart structures, Cem. Concr. Compos. 53 (2014) 162–169. https://doi.org/10.1016/j.cemconcomp.2014.07.003.

[17] B. Han, K. Zhang, X. Yu, E. Kwon, J. Ou, Fabrication of Piezoresistive CNT/CNF Cementitious Composites with Superplasticizer as Dispersant, J. Mater. Civ. Eng. 24 (2012) 658–665. https://doi.org/10.1061/(ASCE)MT.1943-5533.0000435.

[18] K.J. Loh, J. Gonzalez, Cementitious composites engineered with embedded carbon nanotube thin films for enhanced sensing performance, J. Phys. Conf. Ser. 628 (2015). https://doi.org/10.1088/1742-6596/628/1/012042.

[19] I. Wong, K.J. Loh, R. Wu, N. Garg, Effects of ultra-low concentrations of carbon nanotubes on the electromechanical properties of cement paste, in: Nanotechnol. Constr., Springer, 2015: pp. 371–376.

[20] K.M. Liew, M.F. Kai, L.W. Zhang, Carbon nanotube reinforced cementitious composites: An overview, Compos. Part A Appl. Sci. Manuf. 91 (2016) 301–323. https://doi.org/10.1016/j.compositesa.2016.10.020.

[21] Y. Yang, W. Rigdon, X. Huang, X. Li, Enhancing graphene reinforcing potential in composites by hydrogen passivation induced dispersion, Sci. Rep. 3 (2013) 1–7. https://doi.org/10.1038/srep02086.

[22] X. Li, Y.M. Liu, W.G. Li, C.Y. Li, J.G. Sanjayan, W.H. Duan, Z. Li, Effects of graphene oxide agglomerates on workability, hydration, microstructure and compressive strength of cement paste, Constr. Build. Mater. 145 (2017) 402–410. https://doi.org/10.1016/j.conbuildmat.2017.04.058.

[23] A.K. Geim, K.S. Novoselov, The rise of graphene PROGRESS, Nat. Mater. 6 (2007) 183–191.

[24] W. Yu, L. Sisi, Y. Haiyan, L. Jie, Progress in the functional modification of graphene/graphene oxide: A review, RSC Adv. 10 (2020) 15328–15345. https://doi.org/10.1039/d0ra01068e.

[25] A.K. Geim, Graphene : Status and Prospects, 324 (2009) 1530–1535.

[26] J.C. Slonczewski, P.R. Weiss, Band Structure of Graphite, Phys. Rev. 109 (1958) 272–279.

[27] A. Tiwari, M. Syväjärvi, Graphene Materials: Fundamentals and Emerging Applications, John Wiley and Sons, 2015.

[28] E. Shamsaei, F.B. de Souza, X. Yao, E. Benhelal, A. Akbari, W. Duan, Graphene-based nanosheets for stronger and more durable concrete: A review, Constr. Build. Mater. 183 (2018) 642–660. https://doi.org/10.1016/j.conbuildmat.2018.06.201.

[29] C. Lee, X. Wei, J.W. Kysar, J. Hone, Measurement of the elastic properties and intrinsic strength of monolayer graphene, Science (80-. ). 321 (2008) 385–388.

[30] G. Jing, H. Feng, Q. Li, X. Li, J. Wu, S. Wang, X. Cheng, Z. Ye, Enhanced Dispersion of Graphene Oxide in Cement Matrix with Isolated-Dispersion Strategy, Ind. Eng. Chem. Res. 59 (2020) 10221–10228. https://doi.org/10.1021/acs.iecr.0c01230.

[31] B. Wang, S. Deng, Effect and mechanism of graphene nanoplatelets on hydration reaction, mechanical properties and microstructure of cement composites, Constr. Build. Mater. 228 (2019) 116720. https://doi.org/10.1016/j.conbuildmat.2019.116720.

[32] J. Tao, X. Wang, Z. Wang, Q. Zeng, Graphene nanoplatelets as an effective additive to tune the microstructures and piezoresistive properties of cement-based composites, Constr. Build. Mater. 209 (2019) 665–678. https://doi.org/10.1016/j.conbuildmat.2019.03.173.

[33] Z. Jiang, M.M. Sherif, G. Xing, O.E. Ozbulut, Tensile characterization of graphene nanoplatelets (GNP) mortar using acoustic emissions, Mater. Today Commun. 25 (2020) 101433. https://doi.org/10.1016/j.mtcomm.2020.101433.

[34] Z. Jiang, U. Kilic, O.E. Ozbulut, Mechanical properties and durability of cementitious composites reinforced by graphene nanoplatelets with different particle size and surface area, in: Behav. Mech. Multifunct. Mater. XV, 2021: p. 115890E.

[35] A.A. Balandin, S. Ghosh, W. Bao, I. Calizo, D. Teweldebrhan, F. Miao, C.N. Lau, Superior thermal conductivity of single-layer graphene, Nano Lett. 8 (2008) 902–907. https://doi.org/10.1021/nl0731872.

[36] S. Ghosh, I. Calizo, D. Teweldebrhan, E.P. Pokatilov, D.L. Nika, A.A. Balandin, W. Bao, F. Miao, C.N. Lau, Extremely high thermal conductivity of graphene: Prospects for thermal management applications in nanoelectronic circuits, Appl. Phys. Lett. 92 (2008) 1–4. https://doi.org/10.1063/1.2907977.

[37] J. Hu, X. Ruan, Y.P. Chen, Thermal conductivity and thermal rectification in H-terminated graphene nanoribbons, Nano Lett. 9 (2009) 2730–2735.

https://doi.org/10.1021/nl901231s.

[38] S. Chen, J. Jiang, H. Li, G. Liu, The salt-responsive transcriptome of Populus simonii×Populus nigra via DGE, Gene. 504 (2012) 203–212. https://doi.org/10.1016/j.gene.2012.05.023.

[39] A.A. Balandin, D.L. Nika, S. Ghosh, E.P. Pokatilov, Lattice thermal conductivity of graphene flakes: Comparison with bulk graphite, Appl. Phys. Lett. 94 (2009) 2–5. https://doi.org/10.1063/1.3136860.

[40] J. Chen, C. Jang, S. Xiao, M. Ishigami, M.S. Fuhrer, Intrinsic and extrinsic performance limits of graphene devices on SiO 2, Nat. Nanotechnol. 3 (2008) 206–209. https://doi.org/10.1038/nnano.2008.58.

[41] B. Marinho, M. Ghislandi, E. Tkalya, C.E. Koning, G. de With, Electrical conductivity of compacts of graphene, multi-wall carbon nanotubes, carbon black, and graphite powder, Powder Technol. 221 (2012) 351–358. https://doi.org/doi.org/10.1016/j.powtec.2012.01.024.

[42] A.P. Kauling, A.T. Seefeldt, D.P. Pisoni, R.C. Pradeep, R. Bentini, R.V.B. Oliveira, K.S. Novoselov, A.H. Castro Neto, The Worldwide Graphene Flake Production, Adv. Mater. 30 (2018) 1–6. https://doi.org/10.1002/adma.201803784.

[43] I.O. for Standardization, Nanotechnologies — Vocabulary — Part 13: Graphene and related two-dimensional (2D) materials, 2017.

[44] T.S. Qureshi, D.K. Panesar, B. Sidhureddy, A. Chen, P.C. Wood, Nano-cement composite with graphene oxide produced from epigenetic graphite deposit, Compos. Part B Eng. 159 (2019) 248–258. https://doi.org/10.1016/j.compositesb.2018.09.095.

[45] M. Krystek, A. Ciesielski, P. Samorì, Graphene-Based Cementitious Composites: Toward Next-Generation Construction Technologies, Adv. Funct. Mater. 2101887 (2021) 1–16. https://doi.org/10.1002/adfm.202101887.

[46] T.S. Qureshi, D.K. Panesar, Nano reinforced cement paste composite with functionalized

graphene and pristine graphene nanoplatelets, Compos. Part B Eng. 197 (2020) 108063. https://doi.org/10.1016/j.compositesb.2020.108063.

[47] S. Sun, B. Han, S. Jiang, X. Yu, Y. Wang, H. Li, J. Ou, Nano graphite platelets-enabled piezoresistive cementitious composites for structural health monitoring, Constr. Build. Mater. 136 (2017) 314–328. https://doi.org/10.1016/j.conbuildmat.2017.01.006.

[48] S. Chuah, W. Li, S.J. Chen, J.G. Sanjayan, W.H. Duan, Investigation on dispersion of graphene oxide in cement composite using different surfactant treatments, Constr. Build. Mater. 161 (2018) 519–527. https://doi.org/10.1016/j.conbuildmat.2017.11.154.

[49] M. Hu, J. Guo, P. Li, D. Chen, Y. Xu, Y. Feng, Y. Yu, H. Zhang, Effect of characteristics of chemical combined of graphene oxide-nanosilica nanocomposite fillers on properties of cement-based materials, Constr. Build. Mater. 225 (2019) 745–753. https://doi.org/10.1016/j.conbuildmat.2019.07.079.

[50] P. Turner, M. Hodnett, R. Dorey, J.D. Carey, Controlled Sonication as a Route to in-situ Graphene Flake Size Control, Sci. Rep. 9 (2019) 1–8. https://doi.org/10.1038/s41598-019-45059-5.

[51] B. Zhang, T. Chen, Study of ultrasonic dispersion of graphene nanoplatelets, Materials (Basel). 12 (2019). https://doi.org/10.3390/ma12111757.

[52] M. Wang, H. Yao, R. Wang, S. Zheng, Chemically functionalized graphene oxide as the additive for cement–matrix composite with enhanced fluidity and toughness, Constr. Build. Mater. 150 (2017) 150–156. https://doi.org/10.1016/j.conbuildmat.2017.05.217.

[53] T.S. Qureshi, D.K. Panesar, Impact of graphene oxide and highly reduced graphene oxide on cement based composites, Constr. Build. Mater. 206 (2019) 71–83. https://doi.org/10.1016/j.conbuildmat.2019.01.176.

[54] B. Wang, B. Pang, Mechanical property and toughening mechanism of water reducing agents modified graphene nanoplatelets reinforced cement composites, Constr. Build. Mater. 226 (2019) 699–711. https://doi.org/10.1016/j.conbuildmat.2019.07.229.

[55] V.D. Ho, C.T. Ng, C.J. Coghlan, A. Goodwin, C. Mc Guckin, T. Ozbakkaloglu, D. Losic, Electrochemically produced graphene with ultra large particles enhances mechanical properties of Portland cement mortar, Constr. Build. Mater. 234 (2020) 117403. https://doi.org/10.1016/j.conbuildmat.2019.117403.

[56] H. Du, S.D. Pang, Dispersion and stability of graphene nanoplatelet in water and its influence on cement composites, Constr. Build. Mater. 167 (2018) 403–413. https://doi.org/10.1016/j.conbuildmat.2018.02.046.

[57] J. An, B.H. Nam, Y. Alharbi, B.H. Cho, M. Khawaji, Edge-oxidized graphene oxide (EOGO) in cement composites: Cement hydration and microstructure, Compos. Part B Eng. 173 (2019). https://doi.org/10.1016/j.compositesb.2019.05.006.

[58] I.A. Vacchi, C. Ménard-Moyon, A. Bianco, Chemical Functionalization of Graphene Family Members, Phys. Sci. Rev. 2 (2017) 1–18. https://doi.org/10.1515/psr-2016-0103.

[59] L. Tang, J. Liu, N. Wang, L. Ye, Pre-Study of Graphene-Enhanced Cementitious Materials, Chalmers Univ. Technol. (2014).

[60] M.E. Abrishami, V. Zahabi, Reinforcing graphene oxide/cement composite with NH2 functionalizing group, Bull. Mater. Sci. 39 (2016) 1073–1078. https://doi.org/10.1007/s12034-016-1250-7.

[61] W.J. Long, T.H. Ye, L.X. Li, G.L. Feng, Electrochemical characterization and inhibiting mechanism on calcium leaching of graphene oxide reinforced cement composites, Nanomaterials. 9 (2019). https://doi.org/10.3390/nano9020288.

[62] I. Tragazikis, K.G. Dassios, P.T. Dalla, D.A. Exarchos, T.E. Matikas, Acoustic emission investigation of the effect of graphene on the fracture behavior of cement mortars, Eng. Fract. Mech. 210 (2019) 444–451. https://doi.org/10.1016/j.engfracmech.2018.01.004.

[63] L. Guardia, M.J. Fernández-Merino, J.I. Paredes, P. Solís-Fernández, S. Villar-Rodil, A. Martínez-Alonso, J.M.D. Tascón, High-throughput production of pristine graphene in an aqueous dispersion assisted by non-ionic surfactants, Carbon N. Y. 49 (2011) 1653–1662. https://doi.org/10.1016/j.carbon.2010.12.049.

[64] L. Liu, B. Gao, L. Wu, Y. Sun, Z. Zhou, Effects of surfactant type and concentration on graphene retention and transport in saturated porous media, Chem. Eng. J. 262 (2015) 1187–1191. https://doi.org/10.1016/j.cej.2014.10.032.

[65] Z.S. Metaxa, Polycarboxylate based superplasticizers as dispersant agents for exfoliated graphene nanoplatelets reinforcing cement based materials, J. Eng. Sci. Techno. Rev. 8 (2015) 1–5.

[66] A.H. Korayem, N. Tourani, M. Zakertabrizi, A.M. Sabziparvar, W.H. Duan, A review of dispersion of nanoparticles in cementitious matrices: Nanoparticle geometry perspective, Constr. Build. Mater. 153 (2017) 346–357. https://doi.org/10.1016/j.conbuildmat.2017.06.164.

[67] B. Zou, S.J. Chen, A.H. Korayem, F. Collins, C.M. Wang, W.H. Duan, Effect of ultrasonication energy on engineering properties of carbon nanotube reinforced cement pastes, Carbon N. Y. 85 (2015) 212–220. https://doi.org/10.1016/j.carbon.2014.12.094.

[68] I. Papanikolaou, L. Ribeiro de Souza, C. Litina, A. Al-Tabbaa, Investigation of the dispersion of multi-layer graphene nanoplatelets in cement composites using different superplasticiser treatments, Constr. Build. Mater. 293 (2021) 123543. https://doi.org/10.1016/j.conbuildmat.2021.123543.

[69] L. Guo, J. Wu, H. Wang, Mechanical and perceptual characterization of ultra-high-performance cement-based composites with silane-treated graphene nano-platelets, Constr. Build. Mater. 240 (2020) 117926. https://doi.org/10.1016/j.conbuildmat.2019.117926.

[70] F. Matalkah, P. Soroushian, Graphene nanoplatelet for enhancement the mechanical properties and durability characteristics of alkali activated binder, Constr. Build. Mater. 249 (2020) 118773. https://doi.org/10.1016/j.conbuildmat.2020.118773.

[71] A. Belli, A. Mobili, T. Bellezze, F. Tittarelli, P. Cachim, Evaluating the self-sensing ability of cement mortars manufactured with graphene nanoplatelets, virgin or recycled carbon fibers through piezoresistivity tests, Sustain. 10 (2018).

https://doi.org/10.3390/su10114013.

[72] L. Lavagna, D. Massella, E. Priola, M. Pavese, Relationship between oxygen content of graphene and mechanical properties of cement-based composites, Cem. Concr. Compos. 115 (2021) 103851. https://doi.org/10.1016/j.cemconcomp.2020.103851.

[73] W. Dong, W. Li, K. Wang, S.P. Shah, Physicochemical and Piezoresistive properties of smart cementitious composites with graphene nanoplates and graphite plates, Constr. Build. Mater. 286 (2021) 122943. https://doi.org/10.1016/j.conbuildmat.2021.122943.

[74] L. Li, Q. Zheng, B. Han, J. Ou, Fatigue behaviors of graphene reinforcing concrete composites under compression, Int. J. Fatigue. 151 (2021) 106354. https://doi.org/10.1016/j.ijfatigue.2021.106354.

[75] H. Li, S. Ding, L. Zhang, J. Ouyang, B. Han, Rheological behaviors of cement pastes with multi-layer graphene, Constr. Build. Mater. 269 (2021) 121327. https://doi.org/10.1016/j.conbuildmat.2020.121327.

[76] D. Shuang, A. Hongmei, W. Baomin, Research on the electromagnetic wave absorption properties of GNPs/EMD cement composite, Constr. Build. Mater. 321 (2022) 126398. https://doi.org/10.1016/j.conbuildmat.2022.126398.

[77] A. Reina, X. Jia, J. Ho, D. Nezich, H. Son, V. Bulovic, M.S. Dresselhaus, K. Jing, Large area, few-layer graphene films on arbitrary substrates by chemical vapor deposition, Nano Lett. 9 (2009) 30–35. https://doi.org/10.1021/nl801827v.

[78] S. Gayathri, P. Jayabal, M. Kottaisamy, V. Ramakrishnan, Synthesis of few layer graphene by direct exfoliation of graphite and a Raman spectroscopic study, Aip Adv. 4 (2014) 27116. https://doi.org/10.1063/1.4866595.

[79] Y. Arao, F. Mori, M. Kubouchi, Efficient solvent systems for improving production of few-layer graphene in liquid phase exfoliation, Carbon N. Y. 118 (2017) 18–24. https://doi.org/10.1016/j.carbon.2017.03.002.

[80] W. Zhou, J. Zeng, X. Li, J. Xu, Y. Shi, W. Ren, F. Miao, B. Wang, D. Xing, Ultraviolet

Raman spectra of double-resonant modes of graphene, Carbon N. Y. 101 (2016) 235–238. https://doi.org/10.1016/j.carbon.2016.01.102.

[81] S. Roscher, R. Hoffmann, O. Ambacher, Determination of the graphene-graphite ratio of graphene powder by Raman 2D band symmetry analysis, Anal. Methods. 11 (2019) 1180–1191. https://doi.org/10.1039/c8ay02619j.

[82] M. Wall, The Raman Spectroscopy of Graphene and the Determination of Layer Thickness, Thermo Sci. Note. 5 (2011) 1–5. https://tools.thermofisher.com/content/sfs/brochures/AN52252_E 1111 LayerThkns_H_1.pdf.

[83] M.A. Pimenta, G. Dresselhaus, M.S. Dresselhaus, L.G. Cancado, A. Jorio, R. Saito, Studying disorder in graphite-based systems by Raman spectroscopy, Phys. Chem. Chem. Phys. 9 (2007) 1276–1290. https://doi.org/10.1039/B613962K.

[84] L.M. Malard, M.A.A. Pimenta, G. Dresselhaus, M.S. Dresselhaus, Raman spectroscopy in graphene, Phys. Rep. 473 (2009) 51–87. https://doi.org/10.1016/j.physrep.2009.02.003.

[85] M. Begliarbekov, O. Sul, S. Kalliakos, E.H. Yang, S. Strauf, Determination of edge purity in bilayer graphene using μ-Raman spectroscopy, Appl. Phys. Lett. 97 (2010) 2008–2011. https://doi.org/10.1063/1.3464972.

[86] K.R. Paton, E. Varrla, C. Backes, R.J. Smith, U. Khan, A. O'Neill, C. Boland, M. Lotya, O.M. Istrate, P. King, T. Higgins, S. Barwich, P. May, P. Puczkarski, I. Ahmed, M. Moebius, H. Pettersson, E. Long, J. Coelho, S.E. O'Brien, E.K. McGuire, B.M. Sanchez, G.S. Duesberg, N. McEvoy, T.J. Pennycook, C. Downing, A. Crossley, V. Nicolosi, J.N. Coleman, Scalable production of large quantities of defect-free few-layer graphene by shear exfoliation in liquids, Nat. Mater. 13 (2014) 624–630. https://doi.org/10.1038/nmat3944.

[87] B. Nazari, Z. Ranjbar, R.R. Hashjin, A. Rezvani Moghaddam, G. Momen, B. Ranjbar, Dispersing graphene in aqueous media: Investigating the effect of different surfactants, Colloids Surfaces A Physicochem. Eng. Asp. 582 (2019).

https://doi.org/10.1016/j.colsurfa.2019.123870.

[88] J. Liu, J. Fu, Y. Yang, C. Gu, Study on dispersion, mechanical and microstructure properties of cement paste incorporating graphene sheets, Constr. Build. Mater. 199 (2019) 1–11. https://doi.org/10.1016/j.conbuildmat.2018.12.006.

[89] A. Eneborg, DEGREE PROJECT IN THE FIELD OF TECHNOLOGY Improvement and Characterization of Aqueous Graphene Dispersions, (2019).

[90] Y. Zhou, Q. Bao, L.A.L. Tang, Y. Zhong, K.P. Loh, Hydrothermal dehydration for the “green” reduction of exfoliated graphene oxide to graphene and demonstration of tunable optical limiting properties, Chem. Mater. 21 (2009) 2950–2956. https://doi.org/10.1021/cm9006603.

[91] U.K. Sur, A. Saha, A. Datta, B. Ankamwar, F. Surti, S.D. Roy, D. Roy, Synthesis and characterization of stable aqueous dispersions of graphene, Bull. Mater. Sci. 39 (2016) 159–165. https://doi.org/10.1007/s12034-015-0893-0.

[92] S.J. Chen, W. Wang, K. Sagoe-Crentsil, F. Collins, X.L. Zhao, M. Majumder, W.H. Duan, Distribution of carbon nanotubes in fresh ordinary Portland cement pastes: Understanding from a two-phase perspective, RSC Adv. 6 (2016) 5745–5753. https://doi.org/10.1039/c5ra13511g.

[93] B. Wang, R. Jiang, Z. Wu, Investigation of the mechanical properties and microstructure of graphene nanoplatelet-cement composite, Nanomaterials. 6 (2016). https://doi.org/10.3390/nano6110200.

[94] J. Lin, E. Shamsaei, F. Basquiroto de Souza, K. Sagoe-Crentsil, W.H. Duan, Dispersion of graphene oxide–silica nanohybrids in alkaline environment for improving ordinary Portland cement composites, Cem. Concr. Compos. 106 (2020) 103488. https://doi.org/10.1016/j.cemconcomp.2019.103488.

[95] S. Badaire, P. Poulin, M. Maugey, C. Zakri, In situ measurements of nanotube dimensions in suspensions by depolarized dynamic light scattering, Langmuir. 20 (2004) 10367–10370. https://doi.org/10.1021/la049096r.

[96] J. Shojaeiarani, D. Bajwa, G. Holt, Sonication amplitude and processing time influence the cellulose nanocrystals morphology and dispersion, Nanocomposites. 6 (2020) 41–46. https://doi.org/10.1080/20550324.2019.1710974.

[97] M. Lotya, A. Rakovich, J.F. Donegan, J.N. Coleman, Measuring the lateral size of liquid-exfoliated nanosheets with dynamic light scattering, Nanotechnology. 24 (2013). https://doi.org/10.1088/0957-4484/24/26/265703.

[98] A.N.J. Rodgers, M. Velický, R.A.W. Dryfe, Electrostatic Stabilization of Graphene in Organic Dispersions, Langmuir. 31 (2015) 13068–13076. https://doi.org/10.1021/acs.langmuir.5b04219.

[99] B.B. Feng, Z.H. Wang, W.H. Suo, Y. Wang, J.C. Wen, Y.F. Li, H.L. Suo, M. Liu, L. Ma, Performance of graphene dispersion by using mixed surfactants, Mater. Res. Express. 7 (2020). https://doi.org/10.1088/2053-1591/abb2ca.

[100] Q. Xie, A. Saeedi, E. Pooryousefy, Y. Liu, Extended DLVO-based estimates of surface force in low salinity water flooding, J. Mol. Liq. 221 (2016) 658–665. https://doi.org/10.1016/j.molliq.2016.06.004.

[101] F. Karakaş, M.S. Çelik, Stabilization mechanism of main paint pigments, Prog. Org. Coatings. 123 (2018) 292–298. https://doi.org/10.1016/j.porgcoat.2018.07.019.

[102] B. Konkena, S. Vasudevan, Understanding aqueous dispersibility of graphene oxide and reduced graphene oxide through p K a measurements, J. Phys. Chem. Lett. 3 (2012) 867–872. https://doi.org/10.1021/jz300236w.

[103] S. Srinivasan, S.A. Barbhuiya, D. Charan, S.P. Pandey, Characterising cement-superplasticiser interaction using zeta potential measurements, Constr. Build. Mater. 24 (2010) 2517–2521. https://doi.org/10.1016/j.conbuildmat.2010.06.005.

[104] E. Nägele, The zeta-potential of cement, Cem. Concr. Res. 15 (1985) 453–462. https://doi.org/10.1016/0008-8846(85)90118-8.

[105] Z. Sun, V. Nicolosi, D. Rickard, S.D. Bergin, D. Aherne, J.N. Coleman, Quantitative

evaluation of surfactant-stabilized single-walled carbon nanotubes: Dispersion quality and its correlation with zeta potential, J. Phys. Chem. C. 112 (2008) 10692–10699. https://doi.org/10.1021/jp8021634.

[106] J.S. Taurozzi, V.A. Hackley, M.R. Wiesner, Ultrasonic dispersion of nanoparticles for environmental, health and safety assessment issues and recommendations, Nanotoxicology. 5 (2011) 711–729. https://doi.org/10.3109/17435390.2010.528846.

[107] M. Wang, Y. Niu, J. Zhou, H. Wen, Z. Zhang, D. Luo, D. Gao, J. Yang, D. Liang, Y. Li, The dispersion and aggregation of graphene oxide in aqueous media, Nanoscale. 8 (2016) 14587–14592. https://doi.org/10.1039/c6nr03503e.

[108] A.M. Sabziparvar, E. Hosseini, V. Chiniforush, A.H. Korayem, Barriers to achieving highly dispersed graphene oxide in cementitious composites: An experimental and computational study, Constr. Build. Mater. 199 (2019) 269–278. https://doi.org/10.1016/j.conbuildmat.2018.12.030.

[109] D. Li, M.B. Müller, S. Gilje, R.B. Kaner, G.G. Wallace, Processable aqueous dispersions of graphene nanosheets, Nat. Nanotechnol. 3 (2008) 101–105. https://doi.org/10.1038/nnano.2007.451.

[110] Q. Liu, Q. Xu, Q. Yu, R. Gao, T. Tong, Experimental investigation on mechanical and piezoresistive properties of cementitious materials containing graphene and graphene oxide nanoplatelets, Constr. Build. Mater. 127 (2016) 565–576. https://doi.org/10.1016/j.conbuildmat.2016.10.024.

[111] B. Wang, D. Shuang, Effect of graphene nanoplatelets on the properties, pore structure and microstructure of cement composites, Mater. Express. 8 (2018) 407–416. https://doi.org/10.1166/mex.2018.1447.

[112] J. Tao, J. Wang, Q. Zeng, A comparative study on the influences of CNT and GNP on the piezoresistivity of cement composites, Mater. Lett. 259 (2020) 126858. https://doi.org/10.1016/j.matlet.2019.126858.

[113] O.E. Ozbulut, Z. Jiang, D.K. Harris, Exploring scalable fabrication of self-sensing

cementitious composites with graphene nanoplatelets, Smart Mater. Struct. 27 (2018) 115029. https://doi.org/10.1088/1361-665X/aae623.

[114] J. Le, H. Du, S. Dai Pang, Use of 2D Graphene Nanoplatelets (GNP) in cement composites for structural health evaluation, Compos. Part B Eng. 67 (2014) 555–563. https://doi.org/10.1016/j.compositesb.2014.08.005.

[115] A. Al-Dahawi, O. Öztürk, F. Emami, G. Yildirim, M. Şahmaran, Effect of mixing methods on the electrical properties of cementitious composites incorporating different carbon-based materials, Constr. Build. Mater. 104 (2016) 160–168. https://doi.org/10.1016/j.conbuildmat.2015.12.072.

[116] J. Xu, D. Zhang, Pressure-sensitive properties of emulsion modified graphene nanoplatelets / cement composites, Cem. Concr. Compos. 84 (2017) 74–82. https://doi.org/10.1016/j.cemconcomp.2017.07.025.

[117] H. Du, H.J. Gao, S.D. Pang, Improvement in concrete resistance against water and chloride ingress by adding graphene nanoplatelet, Cem. Concr. Res. 83 (2016) 114–123. https://doi.org/10.1016/j.cemconres.2016.02.005.

[118] G. Chen, M. Yang, L. Xu, Y. Zhang, Y. Wang, Graphene nanoplatelets impact on concrete in improving freeze-thaw resistance, Appl. Sci. 9 (2019). https://doi.org/10.3390/app9173582.

[119] A. Peyvandi, P. Soroushian, N. Farhadi, A.M. Balachandra, Evaluation of the Reinforcement Efficiency of Low-Cost Graphite Nanomaterials in High-Performance Concrete, KSCE J. Civ. Eng. 22 (2018) 3875–3882. https://doi.org/10.1007/s12205-018-0168-6.

[120] Q. Liu, W. Wu, J. Xiao, Y. Tian, J. Chen, A. Singh, Correlation between damage evolution and resistivity reaction of concrete in-filled with graphene nanoplatelets, Constr. Build. Mater. 208 (2019) 482–491. https://doi.org/10.1016/j.conbuildmat.2019.03.036.

[121] D. Dimov, I. Amit, O. Gorrie, M.D. Barnes, N.J. Townsend, A.I.S. Neves, F. Withers, S. Russo, M.F. Craciun, Ultrahigh Performance Nanoengineered Graphene–Concrete

Composites for Multifunctional Applications, Adv. Funct. Mater. 28 (2018). https://doi.org/10.1002/adfm.201705183.

[122] R.A. e Silva, P. de Castro Guetti, M.S. da Luz, F. Rouxinol, R.V. Gelamo, Enhanced properties of cement mortars with multilayer graphene nanoparticles, Constr. Build. Mater. 149 (2017) 378–385. https://doi.org/10.1016/j.conbuildmat.2017.05.146.

[123] W. Gao, N. Zhao, W. Yao, Z. Xu, H. Bai, C. Gao, Effect of flake size on the mechanical properties of graphene aerogels prepared by freeze casting, RSC Adv. 7 (2017) 33600–33605. https://doi.org/10.1039/c7ra05557a.

[124] Y. Gao, O.T. Picot, E. Bilotti, T. Peijs, Influence of filler size on the properties of poly (lactic acid)(PLA)/graphene nanoplatelet (GNP) nanocomposites, Eur. Polym. J. 86 (2017) 117–131. https://doi.org/10.1016/j.eurpolymj.2016.10.045.

[125] K. Nawaz, M. Ayub, N. Ul-Haq, M.B. Khan, M.B.K. Niazi, A. Hussain, Effects of selected size of graphene nanosheets on the mechanical properties of polyacrylonitrile polymer, Fibers Polym. 15 (2014) 2040–2044. https://doi.org/10.1007/s12221-014-2040-8.

[126] S. Dong, Y. Wang, A. Ashour, B. Han, J. Ou, Nano/micro-structures and mechanical properties of ultra-high performance concrete incorporating graphene with different lateral sizes, Compos. Part A Appl. Sci. Manuf. 137 (2020) 106011. https://doi.org/10.1016/j.compositesa.2020.106011.

[127] J.H. Xu, T. Fleiter, Y. Fan, W. Eichhammer, CO2 emissions reduction potential in China's cement industry compared to IEA's Cement Technology Roadmap up to 2050, Appl. Energy. 130 (2014) 592–602. https://doi.org/10.1016/j.apenergy.2014.03.004.

[128] B. Krejcirikova, J. Kolarik, P. Wargocki, The effects of cement-based and cement-ash-based mortar slabs on indoor air quality, Build. Environ. 135 (2018) 213–223. https://doi.org/10.1016/j.buildenv.2018.03.011.

[129] T. Santos, J. Almeida, J.D. Silvestre, P. Faria, Life cycle assessment of mortars: A review on technical potential and drawbacks, Constr. Build. Mater. 288 (2021) 123069.

https://doi.org/10.1016/j.conbuildmat.2021.123069.

[130] D.R. Vieira, J.L. Calmon, F.Z. Coelho, Life cycle assessment (LCA) applied to the manufacturing of common and ecological concrete: A review, Constr. Build. Mater. 124 (2016) 656–666. https://doi.org/10.1016/j.conbuildmat.2016.07.125.

[131] C.Z. Li, N.Q. Feng, Y. De Li, R.J. Chen, Effects of polyethlene oxide chains on the performance of polycarboxylate-type water-reducers, Cem. Concr. Res. 35 (2005) 867–873. https://doi.org/10.1016/j.cemconres.2004.04.031.

[132] S. V. Samchenko, O. V. Zemskova, I. V. Kozlova, Stabilization of carbon nanotubes with superplasticizers based on polycarboxylate resin ethers, Russ. J. Appl. Chem. 87 (2014) 1872–1876. https://doi.org/10.1134/S1070427214120131.

[133] A.C.I.C. 211, Standard Practice for Selecting Proportions for Normal, Heavyweight, and Mass Concrete, (1991) 1–38.

[134] K. Kouroupis-Agalou, A. Liscio, E. Treossi, L. Ortolani, V. Morandi, N.M. Pugno, V. Palermo, Fragmentation and exfoliation of 2-dimensional materials: A statistical approach, Nanoscale. 6 (2014) 5926–5933. https://doi.org/10.1039/c3nr06919b.

[135] P.G. Karagiannidis, S.A. Hodge, L. Lombardi, F. Tomarchio, N. Decorde, S. Milana, I. Goykhman, Y. Su, S. V. Mesite, D.N. Johnstone, R.K. Leary, P.A. Midgley, N.M. Pugno, F. Torrisi, A.C. Ferrari, Microfluidization of Graphite and Formulation of Graphene-Based Conductive Inks, ACS Nano. 11 (2017) 2742–2755. https://doi.org/10.1021/acsnano.6b07735.

[136] J. Walter, T.J. Nacken, C. Damm, T. Thajudeen, S. Eigler, W. Peukert, Determination of the lateral dimension of graphene oxide nanosheets using analytical ultracentrifugation, Small. 11 (2015) 814–825. https://doi.org/10.1002/smll.201401940.

[137] B. Zhang, T. Chen, L. Wang, B. Yang, Study of ultrasonic dispersion of graphene nanoplatelets, Gongneng Cailiao/Journal Funct. Mater. 50 (2019) 08133–08139. https://doi.org/10.3969/j.issn.1001-9731.2019.08.019.

[138] Z. Baig, O. Mamat, M. Mustapha, A. Mumtaz, K.S. Munir, M. Sarfraz, Investigation of tip sonication effects on structural quality of graphene nanoplatelets (GNPs) for superior solvent dispersion, Ultrason. Sonochem. 45 (2018) 133–149. https://doi.org/10.1016/j.ultsonch.2018.03.007.

[139] D. Graf, F. Molitor, K. Ensslin, C. Stampfer, A. Jungen, C. Hierold, L. Wirtz, Raman imaging of graphene, Solid State Commun. 143 (2007) 44–46. https://doi.org/10.1016/j.ssc.2007.01.050.

[140] Y. Hao, Y. Wang, L. Wang, Z. Ni, Z. Wang, R. Wang, C.K. Koo, Z. Shen, J.T.L. Thong, Probing layer number and stacking order of few-layer graphene by Raman spectroscopy, Small. 6 (2010) 195–200. https://doi.org/10.1002/smll.200901173.

[141] Y. Lin, H. Du, Graphene reinforced cement composites: A review, Constr. Build. Mater. 265 (2020) 120312. https://doi.org/10.1016/j.conbuildmat.2020.120312.

[142] M. li Cao, H. xia Zhang, C. Zhang, Effect of graphene on mechanical properties of cement mortars, J. Cent. South Univ. 23 (2016) 919–925. https://doi.org/10.1007/s11771-016-3139-4.

[143] X. Wang, S. Dong, A. Ashour, W. Zhang, B. Han, Effect and mechanisms of nanomaterials on interface between aggregates and cement mortars, Constr. Build. Mater. 240 (2020) 117942. https://doi.org/10.1016/j.conbuildmat.2019.117942.

[144] A. Standard, ASTM C109-standard test method for compressive strength of hydraulic cement mortars, ASTM Int. West Conshohocken, PA. (2008).

[145] B. Wang, R. Jiang, Z. Wu, Investigation of the mechanical properties and microstructure of graphene nanoplatelet-cement composite, Nanomaterials. 6 (2016) 200.

[146] W. Meng, K.H. Khayat, Mechanical properties of ultra-high-performance concrete enhanced with graphite nanoplatelets and carbon nanofibers, Compos. Part B Eng. 107 (2016) 113–122. https://doi.org/10.1016/j.compositesb.2016.09.069.

[147] A.M. Hunashyal, S. V. Tippa, S.S. Quadri, N.R. Banapurmath, Experimental Investigation

on Effect of Carbon Nanotubes and Carbon Fibres on the Behavior of Plain Cement Mortar Composite Round Bars under Direct Tension, ISRN Nanotechnol. 2011 (2011) 1–6. https://doi.org/10.5402/2011/856849.

[148] H. Alkhateb, A. Al-Ostaz, A.H.D. Cheng, X. Li, Materials genome for graphene-cement nanocomposites, J. Nanomechanics Micromechanics. 3 (2013) 67–77. https://doi.org/10.1061/(ASCE)NM.2153-5477.0000055.

[149] H. Du, S.D. Pang, Enhancement of barrier properties of cement mortar with graphene nanoplatelet, Cem. Concr. Res. 76 (2015) 10–19. https://doi.org/10.1016/j.cemconres.2015.05.007.

[150] S. Colombo, I.G. Main, M.C. Forde, Assessing damage of reinforced concrete beam using “b-value” analysis of acoustic emission signals, J. Mater. Civ. Eng. 15 (2003) 280–286. https://doi.org/10.1061/(ASCE)0899-1561(2003)15:3(280).

[151] T. Shiotani, Evaluation of progressive failure using AE sources and improved b-value on slope model tests, Prog. Acoust. Emiss. VII, JSNDI. (1994) 529–534.

[152] S. Rouchier, G. Foray, N. Godin, M. Woloszyn, J.J. Roux, Damage monitoring in fibre reinforced mortar by combined digital image correlation and acoustic emission, Constr. Build. Mater. 38 (2013) 371–380. https://doi.org/10.1016/j.conbuildmat.2012.07.106.

[153] A. Kelly, Test Methods, Nondestructive Evaluation and Smart Materials, Elsevier, 2000.

[154] A. Farhidzadeh, S. Salamone, P. Singla, A probabilistic approach for damage identification and crack mode classification in reinforced concrete structures, J. Intell. Mater. Syst. Struct. 24 (2013) 1722–1735. https://doi.org/10.1177/1045389X13484101.

[155] I.K. Tragazikis, K.G. Dassios, D.A. Exarchos, P.T. Dalla, T.E. Matikas, Acoustic emission investigation of the mechanical performance of carbon nanotube-modified cement-based mortars, Constr. Build. Mater. 122 (2016) 518–524. https://doi.org/10.1016/j.conbuildmat.2016.06.095.

[156] E. Tsangouri, D.G. Aggelis, A review of acoustic emission as indicator of reinforcement

effectiveness in concrete and cementitious composites, Constr. Build. Mater. 224 (2019) 198–205. https://doi.org/10.1016/j.conbuildmat.2019.07.042.

[157] A.O. Borode, N.A. Ahmed, P.A. Olubambi, Surfactant-aided dispersion of carbon nanomaterials in aqueous solution, Phys. Fluids. 31 (2019). https://doi.org/10.1063/1.5105380.

[158] M. Abedi, R. Fangueiro, A.G. Correia, Ultra-sensitive affordable cementitious composite with high mechanical and microstructural performances by hybrid CNT/GNP, Materials (Basel). 13 (2020). https://doi.org/10.3390/MA13163484.

[159] P. Alafogianni, K. Dassios, S. Farmaki, S.K. Antiohos, T.E. Matikas, N.M. Barkoula, On the efficiency of UV-vis spectroscopy in assessing the dispersion quality in sonicated aqueous suspensions of carbon nanotubes, Colloids Surfaces A Physicochem. Eng. Asp. 495 (2016) 118–124. https://doi.org/10.1016/j.colsurfa.2016.01.053.

[160] H. Korucu, B. Şimşek, A. Yartaşı, A TOPSIS-Based Taguchi Design to Investigate Optimum Mixture Proportions of Graphene Oxide Powder Synthesized by Hummers Method, Arab. J. Sci. Eng. 43 (2018) 6033–6055. https://doi.org/10.1007/s13369-018-3184-4.

[161] S.K. Gauri, S. Pal, The principal component analysis (PCA)-based approaches for multi-response optimization: Some areas of concerns, Int. J. Adv. Manuf. Technol. 70 (2014) 1875–1887. https://doi.org/10.1007/s00170-013-5389-8.

[162] B. Şimşek, G. Ultav, H. Korucu, A. Yartaşi, Improvement of the Graphene Oxide Dispersion Properties with the Use of TOPSIS Based Taguchi Application, (2018) 323–335.

[163] H. Korucu, B. Şimşek, A. Bilge, V. Arda, Vibrational Spectroscopy Homogeneous graphene oxide production with the variance reduction techniques : Taguchi method with the principal component analysis, 104 (2019).

[164] T. Uygunog, Multi-response optimization of polymer blended concrete : A TOPSIS based Taguchi application, 117 (2016) 251–262.

https://doi.org/10.1016/j.conbuildmat.2016.05.027.

[165] B. Şimşek, Y.T. Iç, E.H. Şimşek, A TOPSIS-based Taguchi optimization to determine optimal mixture proportions of the high strength self-compacting concrete, Chemom. Intell. Lab. Syst. 125 (2013) 18–32. https://doi.org/10.1016/j.chemolab.2013.03.012.

[166] S. Datta, G. Nandi, A. Bandyopadhyay, P. Kumar Pal, Application of PCA-based hybrid Taguchi method for correlated multicriteria optimization of submerged arc weld: A case study, Int. J. Adv. Manuf. Technol. 45 (2009) 276–286. https://doi.org/10.1007/s00170-009-1976-0.

[167] M. Abedi, R. Fangueiro, A. Camões, A. Gomes Correia, Evaluation of CNT/GNP's synergic effects on the Mechanical, Microstructural, and durability properties of a cementitious composite by the novel dispersion method, Constr. Build. Mater. 260 (2020) 120486. https://doi.org/10.1016/j.conbuildmat.2020.120486.

[168] E.E. Tkalya, M. Ghislandi, G. de With, C.E. Koning, The use of surfactants for dispersing carbon nanotubes and graphene to make conductive nanocomposites, Curr. Opin. Colloid Interface Sci. 17 (2012) 225–232. https://doi.org/10.1016/j.cocis.2012.03.001.

[169] R.J. Smith, M. Lotya, J.N. Coleman, The importance of repulsive potential barriers for the dispersion of graphene using surfactants, New J. Phys. 12 (2010). https://doi.org/10.1088/1367-2630/12/12/125008.

[170] A. Ghadimi, R. Saidur, H.S.C. Metselaar, A review of nanofluid stability properties and characterization in stationary conditions, Int. J. Heat Mass Transf. 54 (2011) 4051–4068. https://doi.org/10.1016/j.ijheatmasstransfer.2011.04.014.

[171] H. Zhang, N. Zhang, F. Fang, Electrodeposition of Nickel/Graphene Oxide Particle Composite Coatings: Effect of Surfactants on Graphene Oxide Dispersion and Coating Performance, J. Electrochem. Soc. 167 (2020) 162501. https://doi.org/10.1149/1945-7111/abcc32.

[172] S. Shamsi, A.A. Alagan, S.N.E. Sarchio, F. Md Yasin, Synthesis, characterization, and toxicity assessment of Pluronic F127-functionalized graphene oxide on the embryonic

development of Zebrafish (Danio Rerio), Int. J. Nanomedicine. 15 (2020) 8311–8329. https://doi.org/10.2147/IJN.S271159.

[173] S. Jain, B. Pradhan, Effect of cement type on hydration, microstructure and thermo-gravimetric behaviour of chloride admixed self-compacting concrete, Constr. Build. Mater. 212 (2019) 304–316. https://doi.org/10.1016/j.conbuildmat.2019.04.001.

[174] W. Deboucha, N. Leklou, A. Khelidj, M.N. Oudjit, Hydration development of mineral additives blended cement using thermogravimetric analysis (TGA): Methodology of calculating the degree of hydration, Constr. Build. Mater. 146 (2017) 687–701. https://doi.org/10.1016/j.conbuildmat.2017.04.132.

[175] T. Kim, J. Olek, Effects of sample preparation and interpretation of thermogravimetric curves on calcium hydroxide in hydrated pastes and mortars, Transp. Res. Rec. (2012) 10–18. https://doi.org/10.3141/2290-02.

[176] J.I. Bhatty, Hydration versus strength in a portland cement developed from domestic mineral wastes - a comparative study, Thermochim. Acta. 106 (1986) 93–103. https://doi.org/10.1016/0040-6031(86)85120-6.

[177] ASTM C1585-13, Standard Test Method for Measurement of Rate of Absorption of Water by Hydraulic Cement Concretes, ASTM Int. 41 (2013) 1–6. https://doi.org/10.1520/C1585-20.2.

[178] ASTM C642, Standard Test Method for Density, Absorption, and Voids in Hardened Concrete, ASTM International, United States, Annu. B. ASTM Stand. (1997) 1–3. https://doi.org/10.1520/C0642-13.5.

[179] A. Yazdanbakhsh, Z.C. Grasley, B. Tyson, R.K. Abu Al-Rub, Carbon nano filaments in cementitious materials: Some issues on dispersion and interfacial bond, Am. Concr. Institute, ACI Spec. Publ. (2009) 31–34.

[180] H. Yang, H. Cui, W. Tang, Z. Li, N. Han, F. Xing, A critical review on research progress of graphene/cement based composites, Compos. Part A Appl. Sci. Manuf. 102 (2017) 273–296. https://doi.org/10.1016/j.compositesa.2017.07.019.

[181] W. Meng, K.H. Khayat, Effect of graphite nanoplatelets and carbon nanofibers on rheology, hydration, shrinkage, mechanical properties, and microstructure of UHPC, Cem. Concr. Res. 105 (2018) 64–71. https://doi.org/10.1016/j.cemconres.2018.01.001.

[182] S. Chiranjiakumari, R. Ahmad, Compressive strength and durability behavior of graphene oxide reinforced concrete composites containing recycled concrete aggregate, J. Build. Eng. 32 (2020) 101800. https://doi.org/10.1016/j.jobe.2020.101800.

[183] P. Halamickova, R.J. Detwiler, D.P. Bentz, E.J. Garboczi, Water permeability and chloride ion diffusion in portland cement mortars: Relationship to sand content and critical pore diameter, Cem. Concr. Res. 25 (1995) 790–802. https://doi.org/10.1016/0008-8846(95)00069-O.

[184] M. Krystek, D. Pakulski, V. Patroniak, M. Górski, L. Szojda, A. Ciesielski, P. Samorì, High-Performance Graphene-Based Cementitious Composites, Adv. Sci. 6 (2019). https://doi.org/10.1002/advs.201801195.

[185] I. Agustí-Juan, G. Habert, Environmental design guidelines for digital fabrication, J. Clean. Prod. 142 (2017) 2780–2791. https://doi.org/10.1016/j.jclepro.2016.10.190.

[186] T. Stengel, P. Schießl, Life cycle assessment (LCA) of ultra high performance concrete (UHPC) structures, Woodhead Publishing Limited, 2013. https://doi.org/10.1533/9780857097729.3.528.

[187] R. Arvidsson, M. Janssen, M. Svanström, P. Johansson, B.A. Sandén, Energy use and climate change improvements of Li/S batteries based on life cycle assessment, J. Power Sources. 383 (2018) 87–92. https://doi.org/10.1016/j.jpowsour.2018.02.054.

[188] S. Pushkar, The effect of different concrete designs on the life-cycle assessment of the environmental impacts of concretes containing furnace bottom-ash instead of sand, Sustain. 11 (2019). https://doi.org/10.3390/su11154083.

[189] J. Zhao, Z. Wang, Q. Zhao, B. Xing, Adsorption of phenanthrene on multilayer graphene as affected by surfactant and exfoliation, Environ. Sci. Technol. 48 (2014) 331–339. https://doi.org/10.1021/es403873r.

[190] I. Papanikolaou, N. Arena, A. Al-Tabbaa, Graphene nanoplatelet reinforced concrete for self-sensing structures – A lifecycle assessment perspective, J. Clean. Prod. 240 (2019) 118202. https://doi.org/10.1016/j.jclepro.2019.118202.